ISSN 2732–0189 (Online)
ISSN 1586–2070 (Print)

JOURNAL OF COMPUTATIONAL AND APPLIED MECHANICS

An Open Access International Journal

Published by the University of Miskolc

VOLUME 18, NUMBER 1 (2023)

MISKOLC UNIVERSITY PRESS

ISSN 2732–0189 (Online)
ISSN 1586–2070 (Print)

JOURNAL OF COMPUTATIONAL AND APPLIED MECHANICS

An Open Access International Journal

Published by the University of Miskolc

VOLUME 18 NUMBER 1 (2023)

MISKOLC UNIVERSITY PRESS

Journal of Computational and Applied Mechanics, Vol. 18, No. 1, (2023), pp. 3–34
DOI: 10.32973/jcam.2023.001

STRESS-BASED DIMENSIONAL REDUCTION AND DUAL-MIXED *hp* FINITE ELEMENTS FOR ELASTIC PLATES

Edgár Bertóti
Institute of Applied Mechanics, University of Miskolc
H-3515 Miskolc-Egyetemváros, Hungary
edgar.bertoti@uni-miskolc.hu

[Received: November 1, 2022; Accepted: February 13, 2023]

Abstract. Starting from the linearized weak forms of the kinematic equation and the angular momentum balance equation of three-dimensional non-linear elasticity, a stress-based dimensional reduction procedure is presented for elastic plates. After expanding the three-dimensional non-symmetric stress tensor into power series with respect to the thickness coordinate, the translational equilibrium equations, written in terms of the expanded stress coefficients, are satisfied by introducing first-order stress functions. The symmetry of the stress field is satisfied in a weak sense by applying the material rotations as Lagrangian multipliers. The seven-field plate model developed in this way employs unmodified three-dimensional strain-stress relations.

On the basis of the dimensionally reduced plate model derived, a new dual-mixed plate bending finite element model is developed and presented. The numerical performance of the *hp*-version plate elements is investigated through the solutions of standard plate bending problems. It is shown that the modeling error of the stress-based plate model in the energy norm is better than that of the displacement-based Kirchhoff- and Reissner-Mindlin plate models. The numerical solutions and their comparisons to reference solutions indicate that the dual-mixed *hp* elements are free from locking problems, in either the energy norm or the stress computations, both for *h*- and *p*-extensions, and the results obtained for the stresses are accurate and reliable even for extremely thin plates.

Mathematical Subject Classification: 05C38, 15A15
Keywords: plate model, dimensional reduction, stress-based approach, dual-mixed weak formulation, locking-free *hp* finite element

1. Introduction

The finite element modeling of structural plate and shell problems has a long history and several successful formulations exist and are being used today in commercial finite element codes. The majority of the plate and shell elements are displacement-based ones and they usually rely on some assumptions regarding the transverse variation of the displacement components. Classical plate and shell theories, applying either the Kirchhoff-Love- or the Reissner-Mindlin hypothesis, with respect to the motion of the normal to the middle surface, are often called first-order theories [1].

There are two main directions in the construction of plate and shell finite elements: discretization based on dimensionally reduced theories leading to two-dimensional surface elements and continuum-based formulations leading to solid-shell, or degenerated three-dimensional, elements. Hierarchic sequences of plate and shell models and elements can also be constructed within the framework of either of these two modeling directions [2, 3].

Considering the approach of dimensional reduction, the first-order shear deformation models and elements with Reissner-Mindlin kinematics are the most popular ones. This is primarily due to the fact that they require C_0-continuous approximation of the displacement variables, in contrast to the C_1-continuity requirement of the elements with Kirchhoff-Love kinematics. It is also well-known that when low-order polynomial approximation is used for the displacements in these plate and shell elements, some inconsistencies in the representation of the transverse shear and membrane energies are introduced through the discretization, and the elements can exhibit different kind of numerical over-stiffening problems, usually called locking [2, 3]. Although the resolution of transverse shear locking and membrane locking in plate and shell elements has been the subject of intensive research in the last decades, and several successful strategies and techniques have been developed to alleviate locking, the improvement and stabilization of the low-order elements based on first-order plate and shell theories seems to be a never-ending story, see, e.g, [4, 5]. In the framework of the displacement-based formulations, higher-order approximations and the p-version of the finite element method are among the most reliable strategies for avoiding numerical convergence problems [6–9].

Considering the direction of the solid-shell approach, the plate and shell elements are usually deduced from continuum-based three-dimensional or solid finite elements [10, 11]. One of the main advantages of this formulation is the applicability of unmodified three-dimensional constitutive equations, in contrast to the dimensionally reduced first-order models, where the inconsistencies due to the kinematical constraints require the modification of the original three-dimensional constitutive equations. However, the solid-shell elements are not exempt from different kinds of numerical locking problems, either. In addition to the shear- and membrane locking, known from dimensionally reduced models, thickness locking, trapezoidal locking and incompressibility locking can also be present, especially when low-order approximation is used [11]. Although the research efforts spent for solving these problems has resulted in successful solutions, the improvement of solid-shell elements is still an active research area [4, 12].

Mixed-hybrid formulations and finite elements for plates and shells are usually based on a Hu-Washizu or Hellinger-Reissner type, primal-mixed or dual-mixed, variational principle. These formulations have also been intensively researched in the last few decades, especially because the elements of these types are proven or assumed to be exempt from numerical locking problems. The price for that is a larger number of independently approximated variables. An additional difficulty is that mixed-hybrid formulations require the choice of stable approximation spaces for the simultaneously approximated kinematic and stress variables [13]. It has also been long recognized that the majority of the modified and locking-free displacement-based plate and shell elements are equivalent or strongly related to elements deduced from mixed variational principles [1, 14].

Primal-mixed formulations and finite elements with continuous displacements and discontinuous surface tractions are much more popular than dual-mixed formulations and elements with continuous surface tractions and discontinuous displacements. This is partly due to fact that dual-mixed models and elements are more sophisticated, both theoretically and computationally, than the primal-mixed ones. An additional difficulty with dual-mixed models is their limited applicability to non-linear problems, as they rely on a complementary energy potential that should be expressed in terms of stresses. This may require the inversion of a general non-linear strain-stress relation, which can be a rather complicated task, if possible at all.

Dual-mixed elements can be formulated with either symmetric or non-symmetric stresses as primarily approximated variables. When symmetric stresses are used, the main problem is finding stable approximation spaces for them, even in the case of two-dimensional elasticity problems. This difficulty can be traced back to the construction of equilibrium elements with symmetric stresses, requiring C_1-continuous approximation for the second-order stress functions [15]. One resolution for this problem is to use dual-mixed variational principles with non-symmetric stresses and the symmetry of the stress tensor, the balance of angular momentum, is enforced then in a weak sense by applying the material rotations as Lagrangian multipliers [15, 16]. Finding stable approximation spaces for dual-mixed elements with non-symmetric stress space is relatively easy [17], which may be related to the fact that an equilibrated but non-symmetric stress field can be generated by C_0-continuous first-order stress functions. The stress boundary conditions in dual-mixed formulations are essential conditions and the related requirement of surface traction continuity is usually satisfied by employing hybridization techniques [13, 18].

The developments to be presented in this paper belong to a special research direction, the aim of which is the development of stress-based dimensionally reduced models for plates and shells using dual-mixed weak formulations with non-symmetric stress space. These models do not rely on the classical kinematical hypotheses and cannot be considered as stress resultant-based formulations. Instead, the stress space is directly approximated across the thickness by (truncated) power series, and the finite element model is based on a dual-mixed variational principle of Hellinger-Reissner or Fraeijs de Veubeke type. The former is a three-field principle and enforces both translational and rotational equilibrium in a weak sense, while the latter is a two-field principle and relies on equilibrated stress space, generated by first-order stress functions, and only the symmetry of the stress space is enforced weakly. Inter-element equilibrium, i.e., surface traction continuity, is satisfied by the related finite elements, and the numerical results are obtained directly for the approximated stress or stress-function variables.

Applying the two-field dual-mixed variational principle of Fraeijs de Veubeke, a dimensionally reduced plate model has already been derived in [19], but only the membrane problem was investigated by two-dimensional *hp* finite elements. Stress-based dimensionally reduced models and *hp* finite elements for axisymmetric problems of cylindrical shells have been presented by [20] using Fraeijs de Veubeke's two-field principle, and by [21] using the three-field dual-mixed principle of Hellinger-Reissner.

The performance of these two types of *hp* finite element models was compared in [22]. A stress-based dimensional reduction procedure based on Hellinger-Reissner's three-field principle, and the related dual-mixed *hp* finite elements for shells of revolution were developed in [23] for elastostatic problems, and in [24] for natural frequency analysis.

The starting point of the formulation and developments reported in this paper is the three-dimensional weak forms of the kinematic equation and the angular momentum balance equation of non-linear elasticity, summarized in Section 2. Following their consistent linearization, the dimensional reduction procedure for elastic plates in terms of stresses is presented in Section 3. Section 4 gives a brief description of the dual-mixed plate bending finite element formulation and the choice of stable approximation spaces for the first-order stress functions and the rotations. The performance and the capabilities of the stress-based plate model and the dual-mixed *hp* finite elements are investigated in Section 5 through the numerical solutions of well-known plate benchmark problems.

2. Preliminaries, strong and weak formulation

This section summarizes the strong formulation of non-linear elasticity in material description and recalls the weak forms of the kinematic equation and the balance of angular momentum, including their consistent linearization. Both symbolic and index notation of tensors will be used. Latin tensor indices are assumed to range over 1,2,3 and the Greek indices over 1 and 2. When index notation is used, the summation convention is applied. The scalar product between two tensors is indicated by one dot and the inner product is denoted by a colon. The tensorial product between two tensors of any order has no special sign.

2.1. **Strong formulation using material description.** The motion of the elastic body is investigated in a Cartesian reference frame. The initial configuration of the body is denoted by ${}^0V$ and its boundary by ${}^0S$ with outward unit normal ${}^0\boldsymbol{n}$. The position of a material point in the stress-free initial configuration is denoted by ${}^0\boldsymbol{x} = {}^0x_i\,\boldsymbol{e}_i$ and in the current deformed configuration by $\boldsymbol{x} = x_i\,\boldsymbol{e}_i$, where ${}^0x_i$ and x_i are the material and spatial coordinates of the same material point and $\boldsymbol{e}_i$ are the orthonormal base vectors. The differential operator with respect to the material coordinates is denoted by ${}^0\nabla = (\partial\,/\partial\,{}^0x_i)\,\boldsymbol{e}_i$.

Applying material description, the governing equations of a nonlinear boundary-value problem in three-dimensional elasticity are

- the kinematic equation:
$$\boldsymbol{F} = \boldsymbol{1} + \boldsymbol{u}\,{}^0\nabla, \tag{2.1}$$
where $\boldsymbol{F} = \boldsymbol{x}\,{}^0\nabla$ is the deformation gradient with determinant $J = \det \boldsymbol{F} > 0$, $\boldsymbol{1}$ is the second-order unit tensor and $\boldsymbol{u} = \boldsymbol{x} - {}^0\boldsymbol{x}$ is the displacement vector;
- the general form of the constitutive equation:
$$\boldsymbol{P} = \boldsymbol{P}(\boldsymbol{F}), \tag{2.2}$$
where $\boldsymbol{P}$ is the first Piola-Kirchhoff stress tensor;

- the balance of linear momentum (translational equilibrium equation):
$$\boldsymbol{P} \cdot {}^0\nabla + {}^0\rho \boldsymbol{b} = \boldsymbol{0}, \tag{2.3}$$
where ${}^0\rho$ is the reference density and $\boldsymbol{b}$ is the prescribed body force density per unit mass;
- the balance of angular momentum (rotational equilibrium equation):
$$\boldsymbol{P} \cdot \boldsymbol{F}^T - \boldsymbol{F} \cdot \boldsymbol{P}^T = \boldsymbol{0}, \tag{2.4}$$
where a T in the right superscript refers to the transpose; this equation expresses the symmetry of the Cauchy stress tensor $\boldsymbol{\sigma} = J^{-1}\boldsymbol{P} \cdot \boldsymbol{F}^T$.

The boundary conditions to the above system of partial differential equations are the displacement boundary conditions
$$\boldsymbol{u} = \widetilde{\boldsymbol{u}}\,, \qquad {}^0\boldsymbol{x} \in {}^0S_u\,, \tag{2.5}$$
and the stress boundary conditions
$$\boldsymbol{P} \cdot {}^0\boldsymbol{n} = {}^0\widetilde{\boldsymbol{p}}\,, \qquad {}^0\boldsymbol{x} \in {}^0S_p\,, \tag{2.6}$$
where $\widetilde{\boldsymbol{u}}$ is the prescribed displacement vector on ${}^0S_u$ and ${}^0\widetilde{\boldsymbol{p}}$ is the prescribed traction vector on ${}^0S_p$, where ${}^0S_u \cup {}^0S_p = {}^0S$ and ${}^0S_u \cap {}^0S_p = \emptyset$.

2.2. **Angular momentum balance and constitutive equation in terms of the Biot stress tensor.** The polar decomposition of the deformation gradient is given by
$$\boldsymbol{F} = \boldsymbol{R} \cdot \boldsymbol{U}, \tag{2.7}$$
where $\boldsymbol{R}$ is the orthogonal rotation tensor ($\boldsymbol{R}^T \cdot \boldsymbol{R} = \boldsymbol{1}$, $\det \boldsymbol{R} = 1$) and $\boldsymbol{U}$ is the symmetric right stretch tensor. The polar decomposition of the first Piola-Kirchhoff stress tensor $\boldsymbol{P}$ reads
$$\boldsymbol{P} = \boldsymbol{R} \cdot \boldsymbol{T}, \tag{2.8}$$
where $\boldsymbol{R}$ is the same orthogonal rotation tensor that appears in (2.7) and $\boldsymbol{T}$ is the (generally non-symmetric) Biot stress tensor.

The spatial Kirchhoff stress tensor $J\boldsymbol{\sigma}$ can be expressed by the Biot stress tensor and the right stretch tensor as
$$J\boldsymbol{\sigma} = \boldsymbol{P} \cdot \boldsymbol{F}^T = \boldsymbol{R} \cdot (\boldsymbol{T} \cdot \boldsymbol{U}) \cdot \boldsymbol{R}^T, \tag{2.9}$$
and the rotated Kirchhoff stress tensor is given by
$$\boldsymbol{R}^T \cdot (J\boldsymbol{\sigma}) \cdot \boldsymbol{R} = \boldsymbol{T} \cdot \boldsymbol{U}. \tag{2.10}$$
In view of (2.9)-(2.10), the material form of the balance of angular momentum (2.4) can be written in terms of $\boldsymbol{U}$ and $\boldsymbol{T}$ as
$$\boldsymbol{T} \cdot \boldsymbol{U} - \boldsymbol{U} \cdot \boldsymbol{T}^T = \boldsymbol{0}. \tag{2.11}$$
For the special case of isotropic materials $\boldsymbol{T}$ and $\boldsymbol{U}$ are coaxial and $\boldsymbol{T}$ is symmetric.

The right stretch tensor $\boldsymbol{U}$ and the Biot stress tensor $\boldsymbol{T}$ are work-conjugate strain and stress measures and the constitutive relation between them is uniquely invertible [25]. The inverse constitutive equation for the right stretch tensor can be given as
$$\boldsymbol{U} = \boldsymbol{U}(\boldsymbol{T}), \tag{2.12}$$

and the fourth-order tangent compliance tensor is defined by

$$\mathbb{C}^{-1} = \frac{\partial \boldsymbol{U}}{\partial \boldsymbol{T}}, \qquad \mathbb{C}^{-1}_{ijk\ell} = \frac{\partial U_{ij}}{\partial T_{k\ell}} \tag{2.13}$$

with major and minor symmetries $\mathbb{C}^{-1}_{ijk\ell} = \mathbb{C}^{-1}_{k\ell ij} = \mathbb{C}^{-1}_{ij\ell k}$.

2.3. **Weak forms of the kinematic equation.** The dual-mixed weak formulation applied in this paper is based on the weak forms of the kinematic equation (2.1) and the rotational equilibrium equation (2.11). The independent variables are the first Piola-Kirchhoff stress tensor $\boldsymbol{P}$ and the orthogonal rotation tensor $\boldsymbol{R}$.

Taking into account the polar decomposition (2.7) of the deformation gradient, the first weak form of the kinematic equation (2.1) can be written as

$$\delta\mathcal{W}_K = \int_{{}^0V} \delta\boldsymbol{P} : (\boldsymbol{R}\cdot\boldsymbol{U} - \mathbf{1} - \boldsymbol{u}\,{}^0\nabla)\,\mathrm{d}\,{}^0V = 0, \tag{2.14}$$

where $\delta\boldsymbol{P}$ is an arbitrary but differentiable tensorial test function called the virtual first Piola-Kirchhoff stress tensor. Applying the divergence theorem, the second weak form of (2.1) is obtained from (2.14) as

$$\delta\mathcal{W}_K = \int_{{}^0V} \left[\, \delta\boldsymbol{P} : (\boldsymbol{R}\cdot\boldsymbol{U} - \mathbf{1}) + (\delta\boldsymbol{P}\cdot{}^0\nabla)\cdot\boldsymbol{u} \,\right] \mathrm{d}\,{}^0V - \int_{{}^0S} \boldsymbol{u}\cdot\delta\boldsymbol{P}\cdot{}^0\boldsymbol{n}\,\mathrm{d}\,{}^0S = 0. \tag{2.15}$$

The displacements can be eliminated from (2.15) by prescribing the constraint equations

$$\delta\boldsymbol{P}\cdot{}^0\nabla = \mathbf{0}, \qquad {}^0\boldsymbol{x} \in {}^0V\,, \tag{2.16}$$

$$\delta\boldsymbol{P}\cdot{}^0\boldsymbol{n} = \mathbf{0}, \qquad {}^0\boldsymbol{x} \in {}^0S_p \tag{2.17}$$

on $\delta\boldsymbol{P}$, i.e., the virtual first Piola-Kirchhoff stress tensor is assumed to satisfy the homogeneous equilibrium equation (2.16) and the stress boundary condition (2.17). Making use of the displacement boundary condition (2.5) and (2.16)-(2.17), equation (2.15) transforms into

$$\delta\mathcal{W}_K(\boldsymbol{P},\boldsymbol{R},\delta\boldsymbol{P}) = \int_{{}^0V} \delta\boldsymbol{P} : (\boldsymbol{R}\cdot\boldsymbol{U} - \mathbf{1})\,\mathrm{d}\,{}^0V \; - \int_{{}^0S_u} \widetilde{\boldsymbol{u}}\cdot\delta\boldsymbol{P}\cdot{}^0\boldsymbol{n}\,\mathrm{d}\,{}^0S = 0. \tag{2.18}$$

2.4. **Weak forms of the angular momentum balance.** The weak form of the symmetry condition (2.4) for the Cauchy stress tensor can be given by

$$\delta\mathcal{W}_S = \int_{{}^0V} \delta\boldsymbol{\Omega} : (\boldsymbol{P}\cdot\boldsymbol{F}^T)\,\mathrm{d}\,{}^0V = 0, \tag{2.19}$$

where $\delta\boldsymbol{\Omega}$ is an arbitrary skew-symmetric tensor called the virtual spatial spin tensor. Taking into account the polar decompositions (2.7) and (2.8), we can write:

$$\delta\boldsymbol{\Omega} : (\boldsymbol{P}\cdot\boldsymbol{F}^T) = \delta\boldsymbol{\Omega} : (\boldsymbol{R}\cdot\boldsymbol{T}\cdot\boldsymbol{U}\cdot\boldsymbol{R}^T) = (\boldsymbol{R}^T\cdot\delta\boldsymbol{\Omega}\cdot\boldsymbol{R}) : (\boldsymbol{T}\cdot\boldsymbol{U}), \tag{2.20}$$

and the weak form of the angular momentum balance (2.19) can be written as

$$\delta\mathcal{W}_S(\boldsymbol{P},\boldsymbol{R},\delta\boldsymbol{R}) = \int_{{}^0V} \delta\boldsymbol{\Theta} : (\boldsymbol{T}\cdot\boldsymbol{U})\,\mathrm{d}\,{}^0V = 0, \tag{2.21}$$

where $\delta\boldsymbol{\Theta} = \boldsymbol{R}^T \cdot \delta\boldsymbol{\Omega} \cdot \boldsymbol{R}$ is an arbitrary skew-symmetric tensor called the virtual material spin tensor. The virtual spin tensors $\delta\boldsymbol{\Omega}$ and $\delta\boldsymbol{\Theta}$ are related to the virtual rotation tensor $\delta\boldsymbol{R}$ as

$$\delta\boldsymbol{\Omega} = \delta\boldsymbol{R} \cdot \boldsymbol{R}^T, \qquad \delta\boldsymbol{\Theta} = \boldsymbol{R}^T \cdot \delta\boldsymbol{R}. \tag{2.22}$$

When the rotation tensor $\boldsymbol{R}$ is parameterized by a rotation vector $\boldsymbol{\phi}$, according to

$$\boldsymbol{R}(\boldsymbol{\phi}) = \exp(\boldsymbol{\phi} \times \mathbf{1}), \tag{2.23}$$

the relation between the spatial and the material spin tensors in (2.22) can be given as [14, 26, 27]

$$\delta\boldsymbol{\Omega} = [\boldsymbol{\Gamma}(\boldsymbol{\phi}) \cdot \delta\boldsymbol{\phi}\,] \times \mathbf{1}, \qquad \delta\boldsymbol{\Theta} = [\boldsymbol{\Gamma}^T(\boldsymbol{\phi}) \cdot \delta\boldsymbol{\phi}\,] \times \mathbf{1}, \tag{2.24}$$

where

$$\boldsymbol{\Gamma}(\boldsymbol{\phi}) = \mathbf{1} + \frac{1-\cos\phi}{\phi^2}\,\boldsymbol{\phi} \times \mathbf{1} + \frac{1}{\phi^2}(1 - \frac{\sin\phi}{\phi})\,\boldsymbol{\phi} \times (\boldsymbol{\phi} \times \mathbf{1}). \tag{2.25}$$

Note that the weak forms (2.18) and (2.21) can also be derived from the two-field dual-mixed variational principle of Fraeijs de Veubeke [28].

2.5. **Linearization.** To linearize the weak forms of the kinematic equation and the angular momentum balance equation, (2.18) and (2.21), their directional derivatives should be computed in the independent variable directions $\Delta\boldsymbol{P}$ and $\Delta\boldsymbol{R}$, which represent sufficiently small increments in the stress- and rotation tensors. Assuming that the rotation tensor $\boldsymbol{R}$ is parameterized with respect to the rotation vector $\boldsymbol{\phi}$, according to (2.23), the directional derivative of $\boldsymbol{R} = \boldsymbol{R}(\boldsymbol{\phi})$ at $\boldsymbol{\phi}$ in the direction of the vectorial rotation increment $\Delta\boldsymbol{\phi}$ can be computed as

$$\Delta\boldsymbol{R} = D\boldsymbol{R}(\boldsymbol{\phi})[\Delta\boldsymbol{\phi}] = \boldsymbol{R} \cdot \Delta\boldsymbol{\Theta}, \qquad \Delta\boldsymbol{\Theta} = [\boldsymbol{\Gamma}^T(\boldsymbol{\phi}) \cdot \Delta\boldsymbol{\phi}\,] \times \mathbf{1}, \tag{2.26}$$

where the tangent tensor $\boldsymbol{\Gamma}(\boldsymbol{\phi})$ is given by (2.25).

2.5.1. *Directional derivatives of* $\boldsymbol{T}$ *and* $\boldsymbol{U}$. In the present formulation the Biot stress tensor

$$\boldsymbol{T}(\boldsymbol{P}, \boldsymbol{R}) = \boldsymbol{R}^T \cdot \boldsymbol{P}, \tag{2.27}$$

introduced in (2.8), depends on both $\boldsymbol{P}$ and $\boldsymbol{R}$. The directional derivatives of $\boldsymbol{T}$ at $\boldsymbol{P}$ and $\boldsymbol{R}$ in the directions of $\Delta\boldsymbol{P}$ and $\Delta\boldsymbol{R}$ can be written as

$$\Delta\boldsymbol{T} = \Delta_{\boldsymbol{P}}\boldsymbol{T} + \Delta_{\boldsymbol{R}}\boldsymbol{T}, \tag{2.28}$$

where, in view of (2.27) and (2.26),

$$\Delta_{\boldsymbol{P}}\boldsymbol{T} \equiv D\,\boldsymbol{T}[\Delta\boldsymbol{P}] = \frac{\partial\boldsymbol{T}}{\partial\boldsymbol{P}} : \Delta\boldsymbol{P} = \boldsymbol{R}^T \cdot \Delta\boldsymbol{P}, \tag{2.29}$$

and

$$\Delta_{\boldsymbol{R}}\boldsymbol{T} \equiv D\,\boldsymbol{T}[\Delta\boldsymbol{R}] = \frac{\partial\boldsymbol{T}}{\partial\boldsymbol{R}} : \Delta\boldsymbol{R} = \Delta\boldsymbol{\Theta}^T \cdot \boldsymbol{T}. \tag{2.30}$$

The directional derivative of the right stretch tensor $\boldsymbol{U}(\boldsymbol{T}) = \boldsymbol{U}[\boldsymbol{T}(\boldsymbol{P}, \boldsymbol{R})]$ at $\boldsymbol{P}$ and $\boldsymbol{R}$ in the directions of $\Delta\boldsymbol{P}$ and $\Delta\boldsymbol{R}$ can be computed as

$$\Delta\boldsymbol{U} = \Delta_{\boldsymbol{P}}\boldsymbol{U} + \Delta_{\boldsymbol{R}}\boldsymbol{U}, \tag{2.31}$$

where, taking into account (2.28)-(2.30) and (2.13),

$$\Delta_{\boldsymbol{P}} \boldsymbol{U} \equiv D\,\boldsymbol{U}(\boldsymbol{T})[\Delta \boldsymbol{P}] = \frac{\partial \boldsymbol{U}}{\partial \boldsymbol{T}} : D\,\boldsymbol{T}[\Delta \boldsymbol{P}] = \mathbb{C}^{-1} : \Delta_{\boldsymbol{P}} \boldsymbol{T}, \tag{2.32}$$

$$\Delta_{\boldsymbol{R}} \boldsymbol{U} \equiv D\,\boldsymbol{U}(\boldsymbol{T})[\Delta \boldsymbol{R}] = \frac{\partial \boldsymbol{U}}{\partial \boldsymbol{T}} : D\,\boldsymbol{T}[\Delta \boldsymbol{R}] = \mathbb{C}^{-1} : \Delta_{\boldsymbol{R}} \boldsymbol{T}. \tag{2.33}$$

Then, in view of (2.28), equation (2.31) can be written as

$$\Delta \boldsymbol{U} = \mathbb{C}^{-1} : (\Delta_{\boldsymbol{P}} \boldsymbol{T} + \Delta_{\boldsymbol{R}} \boldsymbol{T}) = \mathbb{C}^{-1} : \Delta \boldsymbol{T}. \tag{2.34}$$

2.5.2. *Directional derivatives of $\delta\mathcal{W}_K$ and $\delta\mathcal{W}_S$.* Taking into account (2.26) and (2.32)-(2.33), the directional derivatives of $\delta\mathcal{W}_K$ in (2.18) at $\boldsymbol{P}$ and $\boldsymbol{R}$ in the directions of $\Delta\boldsymbol{P}$ and $\Delta\boldsymbol{R}$ are

$$D_{\Delta \boldsymbol{P}}\, \delta\mathcal{W}_K = \int_{{}^0V} \delta \boldsymbol{P} : \big\{ \boldsymbol{R} \cdot D\,\boldsymbol{U}(\boldsymbol{T})[\Delta \boldsymbol{P}] \big\}\, \mathrm{d}\,{}^0V = \int_{{}^0V} \delta_{\boldsymbol{P}} \boldsymbol{T} : \mathbb{C}^{-1} : \Delta_{\boldsymbol{P}} \boldsymbol{T}\, \mathrm{d}\,{}^0V, \tag{2.35}$$

$$\begin{aligned} D_{\Delta \boldsymbol{R}}\, \delta\mathcal{W}_K &= \int_{{}^0V} \delta \boldsymbol{P} : \big\{ \Delta \boldsymbol{R} \cdot \boldsymbol{U} + \boldsymbol{R} \cdot D\,\boldsymbol{U}(\boldsymbol{T})[\Delta \boldsymbol{R}] \big\}\, \mathrm{d}\,{}^0V \\ &= \int_{{}^0V} \big[\, \delta_{\boldsymbol{P}} \boldsymbol{T} : (\Delta \boldsymbol{\Theta} \cdot \boldsymbol{U}) + \delta_{\boldsymbol{P}} \boldsymbol{T} : \mathbb{C}^{-1} : \Delta_{\boldsymbol{R}} \boldsymbol{T} \,\big]\, \mathrm{d}\,{}^0V, \end{aligned} \tag{2.36}$$

where

$$\delta_{\boldsymbol{P}} \boldsymbol{T} \equiv D\,\boldsymbol{T}(\boldsymbol{P}, \boldsymbol{R})[\delta \boldsymbol{P}] = \frac{\partial \boldsymbol{T}}{\partial \boldsymbol{P}} : \delta \boldsymbol{P} = \boldsymbol{R}^T \cdot \delta \boldsymbol{P}. \tag{2.37}$$

Taking into account (2.26) and (2.29)-(2.30), as well as (2.32)-(2.33), the directional derivatives of $\delta\mathcal{W}_S$ in (2.21) at $\boldsymbol{P}$ and $\boldsymbol{R}$ in the directions of $\Delta\boldsymbol{P}$ and $\Delta\boldsymbol{R}$ are

$$\begin{aligned} D_{\Delta \boldsymbol{P}}\, \delta\mathcal{W}_S &= \int_{{}^0V} \delta \boldsymbol{\Theta} : \big\{ D\,\boldsymbol{T}[\Delta \boldsymbol{P}] \cdot \boldsymbol{U} + \boldsymbol{T} \cdot D\,\boldsymbol{U}(\boldsymbol{T})[\Delta \boldsymbol{P}] \big\}\, \mathrm{d}\,{}^0V \\ &= \int_{{}^0V} \big[\, (\delta \boldsymbol{\Theta} \cdot \boldsymbol{U}) : \Delta_{\boldsymbol{P}} \boldsymbol{T} + \delta_{\boldsymbol{R}} \boldsymbol{T} : \mathbb{C}^{-1} : \Delta_{\boldsymbol{P}} \boldsymbol{T} \,\big]\, \mathrm{d}\,{}^0V, \end{aligned} \tag{2.38}$$

$$\begin{aligned} D_{\Delta \boldsymbol{R}}\, \delta\mathcal{W}_S &= \int_{{}^0V} \delta \boldsymbol{\Theta} : \big\{ D\,\boldsymbol{T}[\Delta \boldsymbol{R}] \cdot \boldsymbol{U} + \boldsymbol{T} \cdot D\,\boldsymbol{U}(\boldsymbol{T})[\Delta \boldsymbol{R}] \big\}\, \mathrm{d}\,{}^0V \\ &= \int_{{}^0V} \big[\, (\boldsymbol{T} \cdot \boldsymbol{U}) : (\delta \boldsymbol{\Theta} \cdot \Delta \boldsymbol{\Theta}) + \delta_{\boldsymbol{R}} \boldsymbol{T} : \mathbb{C}^{-1} : \Delta_{\boldsymbol{R}} \boldsymbol{T} \,\big]\, \mathrm{d}\,{}^0V, \end{aligned} \tag{2.39}$$

where

$$\delta_{\boldsymbol{R}} \boldsymbol{T} \equiv D\,\boldsymbol{T}(\boldsymbol{P}, \boldsymbol{R})[\delta \boldsymbol{R}] = \frac{\partial \boldsymbol{T}}{\partial \boldsymbol{R}} : \delta \boldsymbol{R} = \delta \boldsymbol{\Theta}^T \cdot \boldsymbol{T}. \tag{2.40}$$

2.5.3. *Linearized weak forms.* Considering a trial solution ${}^t\boldsymbol{P}$ and ${}^t\boldsymbol{R}$, the weak forms of the kinematic equation (2.18) and the angular momentum balance equation (2.21) can be linearized in the directions of the stress- and rotation increments $\Delta\boldsymbol{P}$ and $\Delta\boldsymbol{R}$ at ${}^t\boldsymbol{P}$ and ${}^t\boldsymbol{R}$ according to

$$\delta\mathcal{W}_K({}^t\boldsymbol{P}, {}^t\boldsymbol{R}, \delta \boldsymbol{P}) + D_{\Delta \boldsymbol{P}}\, \delta\mathcal{W}_K({}^t\boldsymbol{P}, {}^t\boldsymbol{R}, \delta \boldsymbol{P}) + D_{\Delta \boldsymbol{R}}\, \delta\mathcal{W}_K({}^t\boldsymbol{P}, {}^t\boldsymbol{R}, \delta \boldsymbol{P}) = 0, \tag{2.41}$$

$$\delta\mathcal{W}_S({}^t\boldsymbol{P}, {}^t\boldsymbol{R}, \delta \boldsymbol{R}) + D_{\Delta \boldsymbol{P}}\, \delta\mathcal{W}_S({}^t\boldsymbol{P}, {}^t\boldsymbol{R}, \delta \boldsymbol{R}) + D_{\Delta \boldsymbol{R}}\, \delta\mathcal{W}_S({}^t\boldsymbol{P}, {}^t\boldsymbol{R}, \delta \boldsymbol{R}) = 0. \tag{2.42}$$

Taking into account (2.35)-(2.36) and (2.38)-(2.39), equations (2.41) and (2.42) can be written as

$$\int_{{}^0V}\big[\,\delta_{\boldsymbol{P}}\boldsymbol{T} : {}^t\mathbb{C}^{-1} : \Delta\boldsymbol{T} \;+\; \delta_{\boldsymbol{P}}\boldsymbol{T} : (\Delta\boldsymbol{\Theta}\cdot{}^t\boldsymbol{U})\big]\,\mathrm{d}\,{}^0V \\ + \int_{{}^0V} \delta\boldsymbol{P} : (\,{}^t\boldsymbol{R}\cdot{}^t\boldsymbol{U} - \mathbf{1})\,\mathrm{d}\,{}^0V - \int_{{}^0S_u} \widetilde{\boldsymbol{u}}\cdot\delta\boldsymbol{P}\cdot{}^0\boldsymbol{n}\,\mathrm{d}\,{}^0S = 0, \tag{2.43}$$

$$\int_{{}^0V}\big[\,\delta_{\boldsymbol{R}}\boldsymbol{T} : {}^t\mathbb{C}^{-1} : \Delta\boldsymbol{T} \;+\; \Delta_{\boldsymbol{P}}\boldsymbol{T} : (\delta\boldsymbol{\Theta}\cdot{}^t\boldsymbol{U}) \\ + (\,{}^t\boldsymbol{T}\cdot{}^t\boldsymbol{U}) : (\delta\boldsymbol{\Theta}\cdot\Delta\boldsymbol{\Theta})\,\big]\,\mathrm{d}\,{}^0V + \int_{{}^0V}\delta\boldsymbol{\Theta} : (\,{}^t\boldsymbol{T}\cdot{}^t\boldsymbol{U})\,\mathrm{d}\,{}^0V = 0, \tag{2.44}$$

where ${}^t\mathbb{C}^{-1}$ is the tangent compliance tensor at ${}^t\boldsymbol{T} = {}^t\boldsymbol{R}^T\cdot{}^t\boldsymbol{P}$. The linearized weak forms (2.43) and (2.44) serve as the basis for the dual-mixed finite element solution procedure of the nonlinear elasticity problem. Note that when the approximation is based on the Bubnov-Galerkin method, the above dual-mixed formulation leads to symmetric system matrices.

Subsidiary conditions to the weak forms (2.43)-(2.44), to be *a priori* satisfied during the incremental solution procedure, are the translational equilibrium equation

$$\Delta\boldsymbol{P}\cdot{}^0\nabla + {}^0\!\rho\boldsymbol{b} = \mathbf{0}, \qquad {}^0\boldsymbol{x}\in{}^0V, \tag{2.45}$$

and the stress boundary condition

$$\Delta\boldsymbol{P}\cdot{}^0\boldsymbol{n} = {}^0\widetilde{\boldsymbol{p}}, \qquad {}^0\boldsymbol{x}\in{}^0S_p\,. \tag{2.46}$$

At the initial, stress-free configuration the trial solution in (2.43)-(2.44) is ${}^t\boldsymbol{P} = \mathbf{0}$ and ${}^t\boldsymbol{R} = \mathbf{1}$ from which it follows that ${}^t\boldsymbol{T} = {}^t\boldsymbol{R}^T\cdot{}^t\boldsymbol{P} = \mathbf{0}$ and

$$\delta_{\boldsymbol{R}}\boldsymbol{T} = \Delta_{\boldsymbol{R}}\boldsymbol{T} = \mathbf{0}, \qquad \delta_{\boldsymbol{P}}\boldsymbol{T} = \delta\boldsymbol{P} = \delta\boldsymbol{T}, \qquad \Delta_{\boldsymbol{P}}\boldsymbol{T} = \Delta\boldsymbol{P} = \Delta\boldsymbol{T}. \tag{2.47}$$

Since ${}^t\boldsymbol{U} = \mathbf{1}$ and ${}^t\boldsymbol{\phi} = \mathbf{0}$ also hold, from (2.24)-(2.26) it follows that

$$\delta\boldsymbol{\Theta} = \delta\boldsymbol{\phi}\times\mathbf{1}, \qquad \Delta\boldsymbol{\Theta} = \Delta\boldsymbol{\phi}\times\mathbf{1}, \tag{2.48}$$

and the linearized weak forms (2.43)-(2.44) simplify to

$$\int_{{}^0V}(\,\delta\boldsymbol{T} : \mathbb{C}^{-1} : \Delta\boldsymbol{T} + \delta\boldsymbol{T} : \Delta\boldsymbol{\Theta}\,)\,\mathrm{d}\,{}^0V - \int_{{}^0S_u}\widetilde{\boldsymbol{u}}\cdot\delta\boldsymbol{T}\cdot{}^0\boldsymbol{n}\,\mathrm{d}\,{}^0S = 0, \tag{2.49}$$

$$\int_{{}^0V}\delta\boldsymbol{\Theta} : \Delta\boldsymbol{T}\,\mathrm{d}\,{}^0V = 0. \tag{2.50}$$

Finite element models based on the above weak forms requires *a priori* satisfaction of the subsidiary conditions (2.45)-(2.46) and leads to a stress-based numerical solution of the linear elasticity problem. The translational equilibrium equation (2.45) can identically be satisfied by introducing first-order stress functions [15, 29]. The stress boundary condition (2.46) is usually taken into account in the course of the finite element solution procedure by applying hybridization techniques [13, 18].

3. Dimensional reduction for plates in terms of stresses

This section presents a stress-based dimensional reduction procedure for linearly elastic plates. The independent variables, the non-symmetric stresses and the rotations, are expanded into power series with respect to the thickness coordinate. After making assumptions on the transverse variations of the stress components across the thickness, the translational equilibrium equations will be satisfied by introducing one first-order stress function vector. The stress boundary conditions on the faces of the plate are incorporated into the equilibrated stress space. The weak formulation for the plate model, which serve as a basis for the development of the dual-mixed *hp* finite elements in Sections 4 and 5, will be derived from the linearized three-dimensional weak forms (2.49) and (2.50).

3.1. **Notation for plates.** In the developments of this section, the index notation of tensor variables is used. The left superscript 0, referring to the initial configuration, will be neglected for $\boldsymbol{x}$, $\boldsymbol{n}$, $\boldsymbol{p}$, ρ, V, S and ∇, as notational distinction between the reference and the current configuration is unnecessary in the linear elastic case.

The reference configuration of the three-dimensional plate of thickness d is denoted by

$$V = \{x_a \in \mathbb{R}^3 : \, x_\alpha \in \bar{S}, \; |x_3| < d/2\}, \tag{3.1}$$

where $\bar{S} \in \mathbb{R}^2$ is the reference middle plane of the plate, parameterized by the Cartesian coordinates x_α, and the coordinate x_3 is measured along a straight line perpendicular to $\bar{S}$. It is assumed that both V and $\bar{S}$ are simply connected and bounded sets in $\mathbb{R}^3$ and $\mathbb{R}^2$, respectively, and the thickness d is independent of x_α.

The boundary of V, denoted by S, consists of the top and bottom surfaces $S^\pm$ and the lateral surface $S^\times$ ($S = S^\pm \cup S^\times$, $S^\pm \cap S^\times = \emptyset$) with outward unit normals $\boldsymbol{n}^\pm = \pm \boldsymbol{e}_3$ and $\boldsymbol{n}^\times = n^\times_\lambda \boldsymbol{e}_\lambda$, respectively. It is assumed that the plate is subjected to body forces $\rho \boldsymbol{b}$ in V and surface loads $\widetilde{\boldsymbol{p}}^\pm$ on $S^\pm$. On the lateral surface $S^\times = S^\times_p \cup S^\times_u$ ($S^\times_p \cap S^\times_u = \emptyset$), surface load $\widetilde{\boldsymbol{p}}^\times$ on $S^\times_p$ and the displacement vector $\widetilde{\boldsymbol{u}}^\times$ on $S^\times_u$ are prescribed. The boundary curve of the reference middle plane, $\bar{S}$, is denoted by $\ell = \ell_u \cup \ell_p$ ($\ell_u \cap \ell_p = \emptyset$).

3.2. **Approximation of the stress space across the thickness.** Applying index notation, the linearized weak forms (2.49)-(2.50) can be written as

$$\int_V (\, \delta T_{ij} \, \mathbb{C}^{-1}_{ijk\ell} \, T_{k\ell} + \delta T_{k\ell} \, \Theta_{k\ell} \,) \, \mathrm{d}V - \int_{S^\times_u} \widetilde{u}^\times_k \, \delta T_{k\lambda} \, n^\times_\lambda \, \mathrm{d}S = 0, \tag{3.2}$$

$$\int_V \delta\Theta_{k\ell} \, T_{k\ell} \, \mathrm{d}V = 0, \tag{3.3}$$

where, for the sake of notational simplicity, the sign Δ is neglected in the first increment of the stress- and rotation tensors, i.e., $\Delta T_{k\ell} = T_{k\ell}$ and $\Delta\Theta_{k\ell} = \Theta_{k\ell}$ correspond to the linear solution. Assuming linearly elastic and isotropic material,

$$\mathbb{C}^{-1}_{ijk\ell} = \frac{1}{2\mu} \Big[\frac{1}{2} (\delta_{ik}\delta_{j\ell} + \delta_{i\ell}\delta_{jk}) - \frac{\nu}{1+\nu} \, \delta_{ij}\delta_{k\ell} \Big] \tag{3.4}$$

with Kronecker symbol δ_{ij}, shear modulus μ and Poisson ratio ν. The components of the stress tensor $\boldsymbol{T} = \boldsymbol{p}_\ell\, \boldsymbol{e}_\ell = T_{k\ell}\, \boldsymbol{e}_k \boldsymbol{e}_\ell$ with stress vector $\boldsymbol{p}_\ell$ should *a priori* satisfy the translational equilibrium equations

$$T_{k\ell,\ell} + \rho b_k = 0 \tag{3.5}$$

and the stress boundary conditions on the faces and on the lateral surfaces of the plate:

$$\boldsymbol{T} \cdot \boldsymbol{n}^{\pm} = \pm\, \boldsymbol{p}_3 = \widetilde{\boldsymbol{p}}^{\,\pm} \qquad \text{on } S_p^{\pm}, \tag{3.6}$$

$$\boldsymbol{T} \cdot \boldsymbol{n}^{\times} = n_\lambda^{\times}\, \boldsymbol{p}_\lambda = \widetilde{\boldsymbol{p}}^{\,\times} \qquad \text{on } S_p^{\times}. \tag{3.7}$$

In (3.5), the comma followed by the index ℓ in the right subscript denotes partial differentiation with respect to x_ℓ.

The first step in the derivation of the stress-based, dimensionally reduced plate model is the expansion of the stress components and the prescribed body forces into power series with respect to the thickness coordinate x_3, according to

$$T_{k\ell}(x_\alpha, x_3) = \sum_{i=0}^{n} {}_iT_{k\ell}(x_\alpha)\,(x_3)^i, \qquad b_\ell(x_\alpha, x_3) = \sum_{i=0}^{n} {}_ib_\ell(x_\alpha)\,(x_3)^i, \tag{3.8}$$

where $n > 0$ is an integer. According to the notation applied in (3.8), an index on the left subscript refers to the power of x_3. Substituting (3.8) into (3.5) and making separation with respect to the powers of x_3, we obtain a set of two-dimensional equilibrium equations:

$${}_iT_{k\lambda,\lambda} + (i+1)\, {}_{i+1}T_{k3} + \rho\, {}_ib_k = 0, \quad i = 0, 1, 2, ..., n. \tag{3.9}$$

Depending on the number of n chosen, a variety of plate models can be derived.

The next step in the derivation of the plate model is making assumptions on the transverse variations of the three-dimensional stress components. In this paper, a model described by $n = 1$ in (3.9) is chosen, which means that the first two equilibrium equations of (3.9) are selected:

$${}_0T_{k\lambda,\lambda} + {}_1T_{k3} + \rho\, {}_0b_k = 0, \tag{3.10}$$

$${}_1T_{k\lambda,\lambda} + 2\, {}_2T_{k3} + \rho\, {}_1b_k = 0, \tag{3.11}$$

and the equations characterized by $n > 1$ are neglected with the assumption that they are identically satisfied. Following from (3.10)-(3.11), the transverse variations of the stress components in x_3 are assumed to be

$$T_{k\lambda}(x_\alpha, x_3) = {}_0T_{k\lambda}(x_\alpha) + {}_1T_{k\lambda}(x_\alpha)\, x_3, \tag{3.12}$$

$$T_{k3}(x_\alpha, x_3) = {}_0T_{k3}(x_\alpha) + {}_1T_{k3}(x_\alpha)\, x_3 + {}_2T_{k3}(x_\alpha)\,(x_3)^2, \tag{3.13}$$

i.e., the stress vectors $\boldsymbol{p}_\lambda = \boldsymbol{T} \cdot \boldsymbol{e}_\lambda = T_{k\lambda}\, \boldsymbol{e}_k$, parallel to the middle plane of the plate, are linear functions of the coordinate x_3, whereas the stress vector $\boldsymbol{p}_3 = \boldsymbol{T} \cdot \boldsymbol{e}_3 = T_{k3}\, \boldsymbol{e}_k$, perpendicular to the middle plane, is parabolic in x_3.

To keep the number of the independent stress components as minimal as possible, the stress boundary conditions on the top and bottom faces of the plate will be incorporated in the equilibrium equations (3.10)-(3.11), just like in the case of the stress resultant-based shell models. By the procedure described subsequently, the number of the independent stress coefficients in (3.12)-(3.13) can be reduced from 21 to 15.

Taking into account (3.13), the stress boundary conditions (3.6) on the top and bottom faces of the plate can be written as

$$ {}_0T_{k3} \pm {}_1T_{k3}\,\frac{d}{2} + {}_2T_{k3}\,\frac{d^2}{4} = \pm\widetilde{p}_k^{\pm} \qquad \text{on } S_p^{\pm}. \tag{3.14} $$

Adding and subtracting the two equations in (3.14) and defining the load vector

$$ \widetilde{\boldsymbol{p}}\,(x_\alpha, x_3) = {}_0\widetilde{\boldsymbol{p}} + {}_1\widetilde{\boldsymbol{p}}\,x^3, \qquad \widetilde{\boldsymbol{p}}\,(x_\alpha, \pm d/2) := \pm\widetilde{\boldsymbol{p}}^{\pm} \tag{3.15} $$

with coefficients

$$ {}_0\widetilde{\boldsymbol{p}}\,(x_\alpha) = \frac{1}{2}\,(\widetilde{\boldsymbol{p}}^{+} - \widetilde{\boldsymbol{p}}^{-}), \qquad {}_1\widetilde{\boldsymbol{p}}\,(x_\alpha) = \frac{1}{d}\,(\widetilde{\boldsymbol{p}}^{+} + \widetilde{\boldsymbol{p}}^{-}), \tag{3.16} $$

the stress boundary conditions (3.14) can be rewritten as

$$ {}_0T_{k3} + \frac{d^2}{4}\,{}_2T_{k3} = {}_0\widetilde{p}_k, \tag{3.17} $$

$$ {}_1T_{k3} = {}_1\widetilde{p}_k. \tag{3.18} $$

Making use of (3.17)-(3.18), the two equilibrium equations in (3.10)-(3.11) take the forms

$$ {}_0T_{k\lambda,\lambda} + {}_1\widetilde{p}_k + \rho\,{}_0b_k = 0, \tag{3.19} $$

$$ {}_1T_{k\lambda,\lambda} - \frac{8}{d^2}\,{}_0T_{k3} + \frac{8}{d^2}\,{}_0\widetilde{p}_k + \rho\,{}_1b_k = 0. \tag{3.20} $$

To obtain a numerically more efficient formulation, the number of the independent stress variables can be further reduced by satisfying the symmetry of the transverse shear stresses in an integral average sense, according to the equation

$$ \int_{-d/2}^{+d/2} T_{\lambda 3}\,\mathrm{d}x_3 = \int_{-d/2}^{+d/2} T_{3\lambda}\,\mathrm{d}x_3. \tag{3.21} $$

Carrying out the integration in (3.21) by taking into account (3.12)-(3.13) and the stress boundary conditions (3.17)-(3.18), the following equations are obtained:

$$ {}_0T_{\lambda 3} = \frac{3}{2}\,{}_0T_{3\lambda} - \frac{1}{2}\,{}_0\widetilde{p}_\lambda, \qquad {}_1T_{\lambda 3} = {}_1T_{3\lambda} = {}_1\widetilde{p}_\lambda. \tag{3.22} $$

Substituting them into (3.20), the three equilibrium equations take the forms

$$ {}_1T_{\kappa\lambda,\lambda} - \frac{12}{d^2}\,{}_0T_{3\kappa} + \frac{12}{d^2}\,{}_0\widetilde{p}_\kappa + \rho\,{}_1b_\kappa = 0, \tag{3.23} $$

$$ {}_0T_{33} = {}_0\widetilde{p}_3 + \frac{d^2}{8}(\,{}_1\widetilde{p}_{\lambda,\lambda} + \rho\,{}_1b_3). \tag{3.24} $$

Equation (3.24) indicates that the transverse normal stress ${}_0T_{33}$ is determined by the prescribed surface and body loads. Since ${}_1T_{33}$ is given by (3.18) and ${}_2T_{33}$ is obtained from (3.17) using (3.24), the parabolic transverse normal stress T_{33} is completely determined by the prescribed surface loads on the top and bottom faces and by the body forces. Thus, the equilibrium of the plate is described by three membrane equilibrium equations in (3.19) and two bending equilibrium equations in (3.23), written in terms of 10 independent stress coefficients.

3.3. **Equilibrated stress space using first-order stress functions.** The five two-dimensional equilibrium equations in (3.19) and (3.23) can identically be satisfied by introducing one first-order stress function vector

$$\boldsymbol{\psi}(x_\alpha, x_3) = {}_0\boldsymbol{\psi}(x_\alpha) + {}_1\boldsymbol{\psi}(x_\alpha)\, x_3 = {}_0\psi_\ell(x_\alpha)\, \boldsymbol{e}_\ell + {}_1\psi_\lambda(x_\alpha)\, x_3\, \boldsymbol{e}_\lambda \tag{3.25}$$

with component-wise transverse variations

$$\psi_\lambda(x_\alpha, x_3) = {}_0\psi_\lambda(x_\alpha) + {}_1\psi_\lambda(x_\alpha)\, x_3\,, \tag{3.26}$$

$$\psi_3(x_\alpha, x_3) = {}_0\psi_3(x_\alpha). \tag{3.27}$$

Applying the five two-dimensional stress function coefficients appearing in (3.26)-(3.27), the three membrane equilibrium equations in (3.19) can be satisfied using stress functions ${}_0\psi_\lambda$ as

$$ {}_0T_{11} = {}_0\psi_{1,2} - {}_0f_1, \qquad {}_0T_{12} = -\,{}_0\psi_{1,1}, \tag{3.28}$$

$$ {}_0T_{21} = {}_0\psi_{2,2}, \qquad {}_0T_{22} = -\,{}_0\psi_{2,1} - {}_0f_2, \tag{3.29}$$

where

$$ {}_0f_\lambda(x_\alpha) = \int_{\xi=0}^{x_\lambda} (\,{}_1\widetilde{p}_\lambda + \rho\,{}_0b_\lambda)\,\mathrm{d}\xi, \tag{3.30}$$

and the two bending equilibrium equations in (3.23) can be satisfied using stress functions ${}_0\psi_3$ and ${}_1\psi_\lambda$ as

$$ {}_0T_{31} = {}_0\psi_{3,2} - \frac{1}{2} f_{3,2}, \qquad {}_0T_{32} = -\,{}_0\psi_{3,1} - \frac{1}{2} f_{3,1}, \tag{3.31}$$

$$ {}_1T_{11} = {}_1\psi_{1,2} - {}_1f_1, \qquad {}_1T_{12} = -\,{}_1\psi_{1,1} + \frac{12}{d^2}\,{}_0\psi_3 - \frac{6}{d^2} f_3, \tag{3.32}$$

$$ {}_1T_{21} = {}_1\psi_{2,2} - \frac{12}{d^2}\,{}_0\psi_3 - \frac{6}{d^2} f_3, \qquad {}_1T_{22} = -\,{}_1\psi_{2,1} - {}_1f_2, \tag{3.33}$$

where

$$ {}_1f_\lambda(x_\alpha) = \int_{\xi=0}^{x_\lambda} (\frac{12}{d^2}\,{}_0\widetilde{p}_\lambda + \rho\,{}_1b_\lambda)\,\mathrm{d}\xi, \qquad f_3(x_\alpha) = \int_{\eta=0}^{x_2}\int_{\xi=0}^{x_1} (\,{}_1\widetilde{p}_3 + \rho\,{}_0b_3)\,\mathrm{d}\xi\,\mathrm{d}\eta. \tag{3.34}$$

Note that the stress coefficients ${}_iT_{k3},\ i = 0, 1, 2$, appearing in the truncated power series (3.13), are determined by equations (3.17)-(3.18), (3.22) and (3.24), i.e., by the surface and body loads and the stress coefficients in (3.31). According to equations (3.28)-(3.29) and (3.31)-(3.33), the equilibrium of the plate in terms of 10 independent stress coefficients can be satisfied by 5 first-order stress functions.

3.4. **Approximation of the rotation vector across the thickness.** Considering the equilibrated stress space given in Subsection 3.3 in terms of first-order stress functions, the only symmetry condition remaining to be satisfied is the symmetry of the shear stresses $T_{12} = T_{21}$. This constraint is enforced weakly through functional (3.3) by considering the rotation component $\phi_3 = \Theta_{21}$ as an independent variable. Since the shear stresses T_{12} and T_{21} are approximated by linear polynomials in x_3, according to (3.12), the corresponding Lagrange multiplier, i.e., the rotation ϕ_3, is approximated by linear polynomial as well through the thickness:

$$\phi_3(x_\alpha, x_3) \;=\; {}_0\phi_3(x_\alpha) \;+\; {}_1\phi_3(x_\alpha)\, x_3. \tag{3.35}$$

The symmetry of the in-plane shear stresses ${}_0T_{12} = {}_0T_{21}$ will be enforced by ${}_0\phi_3$, and that of the torsional stresses ${}_1T_{12} = {}_1T_{21}$ by ${}_1\phi_3$. Note that the rotation around the normal to the middle surface has also been approximated by a linear function across the thickness in [30], though in a different theoretical setting.

3.5. **Weak forms of the plate model with first-order stress functions and rotations.** The weak forms of the stress-based dimensionally reduced plate model in terms of first-order stress functions and rotations can be obtained from the three-dimensional weak forms (3.2)-(3.3) by carrying out the following steps. First, the expanded stress and rotation components (3.12)-(3.13) and (3.35), as well as the elastic compliance tensor (3.4), should be inserted in (3.2)-(3.3). Note that using $\mathbb{C}^{-1}_{ijk\ell}$ in (3.2) means that this plate model relies on unmodified three-dimensional constitutive equations. In the second step, relations (3.17)-(3.18), (3.22) and (3.24), as well as (3.28)-(3.29) and (3.31)-(3.33) should be inserted in the weak forms. Finally, by carrying out all the integrations with respect to the thickness coordinate x_3, as a third step, the following 2D weak forms of the kinematic equation and the angular momentum balance are obtained from (3.2)-(3.3):

$$\mathscr{A}(\delta\boldsymbol{\psi}, \boldsymbol{\psi}) + \mathscr{B}(\delta\boldsymbol{\psi}, \boldsymbol{\phi}) = \mathscr{P}(\delta\boldsymbol{\psi}, \widetilde{\boldsymbol{p}}) + \mathscr{U}(\delta\boldsymbol{\psi}, \widetilde{\boldsymbol{u}}), \tag{3.36}$$

$$\mathscr{B}(\delta\boldsymbol{\phi}, \boldsymbol{\psi}) \qquad\qquad = \; 0, \tag{3.37}$$

where the bilinear forms $\mathscr{A}(\delta\boldsymbol{\psi}, \boldsymbol{\psi})$ and $\mathscr{B}(\delta\boldsymbol{\phi}, \boldsymbol{\psi})$ and the linear forms $\mathscr{P}(\delta\boldsymbol{\psi}, \widetilde{\boldsymbol{p}})$ and $\mathscr{U}(\delta\boldsymbol{\psi}, \widetilde{\boldsymbol{u}})$ are detailed subsequently. An important observation is that each of the above bilinear and linear forms can be divided into a membrane part, a shear part, and a bending part. The bilinear form $\mathscr{A}(\delta\boldsymbol{\psi}, \boldsymbol{\psi})$ in (3.36) can be written as

$$\mathscr{A}(\delta\boldsymbol{\psi}, \boldsymbol{\psi}) = \mathscr{A}_m(\delta_0\psi_\lambda,\, {}_0\psi_\lambda) + \mathscr{A}_s(\delta_0\psi_3,\, {}_0\psi_3) + \mathscr{A}_b(\delta_1\psi_\lambda,\, {}_1\psi_\lambda), \tag{3.38}$$

where the membrane, shear and bending parts are given, respectively, by

$$\begin{aligned}\mathscr{A}_m(\delta_0\psi_\lambda,\, {}_0\psi_\lambda) = d\int_{\bar S}\big[\frac{1}{E}(\,&\delta_0\psi_{1,2}\, {}_0\psi_{1,2} + \delta_0\psi_{2,1}\, {}_0\psi_{2,1} + \nu\, \delta_0\psi_{1,2}\, {}_0\psi_{2,1} + \nu\, \delta_0\psi_{2,1}\, {}_0\psi_{1,2}) \\ &+ \frac{1}{4\mu}(\delta_0\psi_{1,1}\, {}_0\psi_{1,1} + \delta_0\psi_{2,2}\, {}_0\psi_{2,2} - \delta_0\psi_{1,1}\, {}_0\psi_{2,2} - \delta_0\psi_{2,2}\, {}_0\psi_{1,1})\big]\, \mathrm{d}\bar S,\end{aligned} \tag{3.39}$$

$$\mathscr{A}_s(\delta_0\psi_3,\, {}_0\psi_3) \;=\; \frac{21d}{20\mu}\int_{\bar S}(\,\delta_0\psi_{3,1}\, {}_0\psi_{3,1} + \delta_0\psi_{3,2}\, {}_0\psi_{3,2})\, \mathrm{d}\bar S, \tag{3.40}$$

$$\begin{aligned}\mathscr{A}_b(\delta_1\psi_\lambda,\, {}_1\psi_\lambda) = \frac{d^3}{12}\int_{\bar S}\big[\frac{1}{E}(\,&\delta_1\psi_{1,2}\, {}_1\psi_{1,2} + \delta_1\psi_{2,1}\, {}_1\psi_{2,1} + \nu\, \delta_1\psi_{1,2}\, {}_1\psi_{2,1} + \nu\, \delta_1\psi_{2,1}\, {}_1\psi_{1,2}) \\ &+ \frac{1}{4\mu}(\delta_1\psi_{1,1}\, {}_1\psi_{1,1} + \delta_1\psi_{2,2}\, {}_1\psi_{2,2} - \delta_1\psi_{1,1}\, {}_1\psi_{2,2} - \delta_1\psi_{2,2}\, {}_1\psi_{1,1})\big]\, \mathrm{d}\bar S,\end{aligned} \tag{3.41}$$

with elasticity modulus $E = 2\mu(1+\nu)$. Note that the membrane part depends on stress functions ${}_0\psi_\lambda$, the shear part on ${}_0\psi_3$, and the bending part on ${}_1\psi_\lambda$; i.e., the three parts, expressing the complementary virtual work of the inner forces in the plate, are uncoupled.

The bilinear form $\mathscr{B}(\delta\boldsymbol{\phi}, \boldsymbol{\psi})$ in (3.36) and (3.37) can be written as

$$\mathscr{B}(\delta\boldsymbol{\phi}, \boldsymbol{\psi}) = \mathscr{B}_m(\delta_0\phi_3,\ {}_0\psi_\lambda) + \mathscr{B}_s(\delta_1\phi_3,\ {}_0\psi_3) + \mathscr{B}_b(\delta_1\phi_3,\ {}_1\psi_\lambda), \tag{3.42}$$

where the membrane, shear and bending parts are given, respectively, by

$$\mathscr{B}_m(\delta_0\phi_3,\ {}_0\psi_\lambda) = d\int_{\bar{S}} \delta_0\phi_3\,({}_0\psi_{1,1} + {}_0\psi_{2,2})\,\mathrm{d}\bar{S}, \tag{3.43}$$

$$\mathscr{B}_s(\delta_1\phi_3,\ {}_0\psi_3) = -\frac{24}{d^3}\int_{\bar{S}} \delta_1\phi_3\,{}_0\psi_3\,\mathrm{d}\bar{S}, \tag{3.44}$$

$$\mathscr{B}_b(\delta_1\phi_3,\ {}_1\psi_\lambda) = \frac{d^3}{12}\int_{\bar{S}} \delta_1\phi_3\,({}_1\psi_{1,1} + {}_1\psi_{2,2})\,\mathrm{d}\bar{S}. \tag{3.45}$$

Note that the membrane part depends on stress functions ${}_0\psi_\lambda$ and rotation ${}_0\phi_3$, the shear part on ${}_0\psi_3$ and ${}_1\phi_3$, and the bending part on ${}_1\psi_\lambda$ and and ${}_1\phi_3$. The membrane part is uncoupled from the other two, the shear and bending parts are coupled by the rotation ${}_1\phi_3$, but not by the stress functions.

The right-hand side of the equation (3.36) contains the prescribed loads on the top and bottom faces $S^\pm$ and the prescribed displacements on the lateral surface $S^\times$. The linear form $\mathscr{P}(\delta\boldsymbol{\psi}, \widetilde{\boldsymbol{p}})$ can be written as

$$\mathscr{P}(\delta\boldsymbol{\psi}, \widetilde{\boldsymbol{p}}) = \mathscr{P}_m(\delta_0\psi_\lambda, \widetilde{\boldsymbol{p}}) + \mathscr{P}_s(\delta_0\psi_3, \widetilde{\boldsymbol{p}}) + \mathscr{P}_b(\delta_1\psi_\lambda, \widetilde{\boldsymbol{p}}), \tag{3.46}$$

where the membrane, shear and bending parts are given, respectively, by

$$\mathscr{P}_m(\delta_0\psi_\lambda, \widetilde{\boldsymbol{p}}) = \int_{\bar{S}} \frac{d\nu}{E}\,(\delta_0\psi_{1,2} - \delta_0\psi_{2,1})\,{}_0\widetilde{p}_3\,\mathrm{d}\bar{S}, \tag{3.47}$$

$$\mathscr{P}_s(\delta_0\psi_3, \widetilde{\boldsymbol{p}}) = \int_{\bar{S}} \frac{21d}{40\mu}\,(\delta\,{}_0\psi_{3,2}\,f_{3,2} - \delta\,{}_0\psi_{3,1}\,f_{3,1})\,\mathrm{d}\bar{S}, \tag{3.48}$$

$$\mathscr{P}_b(\delta_1\psi_\lambda, \widetilde{\boldsymbol{p}}) = \int_{\bar{S}} \frac{d^3\nu}{12E}\,(\delta_1\psi_{1,2} - \delta_1\psi_{2,1})\,{}_1\widetilde{p}_3 + \frac{d}{4\mu}\,(\delta_1\psi_{2,2} - \delta_1\psi_{1,1})f_3\,\mathrm{d}\bar{S}. \tag{3.49}$$

For more algebraic simplicity, the body forces and the tangential loads to the top and bottom faces are neglected in $\mathscr{P}(\delta\boldsymbol{\psi}, \widetilde{\boldsymbol{p}})$. The linear form $\mathscr{U}(\delta\boldsymbol{\psi}, \widetilde{\boldsymbol{u}})$ can be written as

$$\begin{aligned}\mathscr{U}(\delta\boldsymbol{\psi}, \widetilde{\boldsymbol{u}}) &= \mathscr{U}_m(\delta_0\psi_\kappa, \widetilde{\boldsymbol{u}}) + \mathscr{U}_s(\delta_0\psi_3, \widetilde{\boldsymbol{u}}) + \mathscr{U}_b(\delta_1\psi_\kappa, \widetilde{\boldsymbol{u}}) \\ &= \int_{\ell_u} \frac{\mathrm{d}(\delta_0\psi_\kappa)}{\mathrm{d}s}\,{}_0\widetilde{U}_\kappa\,\mathrm{d}s - \frac{12}{d^2}\int_{\ell_u} \delta_0\psi_3\,{}_1\widetilde{U}_T\,\mathrm{d}s + \int_{\ell_u} \frac{\mathrm{d}(\delta_1\psi_\kappa)}{\mathrm{d}s}\,{}_1\widetilde{U}_\kappa\,\mathrm{d}s,\end{aligned} \tag{3.50}$$

where

$${}_0\widetilde{U}_\kappa(x_\alpha) = \int_{-d/2}^{+d/2} \widetilde{u}_\kappa^\times\,\mathrm{d}x_3 = d\,{}_0\widetilde{u}_\kappa, \tag{3.51}$$

$${}_1\widetilde{U}_T(x_\alpha) = \int_{-d/2}^{+d/2} x_3\,\widetilde{\boldsymbol{u}}^\times\cdot(\boldsymbol{e}_z\times\boldsymbol{n}^\times)\,\mathrm{d}x_3 = \frac{d^3}{12}\,{}_1\widetilde{u}_T, \tag{3.52}$$

$$
{}_1\widetilde{U}_\kappa(x_\alpha) = \int_{-d/2}^{+d/2} x_3\, \widetilde{u}^{\times}_\kappa \, \mathrm{d}x_3 = \frac{d^3}{12}\, {}_1\widetilde{u}_\kappa, \tag{3.53}
$$

and ${}_1\widetilde{u}_T$ is the tangential component of the prescribed displacement vector ${}_1\widetilde{\boldsymbol{u}}$ on the lateral surface $S^{\times}$. Note that the membrane parts of the linear forms $\mathscr{P}(\delta\boldsymbol{\psi}, \widetilde{\boldsymbol{p}})$ and $\mathscr{U}(\delta\boldsymbol{\psi}, \widetilde{\boldsymbol{u}})$ depend on stress functions ${}_0\psi_\lambda$, the shear parts on ${}_0\psi_3$, and the bending parts on ${}_1\psi_\lambda$; i.e., the three parts, expressing the virtual work of the prescribed loads and displacements, are uncoupled, just like the bilinear forms (3.39)-(3.41).

4. Finite element formulation

The dual-mixed finite element formulation for the dimensionally reduced plate model, described in Section 3, is based on the the two-dimensional weak forms of the kinematic equation and the angular momentum balance equation, (3.36) and (3.37). The finite element model requires the approximation of five stress functions and two rotations. However, as pointed out in Subsection 3.5, the membrane problem can be treated and solved separately from the bending-shearing problem of the plate, just like in the case of the linear displacement-based models. The membrane model relies on the bilinear forms $\mathscr{A}_m$, $\mathscr{B}_m$ and the linear forms $\mathscr{P}_m$, $\mathscr{U}_m$, detailed in (3.39), (3.43) and (3.47), (3.50), respectively, and requires the approximation of three variables: the stress functions ${}_0\psi_\lambda$ and the rotation ${}_0\phi_3$. The bending model relies on the bilinear forms $\mathscr{A}_s$, $\mathscr{A}_b$, $\mathscr{B}_s$, $\mathscr{B}_b$, and the linear forms $\mathscr{P}_s$, $\mathscr{P}_m$, $\mathscr{U}_s$, $\mathscr{U}_b$, detailed in (3.40)-(3.41), (3.44)-(3.45) and (3.48)-(3.50), respectively, and requires the approximation of four variables: the stress functions ${}_0\psi_3$, ${}_1\psi_\lambda$ and the rotation ${}_1\phi_3$.

The subsequent developments concentrate on the finite element model and solution of the plate bending problem, as the membrane formulation and element have already been developed and presented in [19]. Stable approximation spaces for the variables ${}_1\psi_\lambda$ and ${}_1\phi_3$ can be chosen by utilizing the fact that $\mathscr{A}_b$, $\mathscr{B}_b$ and $\mathscr{U}_b$ in terms of ${}_1\psi_\lambda$ and ${}_1\phi_3$ have the same structure as $\mathscr{A}_m$, $\mathscr{B}_m$ and $\mathscr{U}_m$ in terms of ${}_0\psi_\lambda$ and ${}_0\phi_3$. The stable approximation spaces for the membrane problem in [19] have been chosen by exploiting the analogy between the weak forms of the membrane model and the displacement-pressure formulation of elasticity (or the velocity-pressure formulation of Stokes flow), for which stable approximation spaces have been developed in [31]. From the three sets of approximation spaces investigated and tested in [19] for the membrane problem, the optimal space denoted by DMX-3 is applied here for the variables ${}_1\psi_\lambda$ and ${}_1\phi_3$. The choice of the approximation spaces for the stress function ${}_0\psi_3$ is governed by the weak forms (3.44)-(3.45).

For the finite element solution of the plate problem, we consider a mesh on $\bar{S}$ that consists of convex disjoint quadrilateral elements. One element in the mesh is denoted by e. The master element $\hat{e} := \{\xi, \eta : -1 \le \xi, \eta \le 1\}$ is a square on the reference plane. We assume a smooth mapping from $\hat{e}$ to e. To introduce the approximation spaces for the element variables, let $P_p(\xi, \eta)$ denote the set of polynomials of total degree p on $\hat{e}$, and let $Q_p(\xi, \eta)$ denote the set of polynomials of degree p in each variable. The *hp* dual-mixed plate bending element is based on the following approximation spaces for $p \geq 2$:

$$
\begin{aligned}
{}_i\psi_\lambda(\xi,\eta) &\in Q_p(\xi,\eta) \cap P_{p+2}(\xi,\eta), \quad i=1,2, &(4.1)\\
{}_0\psi_3(\xi,\eta) &\in Q_{p-1}(\xi,\eta) \cap P_{p+1}(\xi,\eta), &(4.2)\\
{}_i\phi_3(\xi,\eta) &\in P_{p-1}(\xi,\eta), \quad i=1,2. &(4.3)
\end{aligned}
$$

Applying these approximation spaces, a hierarchic sequence of *hp*-version plate bending elements has been developed for $2 \leq p \leq 9$.

The error of the numerical solution in the energy norm is computed using the complementary strain energy of the stress space. A comparable error measure is guaranteed by the fact that the strain energy is equal to the complementary strain energy for a linearly elastic problem. Denoting the analytic solution for the stress space by $\boldsymbol{T}$ and the numerical solution by $\boldsymbol{T}_N$, a monotonically convergent error measure in energy norm is obtained by

$$
\| \boldsymbol{T} - \boldsymbol{T}_N \|_{E(V)} = \Big(\int_V (\boldsymbol{T} - \boldsymbol{T}_N) : \mathbb{C}^{-1} : (\boldsymbol{T} - \boldsymbol{T}_N)\, \mathrm{d}V + \frac{1}{\mu} \int_V (\boldsymbol{T}_N - \boldsymbol{T}_N^T)^2 \, \mathrm{d}V \Big)^{\frac{1}{2}}, \quad (4.4)
$$

where the second term on the right-hand side takes into account the error in the unbalanced symmetry of the computed stress space.

5. Numerical results and comparisons

In this section, the approximation capabilities of the seven-field stress-based plate model and the numerical performance of the related dual-mixed *hp* plate bending finite elements, developed and described in Sections 3 and 4, will be presented. The numerical results are obtained using a finite element research code written in the C/C++ programming language. The polynomial space over the elements is spanned by standard hierarchical basis functions based on orthogonal Legendre polynomials [9]. The numerical integrations over the elements have been performed by applying a 14-point Gaussian quadrature rule. The finite element solution is computed for the first-order stress functions and the rotations. The total number of degrees of freedom is obtained as the sum of the stress function and rotational degrees of freedom.

One of the main points of interest in the numerical analysis is the computation of the modeling error of the new plate model with respect to the three-dimensional solution for different thicknesses, and the comparison of the modeling error to those of the classical displacement-based Kirchhoff- and Reissner-Mindlin plate models. The numerical justification of the shear-locking-free property and the incompressibility-locking-free property of the dual-mixed plate element is another goal of the computations. As the present plate model relies on unmodified three-dimensional strain-stress relations, a particularly interesting case is when, applying low-order approximations, the Poisson's ratio tends to 0.5 and the thickness of the plate tends to zero, simultaneously. The performance of the plate model and the dual-mixed *hp* finite elements on distorted meshes and on plates having curvilinear boundaries is also investigated and presented.

5.1. **Simply supported square plate.** The simply supported square plate of side length $L = 1$ m and thickness d is subjected to a uniformly distributed load $q = 1$ Pa on its middle surface $\bar{S}$. The load is taken into account by prescribing $\widetilde{p}_3^+ = \widetilde{p}_3^- = q/2$ on its top and bottom faces. The material of the plate is isotropic and characterized by its elasticity modulus $E = 30$ GPa and Poisson's ratio $\nu = 0.3$. Three-dimensional benchmark solutions for this plate problem with side-length-to-thickness ratios $L/d = 10$ and $L/d = 100$ can be found in [32], obtained by applying displacement-based p-version finite elements. The main objectives of the numerical analysis are (i) the computation of the modeling error of the stress-based plate model and (ii) the performance of the dual-mixed hp plate bending element through the convergence of the relative errors in energy norm. The extrapolated 3D strain energy values reported in [32] are used for comparisons.

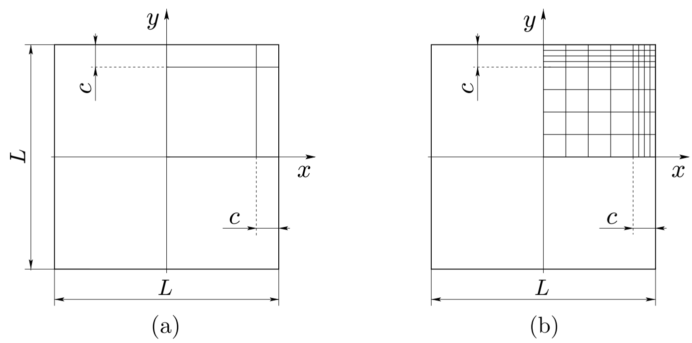

Figure 1. Graded mesh on a square plate with grading parameter c

The double symmetry of the problem allows the discretization of one quarter of the plate only. Two meshes are used for the computations: the graded mesh in Figure 1(a) containing $2 \times 2 = 4$ rectangular elements with a grading parameter denoted by c, and a refined, $8 \times 8 = 64$ element mesh shown in Figure 1(b), which is obtained by uniform division of each element in Figure 1(a) into 16 elements. Two types of simple supports are considered: soft and hard, according to the definitions given in [32].

5.1.1. *Modeling error computation for soft simple support.* The computations for the modeling error were performed using the 64-element mesh shown in Figure 1(b), applying p-extension with polynomial degree p varying from 2 to 9 (see Section 4), where p is the highest polynomial degree used for the approximation of the first-order stress functions in (3.36)-(3.37). The grading parameter is chosen to be $c = 0.1$ for $L/d = 10$, and $c = 0.03$ for $L/d = 100$ (these choices are justified by the investigations presented in Subsection 5.1.2). The convergence of the strain energy and the relative error in the energy norm with respect to the 3D reference solution are summarized in Tables 1 and 2. It can be seen that for $p > 5$, the first eight significant digits of the energy values are the same[1], indicating that the maximum capability of the 2D plate model is reached for this problem. In other words this means that the discretization

[1]The strain energy values in [32] are given in seven significant digits.

Table 1. Square plate, uniform load, soft simple support, $L/d = 10$: relative error in strain energy and in energy norm with respect to the 3D reference solution, p-extension on a graded 8×8 element mesh

p	strain energy	rel. error in energy (%)	rel. error in energy norm (%)
2	7.0799145 e –7	0.625	7.90
3	7.0593276 e –7	0.332	5.76
4	7.0591129 e –7	0.329	5.73
5	7.0591100 e –7	0.329	5.73
6	7.0591099 e –7	0.329	5.73
7	7.0591099 e –7	0.329	5.73
8	7.0591099 e –7	0.329	5.73
9	7.0591099 e –7	0.329	5.73
3D [32]	7.035974 e –7	–	–

Table 2. Square plate, uniform load, soft simple support, $L/d = 100$: relative error in strain energy and in energy norm with respect to the 3D reference solution, p-extension on a graded 8×8 element mesh

p	strain energy	rel. error in energy (%)	rel. error in energy norm (%)
2	6.2739339 e –4	2.23 e –1	4.79 e+0
3	6.2608011 e –4	1.98 e –2	1.41 e+0
4	6.2599754 e –4	6.61 e –3	8.13 e –1
5	6.2599455 e –4	6.13 e –3	7.83 e –1
6	6.2599448 e –4	6.12 e –3	7.82 e –1
7	6.2599448 e –4	6.12 e –3	7.82 e –1
8	6.2599448 e –4	6.12 e –3	7.82 e –1
9	6.2599448 e –4	6.12 e –3	7.82 e –1
3D [32]	6.259562 e –4	–	–

error becomes negligible for higher p values (using three significant digits) and the modeling error of the plate model in energy norm is 5.73 % for $L/d = 10$ (reached for $p > 3$) and 0.782 % for $L/d = 100$ (reached for $p > 4$). The comparison of these modeling errors to those of the classical Kirchhoff and Reissner-Mindlin plate models, computed in [32], is given in Table 3.

Table 3. Square plate, uniform load, soft simple support: modeling error in energy norm for different plate models

L/d	Kirchhoff plate model	Reissner-Mindlin plate model	present plate model
10	34.5 %	11.2 %	5.73 %
100	9.88 %	2.94 %	0.782 %

5.1.2. *Square plate with soft simple support: p-extension on 4-element meshes.* The capabilities of the stress-based plate model and the related dual-mixed *hp* finite elements are investigated next using the 4-element mesh shown in Figure 1a) with different grading parameters c: starting from a uniform mesh with $c = 0.25$, c takes the values of 0.1, 0.05 and 0.03. p-extension with polynomial degree p varying from 2 to 9 is applied again.

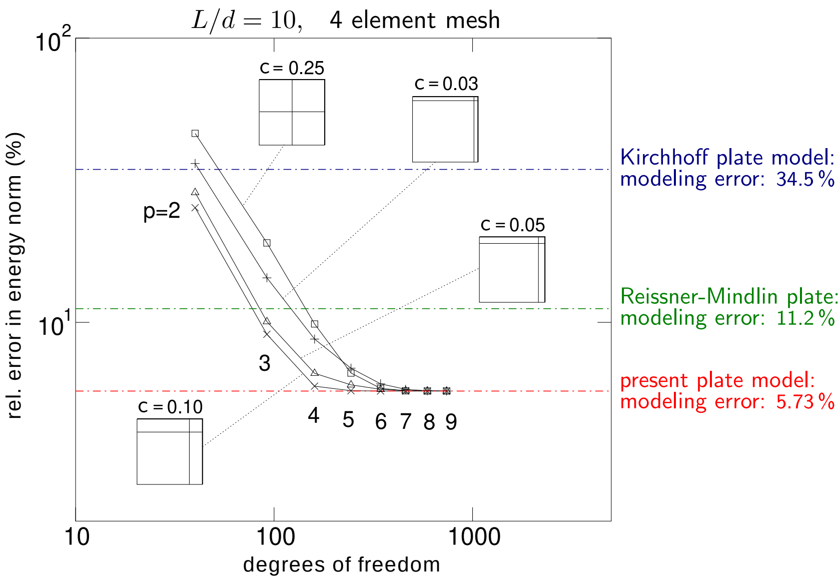

Figure 2. Square plate, uniform load, soft simple support, $L/d = 10$: convergence of the relative error in energy norm with respect to the 3D reference solution; p-extension on a 2×2 element mesh with different grading parameter c and the modeling error of plate models

Figures 2 and 3 show the convergence curves of the relative errors in energy norm with respect to the 3D reference solution for $L/d = 10$ and $L/d = 100$, respectively. Among the four graded meshes applied, the best rate of convergence is achieved when $c = 0.1$ for $L/d = 10$, and $c = 0.03$ for $L/d = 100$. The modeling errors of the different plate models (from Table 3) are illustrated by horizontal lines in the figures.

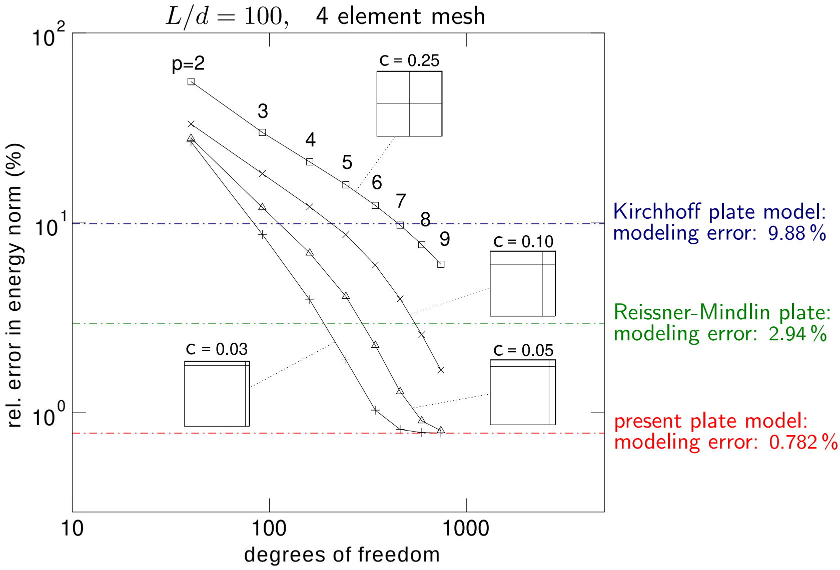

Figure 3. Square plate, uniform load, soft simple support, $L/d = 100$: convergence of the relative error in energy norm with respect to the 3D reference solution; p-extension on a 2×2 element mesh with different grading parameter c and the modeling error of plate models

Figures 2 and 3 indicate that the discretization error can be controlled by p-extension even on a 4-element mesh, and the modeling error, computed and tabulated in Table 3 using a 64-element mesh, can be reached on a properly graded 4-element mesh, as well. For $L/d = 10$, the modeling error is reached at higher polynomial degree p for all values of the grading parameter c, whereas for $L/d = 100$, the modeling error is reached when $c = 0.03$ and $p > 7$.

5.1.3. *Square plate with hard simple support.* The square plate investigated previously is considered now with hard simple support. The shear locking-free property of the dual-mixed plate bending element developed will be demonstrated through the convergence of the scaled displacement and bending moment defined by

$$\bar{u}_3 = u_3 \frac{10^2 D}{qL^4}, \qquad \bar{M}_{11} = M_{11} \frac{10}{qL^2}, \qquad D = Ed^3/12(1-\nu^2) \tag{5.1}$$

and computed at the center of the plate, where q is the applied load density on the middle surface $\bar{S}$ and D is the flexural rigidity of the plate. The computed values are compared to the Navier-series solution given in [33].

First, the approximation capability of a higher-order element with polynomial degree $p = 8$ is investigated and compared to the exact limit solution for thin plates, given in [33], using a 2×2 element mesh. In Figure 4, the scaled displacements and bending moments (5.1) are plotted and tabulated for different thicknesses as $d \to 0$. It is seen that as the side-length-to-thickness ratio goes to infinity, the displacements and bending moments converge to the exact limit solution, indicating that the plate model is asymptotically correct.

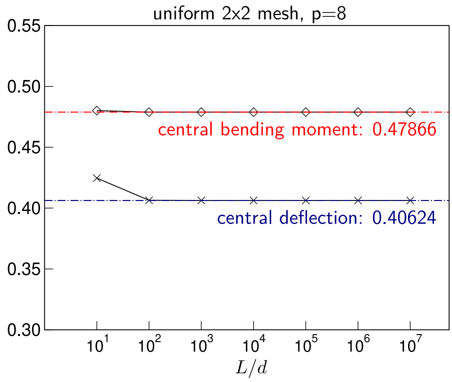

L/d	$\bar{u}_3$	$\bar{M}_{11}$
10	0.42465	0.48011
100	0.40642	0.47887
1 000	0.40624	0.47886
10 000	0.40624	0.47886
100 000	0.40624	0.47886
1 000 000	0.40624	0.47886
10 000 000	0.40624	0.47885
Series [33]	0.40624	0.47886

Figure 4. Square plate with hard simple support: scaled displacement $\bar{u}_3$ and bending moment $\bar{M}_{11}$ at the center of the plate as $d \to 0$, uniform 2×2 element mesh, $p = 8$,

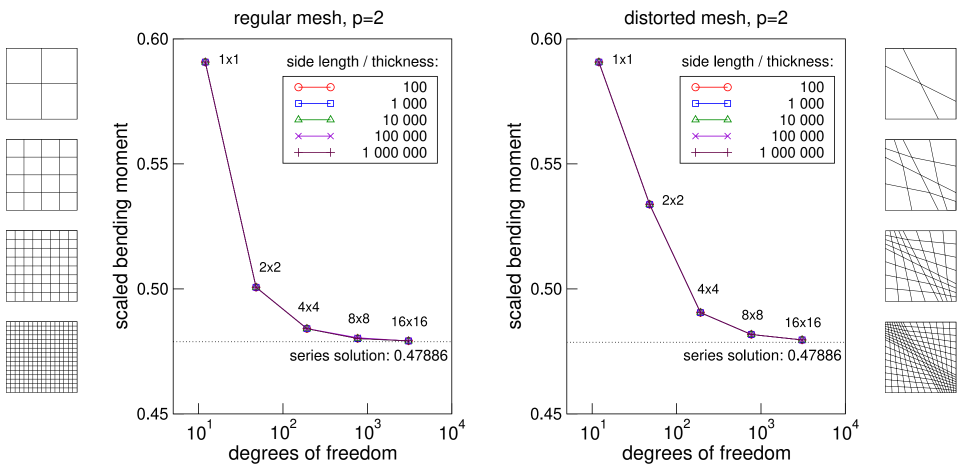

Figure 5. Square plate with hard simple support: convergence of the central bending moment for different side-length-to-thickness ratios applying dual-mixed elements and performing h-extension on regular (left) and distorted (right) meshes

Since shear locking is more likely to appear when low-order polynomial approximation is used, especially in the displacement-based models, the capability of the present plate model is investigated next by performing h-extension with polynomial degree $p = 2$ kept fixed. Note that $p = 2$ is the lowest possible polynomial degree in the stress-based plate element developed. Results were obtained by uniform mesh refinement, starting with a single element and ending with a 16×16 element mesh.

Figure 5 shows the convergence curves for the scaled bending moment at the center of the plate for five different aspect ratios, applying a regular mesh (on the left) and skew mesh with distorted elements (on the right). It is seen that the rates of convergence are not sensitive to the thickness of the plate, whether either regular or distorted elements are used. Practically, the same convergence curve was obtained for all five side-length-to-thickness ratios considered, both for regular and irregular meshes, which indicates that the dual-mixed plate bending element is completely free from shear-locking. The skew mesh gives lower rates of convergence then the regular mesh, independently of the thickness. It is also seen that a good approximation of the exact limit solution can be obtained already with a 16×16 element mesh at $p = 2$, even for the unrealistic side-length-to-thickness ratio of 10^6, which corresponds to a plate of thickness $d = 1$ μm and side length $L = 1$ m.

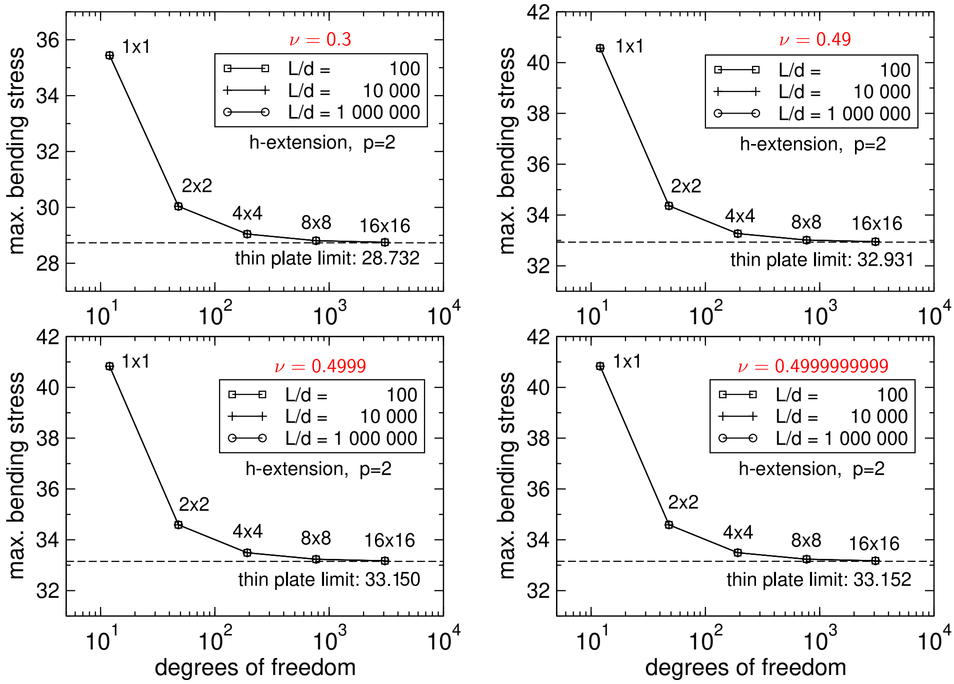

Figure 6. Square plate with hard simple support, dual-mixed element, h-extension, uniform mesh refinement: convergence of the central bending stress when the Poisson's ratio approaches 0.5 with simultaneously increased side-length-to-thickness ratio

5.1.4. *Square plate, hard simple support: h-extension with incompressibility constraint.* As the stress-based plate model relies on unmodified three-dimensional strain-stress relations, the computations were also performed by investigating the effect of the

Poisson's ratio, when it approaches to the incompressibility limit of 0.5 and, at the same time, the thickness of the plate goes to zero. Figure 6 shows the results obtained for the convergence of the maximum bending stress as $\nu \rightarrow 0.5$ and $d \rightarrow 0$, obtained by performing h-extension with regular meshes and polynomial degree $p = 2$ kept fixed. The diagrams in Figure 6 clearly indicate that the rates of convergence of the dual-mixed element is perfectly insensitive to the values of the Poisson's ratio and the thickness of the plate, i.e., the element is free from both shear locking and incompressibility locking. It can also be seen from Figure 6 that the thin plate limit values for different Poisson's ratios, computed from the Navier-series solution given in [33], are approximated well by applying a 16×16 element mesh, independently of the values of the Poisson's ratio ν and the thickness d.

5.2. **Thin circular plate with hard clamp and soft simple support.** In this example the classical problem of a circular plate is investigated in order to test the performance of the stress-based plate model and the dual-mixed hp finite elements on domains containing curved boundaries. The plate, made of isotropic material, is subjected to a uniformly distributed load $q = 1$ Pa on its middle surface $\bar{S}$. The radius of the plate is $R = 0.5$ m, the elasticity modulus is $E = 109.2$ GPa and the Poisson's ratio is $\nu = 0.3$. Two types of boundary condition are investigated: hard clamp and soft simple support.

One quarter of the plate is discretized only with prescribed symmetry conditions on the edges of symmetry. When h-extension is performed, a four-step mesh refinement shown in Figure 7 is applied by keeping $p = 2$ constant. For p-extensions, the 3-element mesh shown in Figure 7 is used. The exact mapping of the elements with curved edges was performed using the blending function method [9].

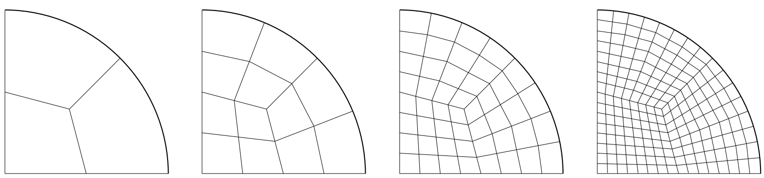

Figure 7. Circular plate problem: the mesh refinement used for h-extension

Applying hardly clamped boundary conditions, the analytic solutions for the central displacement and the boundary shear force are [34]

$$u_3 = \frac{qR^4}{64D}, \qquad Q = \frac{qR}{2}, \tag{5.2}$$

where D is given by $(5.1)_3$. For numerical comparisons, the scaled analytic displacement $\bar{u}_3 = u_3\, 10^2 D/qR^4 = 1.565$ is used. The convergences of the scaled central displacement and the shear force at the boundary are plotted in Figure 8, for both h- and p-extensions, when the diameter-to-thickness ratio is increased from 10^3 to 10^6.

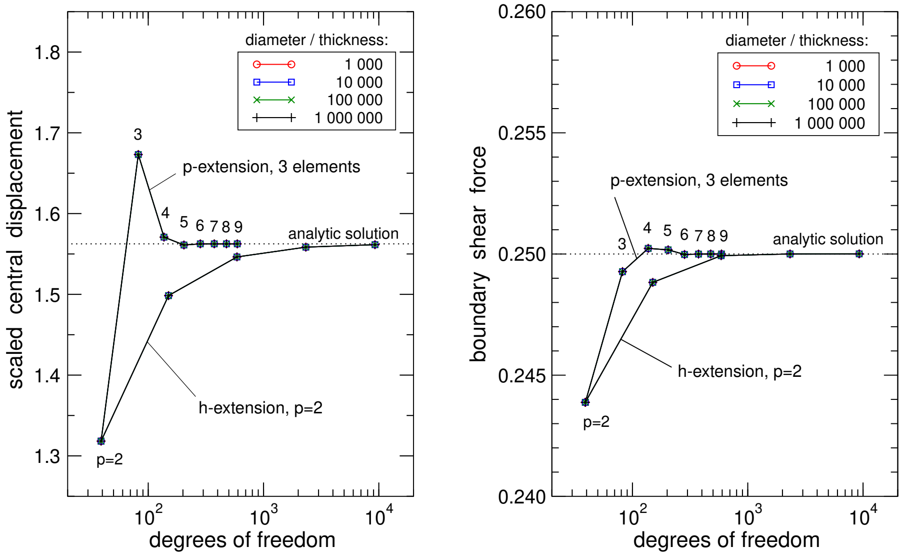

Figure 8. Hardly clamped circular plate: convergence of the scaled central displacement and the shear force at the boundary

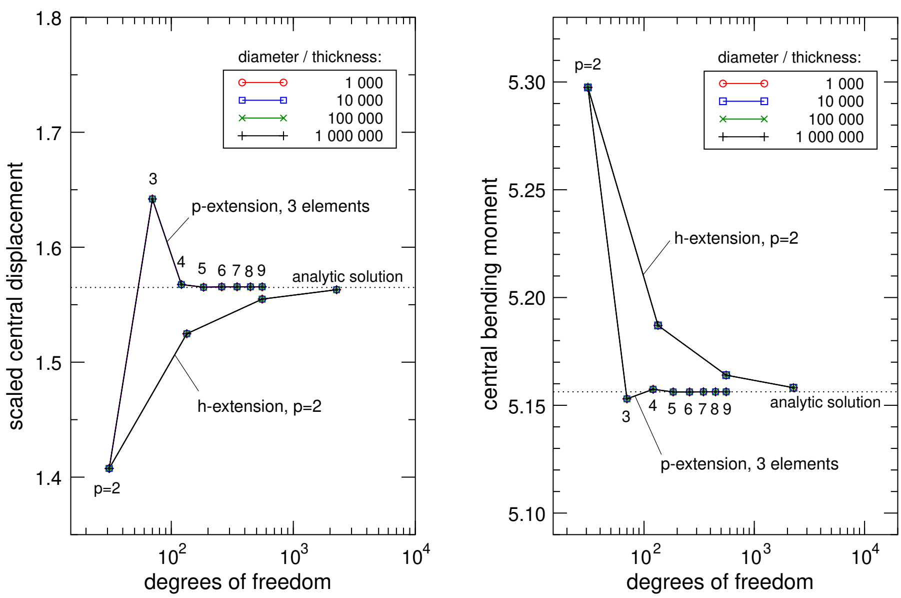

Figure 9. Simply supported circular plate: convergence of the scaled displacement and the bending moment at the center of the plate

When soft simple support is applied, the analytic solutions for the displacement and the bending moment at the center of the plate are [35]

$$u_3 = \frac{qR^4}{64D}\frac{5+\nu}{1+\nu}, \qquad M = \frac{qR^2}{16}(3+\nu), \tag{5.3}$$

where D is defined by $(5.1)_3$. For numerical comparisons, the scaled analytic displacement $\bar{u}_3 = u_3\, 10^2 D(1+\nu)/qR^4(5+\nu) = 1.565$ is used. Figure 9 shows the convergence of the scaled central displacement and the central bending moment for both h- and p-extensions, considering four diameter-to-thickness parameters with decreasing plate thickness d.

It can be seen from Figures 8 and 9 that the thickness change has no influence at all for the rates of convergences, either the displacement or the shear force or the bending moment is considered. This property seems to be independent of the applied boundary conditions as well. As expected, the p-extension on the three-element mesh gives much faster convergence for each variable than the mesh refinement with polynomial degree $p = 2$ kept fixed.

5.3. **Clamped square plate with a circular hole.** The last example is a square plate of side length $L = 2$ m with a central hole of radius $r = 0.2$ m (Figure 10). The thickness of the plate is 0.1 m, the side-length-to-thickness ratio is $L/d = 20$. The outer edge of the plate is clamped, the boundary of the circular hole is traction-free. The plate, made of isotropic material, is subjected to a uniformly distributed load with intensity $q = 1$ Pa on its middle surface. The elasticity modulus is $E = 30$ GPa and the Poisson's ratio is $\nu = 0.3$.

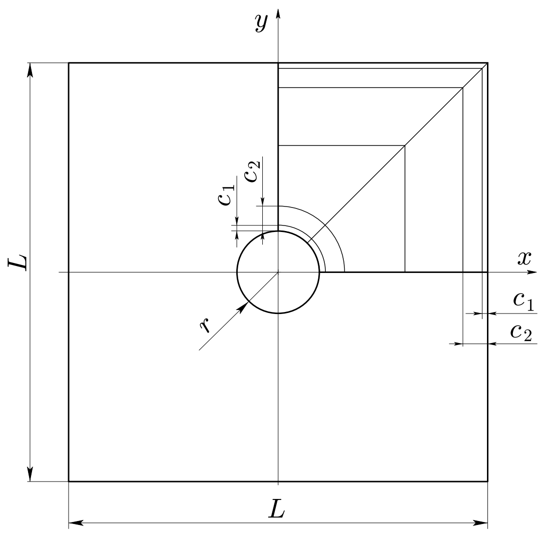

Figure 10. Clamped square plate with a circular hole and the graded 16 element mesh

A solution for this plate problem, considering a hierarchic sequence of displacement-based plated models, and the modeling error computation with respect to the 3D finite element solution can be found in [36]. The 3D solution given in [36] is considered here as a reference solution. All the computations were performed on one-quarter of the plate applying a 12-element graded mesh, shown in Figure 10. The strain energy computations correspond to this sub-domain as well. The same mesh used in [36] is applied here, the grading parameters of $c_1 = 0.03$ m and $c_2 = 0.11$ m (see Figure 10) take into account the boundary layers at the inner and outer edges of the plate. Note that the mesh contains elements with curved boundaries and straight edges as well. The blending function method [9] is used for exact mapping of the elements with curved edges.

Performing p-extension with polynomial degree $2 \leq p \leq 9$, the convergence of the strain energy and the relative discretization error in energy norm, with respect to the estimated exact strain energy of the plate model, as well as the rates of convergence in energy norm are shown in Table 4. The extrapolated exact strain energy (corresponding to $p = \infty$) of the plate model was computed from the solutions at $p = 7, 8, 9$, according to the a posteriori error estimation method described in [9].

Table 4. Clamped square plate with a central hole, uniform load, $L/d = 20$: convergence of the strain energy and the discretization error in energy norm with the rates of convergence on a graded 12 element mesh using the dual-mixed plate element with p-extension

p	DOF	strain energy	rel. error in energy norm (%)	rate of convergence
2	138	6.533638028 e−7	4.160 e+1	–
3	300	5.603839912 e−7	7.841 e+0	2.15
4	510	5.570927830 e−7	1.544 e+0	3.06
5	768	5.569858174 e−7	6.815 e−1	2.00
6	1074	5.569640950 e−7	2.729 e−1	2.73
7	1428	5.569606279 e−7	1.106 e−1	3.17
8	1830	5.569601009 e−7	5.258 e−2	3.00
9	2280	5.569599881 e−7	2.720 e−2	3.00
∞		5.569599469 e−7	–	–

The convergences of the strain energy and the relative error in the energy norm with respect to the 3D reference solution of [36] are given in Table 5. It can be seen that the discretization error becomes negligible for $p > 7$ (using 4 significant digits of precision), and the relative error of 8.000 % is the modeling error of the stress-based plate model for this problem. In Table 6, the modeling error of the present plate model is compared to those of two higher-order displacement-based plate models, referred as $(1, 1, 2)$ and $(3, 3, 2)$ in the hierarchic sequence of models in [36] (the numbers in parentheses refer to the polynomial degree of the three displacement components in

Table 5. Clamped square plate with a central hole, uniform load, $L/d = 20$: relative errors in strain energy and in energy norm with respect to the 3D reference solution on a graded 12 element mesh using the dual-mixed plate element with p-extension

p	strain energy	rel. error in energy (%)	rel. error in energy norm (%)
2	6.533638028 e−7	1.799 e+1	42.50
3	5.603839912 e−7	1.259 e+0	11.22
4	5.570927830 e−7	6.640 e−1	8.149
5	5.569858174 e−7	6.446 e−1	8.029
6	5.569640950 e−7	6.407 e−1	8.005
7	5.569606279 e−7	6.401 e−1	8.001
8	5.569601009 e−7	6.400 e−1	8.000
9	5.569599881 e−7	6.400 e−1	8.000
∞	5.569599469 e-7	6.400 e−1	8.000
3D [36]	5.534181949 e−7	–	–

the thickness direction). The results indicate that the seven-field stress-based plate model gives better modeling error than the seven-field displacement-based $(1, 1, 2)$ model, but is not as accurate as the eleven-field $(3, 3, 2)$ model.

Table 6. Clamped square plate with a central hole, uniform load, $L/d = 20$: comparison of the modeling errors in energy norm for two higher-order displacement-based plate models and the stress-based plate model

plate model	strain energy	modeling error in energy norm (%)
(1, 1, 2) [36]	5.463957687 e−7	11.26
(3, 3, 2) [36]	5.512825921 e−7	6.212
present	5.569599881 e−7	8.000
3D [36]	5.534181949 e−7	–

The convergences of the bending moments $M_x(L/2, 0)$ and $M_y(L/2, 0)$ at the mid-point of the outer boundary are shown in Figure 11, performing p-extension. It is seen that the convergence of the bending moments is very fast and their computed values for $p > 4$ are very close to the limiting values, computed as the average values of the solutions with polynomial degrees $p = 7, 8, 9$.

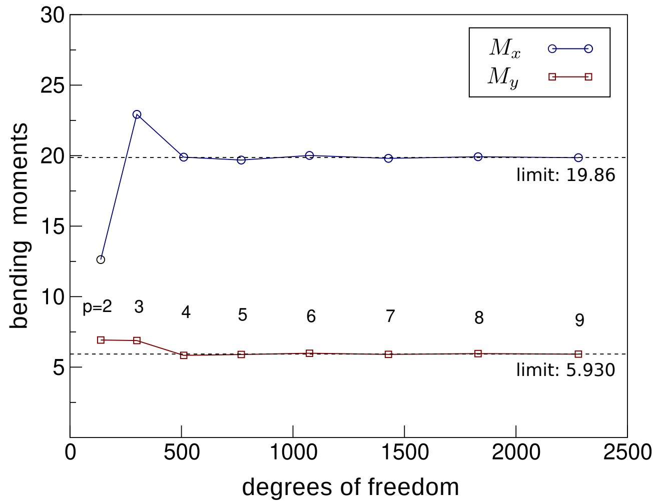

Figure 11. Clamped square plate with a central hole, uniform load, $L/d = 20$: convergence of the bending moments at the midpoint of the outer edge of the plate, performing p-extension

6. Concluding remarks

A stress-based dimensional reduction procedure has been presented for elastic plates and a related dual-mixed *hp*-version plate bending finite element model has been developed. The derivation of the plate model and the construction of the elements were based on the linearized weak forms of the kinematic equation and the angular momentum balance equation of three-dimensional non-linear elasticity. The independent variables in the formulation are the three-dimensional stresses and rotations. Their expansion into truncated power series with respect to the thickness coordinate and the satisfaction of the expanded translational equilibrium equations by the introduction of first-order stress functions have led to a seven-field dimensionally reduced plate model. Out of the seven fields, three fields describe the membrane problem and four fields describe the plate bending problem. Stable approximation spaces for the stress function and rotation components have been chosen by utilizing the analogy between the weak forms of the membrane and the bending models of the present formulation and the displacement-pressure formulation of elasticity. The plate model and the *hp* finite elements employ unmodified three-dimensional strain-stress relations.

The main interest in the numerical analysis and comparisons was twofold: firstly, the computation of the modeling error of the stress-based plate model and, secondly, the justification of the locking-free behavior of the dual-mixed finite elements. The first goal could be achieved by applying the p-extension capabilities of the element model. In the case of the problem of a uniformly loaded square plate it was shown that the modeling error of the present plate model is better than the classical displacement based first-order plate theories. The modeling error of the stress-based plate model was also compared to those of higher-order displacement-based models by solving the problem of a square plate with a central circular hole. The locking-free property of the formulation and the dual-mixed plate bending elements has been justified numerically for both h- and p-extensions by investigating the model problems of a square plate under uniform load with soft and hard simple support and a uniformly loaded circular plate with hard clamp and soft simple support. It was confirmed that the convergence properties of the hp dual-mixed elements are insensitive to the thickness change and to the value of the Poisson's ratio, i.e., the finite element model has been proved to be free from shear locking and incompressibility locking when either low-order h-, or higher-order p-version elements were applied.

References

1. Reddy, J. N. *Theory and Analysis of Elastic Plates and Shells.* 2nd. Boca Raton: CRC Press, 2007. doi: 10.1201/9780849384165.
2. Bishoff, M., Wall, W. A., Bletzinger, K. U., and Ramm, E. *Models and Finite Elements for Thin-Walled Structures. In: The Encyclopedia of Computational Mechanics Vol. II* (E. Stein, R. de Borst and T. J. R. Hughes, Eds.) pp. 59–137. New York: John Wiley & Sons, 2004. doi: 10.1002/0470091355.ecm026.
3. Chapelle, D. and Bathe, K. J. *The Finite Element Analysis of Shells – Fundamentals.* 2nd. Berlin: Springer-Verlag, 2011.
4. Yang, H. T. Y., Saigal, S., Masud, A., and Kapania, R. K. "A survey of recent shell finite elements." *International Journal for Numerical Methods in Engineering,* **47**, (2000), pp. 101–127. doi: 10.1002/(SICI)1097-0207(20000110/30)47:1/3<101::AID-NME763>3.0.CO;2-C.
5. Cen, S. and Shang, Y. "Developments of Mindlin-Reissner plate elements." *Mathematical Problems in Engineering,* Article ID 456740 (2015), pp. 3–61. doi: 10.1155/2015/456740.
6. Hakula, H., Leino, Y., and Pitkäranta, J. "Scale resolution, locking, and high-order finite element modelling of shells." *Computer Methods in Applied Mechanics and Engineering,* **133**, (1996), pp. 157–182. doi: 10.1016/0045-7825(95)00939-6.
7. Szabó, B. A. and Sahrmann, G. J. "Hierarchic plate and shell models based on p-extension." *International Journal for Numerical Methods in Engineering,* **26**, (1988), pp. 1855–1881. doi: 10.1002/nme.1620260812.
8. Arciniega, R. A. and Reddy, J. N. "Tensor-based finite element formulations for geometrically nonlinear analysis of shells." *Computer Methods in Applied Mechanics and Engineering,* **196**, (2007), pp. 1048–1073. doi: 10.1016/j.cma.2006.08.014.
9. Szabó, B. and Babuška, I. *Introduction to Finite Element Analysis. Formulation, Verification and Validation.* New York: John Wiley & Sons, 2011.
10. Bathe, K. J. *Finite Element Procedures.* Upper Saddle River, New Jersey: Prentice-Hall, 1996. doi: 10.1002/nme.1620190115.

11. Hauptmann, R. and Schweizerhof, K. “A systematic development of ’solid-shell’ element formulations for linear and non-linear analyses employing only displacement degrees of freedom.” *International Journal for Numerical Methods in Engineering,* **42**, (), pp. 49–69. doi: 10.1002/(SICI)1097-0207(19980515)42:1<49::AID-NME349>3.0.CO;2-2.
12. Wei, G., Lardeur, P., and Druesne, F. “Solid-shell approach based on first-order or higher-order plate and shell theories for the finite element analysis of thin to very thick structures.” *European Journal of Mechanics - A/Solids,* **94**, 104591, (2022). doi: 10.1016/j.euromechsol.2022.104591.
13. Boffi, D., Brezzi, F., and Fortin, M. *Mixed and Hybrid Finite Element Methods and Applications.* New York: Springer-Verlag, 2013. doi: 10.1007/978-3-642-36519-5.
14. Wiśniewski, K. *Finite Rotation Shells: Basic Equations and Finite Elements for Reissner Kinematics. Lecture Notes on Numerical Methods in Engineering and Sciences.* Dordrecht: CIMNE-Springer, 2010. doi: 10.1007/978-90-481-8761-4.
15. Fraeijs de Veubeke, B. M. “Stress function approach.” *Proceedings of the World Congress on Finite Element Methods.* Bournemouth, U.K., 1975, J.1–J.51.
16. Fraeijs de Veubeke, B. M. and Millard, A. “Discretization of stress fields in the finite element method.” *Journal of the Franklin Institute,* **302**, (1976), pp. 389–412. doi: 10.1016/0016-0032(76)90032-6.
17. Fraeijs de Veubeke, B. M. “Discretization of rotational equilibrium in the finite element method.” *Lecture Notes in Mathematics. Proceedings of the Mathematical Aspects of Finite Element Methods held in Rome, December 10–12, 1975.* Ed. by I. Galligiani and E. Magenes. Vol. 606. Berlin: Springer-Verlag, 1977, pp. 87–112.
18. Roberts, J. E. and Thomas, J. M. Mixed and Hybrid Methods. In: *Handbook of Numerical Analysis, Vol. II* (P. G. Ciarlet and J. L. Lions, Eds.) Amsterdam: North-Holland, 1991, pp. 523–639.
19. Bertóti, E. “Dual-mixed *p* and *hp* finite element methods for elastic membrane problems.” *International Journal for Numerical Methods in Engineering,* **53**, (2002), pp. 3–29. doi: 10.1002/nme.389.
20. Kocsán, L. G. “Derivation of a dual-mixed *hp*-finite element model for axisymmetrically loaded cylindrical shells.” *Archive of Applied Mechanics,* **81**, (2011), pp. 1953–1971. doi: 10.1007/s00419-011-0530-3.
21. Tóth, B. “Dual-mixed *hp* finite element model for elastic cylindrical shells.” *ZAMM Journal of Applied Mathematics and Mechanics,* **92**, (2012), pp. 236–252. doi: 10.1002/zamm.201100044.
22. Tóth, B. and Kocsán, L. G. “Comparison of dual-mixed *h*- and *p*-version finite element models for axisymmetric problems of cylindrical shells.” *Finite Element in Analysis and Design,* **65**, (2013), pp. 50–62. doi: 10.1016/j.finel.2012.11.002.

23. Tóth, B. "Hybridized dual-mixed *hp*-finite element model for shells of revolution." *Computers and Structures,* **218**, (2019), pp. 123–151. doi: 10.1016/j.compstruc.2019.03.003.
24. Tóth, B. "Natural frequency analysis of shells of revolution based on hybrid dual-mixed *hp*-finite element formulation." *Applied Mathematical Modelling,* **98**, (2021), pp. 722–746. doi: 10.1016/j.apm.2021.06.001.
25. Ogden, R. W. *Non-Linear Elastic Deformations.* (2nd ed., Dover, Mineola, 1997). Chichester: Ellis Horwood, 1984.
26. Atluri, S. N. and Cazzani, A. "Rotations in computational solid mechanics." *Archives of Computational Methods in Engineering,* **2**, (1995), pp. 49–138. doi: 10.1007/BF02736189.
27. Géradin, M. and Cardona, A. *Flexible Multibody Dynamics. A Finite Element Approach.* Chichester, England: John Wiley & Sons, 2001.
28. Fraeijs de Veubeke, B. M. "A new variational principle for finite elastic displacements." *International Journal for Engineering Sciences,* **10**, (1972), pp. 745–763. doi: 10.1016/0020-7225(72)90079-1.
29. Bertóti, E. "Indeterminacy of first-order stress functions and the stress- and rotation-based formulation of linear elasticity." *Computational Mechanics,* **14**, (1994), pp. 249–265. doi: 10.1007/BF00370076.
30. Wiśniewski, K. and Turska, E. "Kinematics of finite rotation shells with in-plane twist parameter." *Computer Methods in Applied Mechanics and Engineering,* **190**(8), (2000), pp. 1117–1135. doi: 10.1016/S0045-7825(99)00469-7.
31. Stenberg, R. and Suri, M. "Mixed *hp* finite element methods for problems in elasticity and Stokes flow." *Numerische Mathematik,* **72**, (1996), pp. 367–389. doi: 10.1007/s002110050174.
32. Babuška, I. and Scapolla, T. "Benchmark computation and performance evaluation for a rhombic plate bending problem." *International Journal for Numerical Methods in Engineering,* **28**, (1989), pp. 155–179. doi: 10.1002/nme.1620280112.
33. Timoshenko, S. P. and Woinowsky-Krieger, S. *Theory of Plates and Shells.* 2nd. New-York: McGraw-Hill, 2007.
34. Szilard, R. *Theory and analysis of plates.* NJ: Prentice-Hall: Englewood Cliffs, 1974.
35. Budynas, R. G. and Sadegh, A. M. *Roark's Formulas for Stress and Strain.* (9th edition). New York: McGraw-Hill, 2020.
36. Schwab, C. "A-posteriori error estimation for hierarchic plate models." *Proceedings of the EUROMECH 302 Conference.* Ed. by E. Sanchez-Palencia. Paris, 1993, pp. 1–21.

Journal of Computational and Applied Mechanics, Vol. 18, No. 1, (2023), pp. 35–84
DOI: 10.32973/jcam.2023.002

APPLICATION OF THE p-VERSION OF FEM TO HIERARCHIC ROD MODELS WITH REFERENCE TO MECHANICAL CONTACT PROBLEMS

István Páczelt
Institute of Applied Mechanics, University of Miskolc
3515 Miskolc-Egyetemváros, Hungary
Istvan.Paczelt@uni-miskolc.hu

Barna Szabó
Washington University in St. Louis, USA
barna.szabo@esrd.com

Attila Baksa
Institute of Applied Mechanics, University of Miskolc
3515 Miskolc-Egyetemváros, Hungary
Attila.Baksa@uni-miskolc.hu

[Received: February 22, 2023; Accepted: May 15, 2023]

Abstract. The formulation of a system of hierarchic models for the simulation of the mechanical response of slender elastic bodies, such as elastic rods, is considered. The present work is concerned with aspects of implementation and numerical examples. We use a finite element formulation based on the principle of minimum potential energy. The displacement fields are represented by the product of one-dimensional field functions and two-dimensional director functions. The field functions are approximated by the p-version of the finite element method. Our objective is to control both the model form errors and the errors of discretization with a view toward the development of advanced engineering applications equipped with autonomous error control procedures. We present numerical examples that illustrate the performance characteristics of the algorithm.

Mathematical Subject Classification: 74505, 74M15, 74K10
Keywords: Error estimation, dimensional reduction, hierarchic rod models, p-version of finite element, mechanical contact

1. Introduction

There is growing interest in the democratization of recurrent numerical simulation tasks. Democratization aims to make software tools of numerical simulation easily and broadly accessible. We argue that making data generated by numerical simulation broadly accessible makes sense only if information about its quality and reliability are provided in a form understandable by persons whose expertise is not in numerical simulation. The advantages of democratization include productivity, consistency and compatibility with simulation process and data management (SPDM) systems. On the other hand, implementation without appropriate safeguards and error control can lead to errors that may not be detected in the early phases of design.

The idea of democratization is not new. Engineering handbooks and design manuals are examples of democratization practiced in the pre-computer age. Experts solved a variety of problems in mechanics by classical methods in parametric form. Those solutions were collected and made available to engineers through handbooks.

The classical approach to democratization had a serious limitation, however: Only highly simplified problems can be solved by classical methods. Therefore the handbook entries were not the problems engineers actually needed to solve. To get a rough estimate of the quantities of interest, engineers had to find handbook entries that were close in some sense to their problem on hand. The errors were primarily model form errors, that is, errors coming from simplifications in geometry and boundary conditions.

With the maturing of numerical simulation technology it is now possible to remove the limitations of classical engineering handbooks and provide parametric solutions for the problems that engineers actually need to solve. This is the main goal of democratization. The exceptionally rare talents of engineer-scientists who had populated conventional handbooks have to be democratized, that is, mapped into the world of modern-day analysts. Other important objectives are the accumulation and preservation of corporate knowledge and increased productivity.

The types of problems that are well suited for democratization have the following characteristics: The parameter space is small, the goals of computation are clearly defined and the number of times the problems have to be solved is sufficiently large to justify the investment of creating a dedicated application.

Questions relating to the level of confidence in the accuracy of the numerical solution have to be addressed by the expert analysts who create dedicated applications. When a mathematical problem is solved by a numerical method, commonly the finite element method, then it is necessary to provide information on how large the error in the quantity of interest (QoI) is. Without such an estimate the answer is incomplete. In many cases model form error is dominant. Ideally, the model form errors and the errors of approximation are equal. Applications must be designed so as to estimate and control both types of error.

In this paper the formulation of a system of hierarchic models is considered for the simulation of the mechanical response of slender elastic bodies, such as elastic rods. The displacement fields are represented by the product of one -dimensional field functions and two-dimensional director functions in the following functional form:

$$\mathbf{u} = \mathbf{u}(x, y, s) = \sum_{m=1}^{M} \mathbf{U}_{(m)}(x, y)\, \mathbf{h}^{(m)}(s)\,, \tag{1}$$

where $\mathbf{h}^{(m)}(s)$ are the field functions of the centerline coordinate s and $\mathbf{U}_{(m)}(x, y)$ are fixed director functions of the orthogonal coordinates in the direction of the normal and binormal to the centerline, respectively. In the case of homogeneous bars the director functions are polynomials (see, for example, Szabó and Babuška [1]. In the case of bars made of laminated composites, the director functions are piecewise polynomials (Actis [2]).

The field functions usually are Lagrange or Legendre polynomials, or more recently use of B-splines and isogeometric functional has also been discussed [3, 4].

The essential features of hierarchic models are: (a) The exact solutions corresponding to a hierarchic sequence of models converge in energy norm to the exact solution of the corresponding problem of elasticity, and (b) the exact solution of each model converges in energy norm to the same limit as the exact solution of the corresponding problem of elasticity with respect to the diameter of the cross section approaching zero.

A comprehensive overview of the theory of curved bars was presented by Antmann in [5]. As evidenced by Antmann's paper, the mathematical theory of curved bars is highly developed. We are concerned here with aspects of implementation and applications to problems of engineering interest.

The formulation of hierarchic models follows the same pattern as the formulation of three-dimensional models of continuum mechanics cast in variational form. Here we will consider the displacement formulation. Since the director functions are fixed, it is possible to integrate in the plane defined by the normal and binormal to obtain a set of one-dimensional field functions $\mathbf{h}^{(m)}(s),\ m = 1, \ldots, M$. This process is called dimensional reduction or semi-discretization.

In order to satisfy the condition that the exact solution of each model must converge in energy norm to the same limit as the exact solution of the corresponding problem of elasticity with respect to the diameter of the cross section approaching zero, it is necessary to make certain adjustments in the formulation for the low-order models. The Timoshenko beam model is an example of such adjustments (for a discussion of this point see Szabó and Babuška [1]).

Without any claim to completeness, we mention some important papers on dimensionally reduction in models in the following.

There are many papers on straight or curved beams [6–14], [15], plates [16–18] and shells [19–21], subjected to static loading as well as undergoing free vibration [22–24]. Varying material properties were examined in [25, 26], rods including piezo elements in [27], rod structures exposed to thermal effects in [28], and geometrically nonlinear cases in [29–31]. Solutions of contact problems are found for hierarchical beams in the case of elastic material in [32] and in the case of elastic-plastic deformation in [33].

In [34], we find analyses of hierarchical models for plates and shells covering static and eigenvalue problems. The paper addresses the question of whether models based on Kirchhoff's hypothesis are members of the hierarchic family. The effects of the boundary layer were also investigated. The complex nature of this topic is evidenced by the hundreds of references in the article.

Our primary goal is to present numerical results that highlight the main features of hierarchic models. We examine prismatic and plane-curved rods and rods with a spiral centerline, assuming that the material is homogeneous, isotropic, linearly elastic, the load is quasi-static, and the displacements and deformations are small, i.e., boundary value problems are solved within the framework of linear elasticity theory.

The three-dimensional reference solutions were obtained using the StressCheck finite element program [35] and Abaqus program [36]. In either case error control procedures were applied to ensure that the numerical errors are negligibly small.

We pay special attention to formulating the contact problem for beams and solving it effectively. We construct a solution in which class C problems defined in [1, 37] are reduced to class B problems using a positioning technique [38, 39] whereby the boundaries of the contact regions are also element boundaries.

Few works can be found in the literature related to the p-version finite element modeling of contact problems, even in the case of small displacements and deformations: References [40, 41] examine smooth problems, an axisymmetric friction problem is solved in [42] and a 3D spatial contact problem is solved using splines in [43]. Examples of wear calculations can be found in [44]. Frictionless and frictional contact of spatial supports at large displacements are addressed in [45–48]. Examples of hierarchical modeling are presented in [49]. Parts of the structure are modeled as 3D, 2D, 1D finite elements, using special transition elements.

This paper is organized as follows: The formulation of hierarchical models is described in Section 2. The problem of frictionless contact is formulated in Section 3. Examples, highlighting various aspects of dimensionally reduced hierarchic models, are presented in Section 4. In order to simplify the discussion, details are presented in the Appendices.

2. Formulation

2.1. **Model in the local curvilinear coordinate system.** We examine a linearly elastic body with a helical centerline of pitch H wound on a cylindrical surface of radius R_o as shown in Figure 1. The position vector of the centerline is:

$$\mathbf{r} = \mathbf{r}(\bar{\varphi}) = R_0 \left(\cos(\bar{\varphi})\,\mathbf{i} + \sin(\bar{\varphi})\,\mathbf{j}\right) + \frac{H}{2\pi}\bar{\varphi}\,\mathbf{k}, \tag{2}$$

where $\bar{\varphi}$ is the angle coordinate of the cylindrical coordinate system and s is the arc coordinate of the centerline. Using the Serret-Frenet reference frame [25], the normal, binormal and tangent unit vectors $(\mathbf{n}, \mathbf{b}, \mathbf{t})$ of the local coordinate system, the curvature κ, and the twist per unit length τ are obtained. The $\mathbf{n}$, $\mathbf{b}$ axes are the principal axes of the cross section. The notation is indicated in Figure 1.

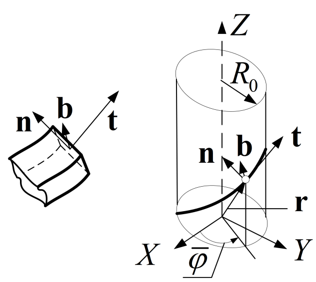

Figure 1. Centerline and unit vectors of the local coordinate system

2.2. **Displacements.** The displacement of an arbitrary point P of the body in the local curvilinear local coordinate system is given by (see Figure 2)

$$\mathbf{u} = \mathbf{u}(x, y, s) = u_n\mathbf{n} + u_b\mathbf{b} + u_t\mathbf{t} \equiv u_1\mathbf{e}_1 + u_2\mathbf{e}_2 + u_3\mathbf{e}_3\,, \tag{3}$$

where

$$\mathbf{u} = \mathbf{u}(x, y, s) = \sum_{m=1}^{M} \bar{\mathbf{h}}^{(m)}(x, y, s) = \sum_{m=1}^{M} \mathbf{U}_{(m)}(x, y)\, \mathbf{h}^{(m)}(s) \tag{4}$$

is the functional form of our approximation. The definition of

$$\bar{\mathbf{h}}^{(m)}(x, y, s)$$

depends on the choice of the hierarchic model. The function

$$\mathbf{U}_{(m)}(x, y)$$

represents the director functions. For example, letting $M = 3$, for homogeneous isotropic material we have

$$\bar{\mathbf{h}}^{(1)}(x, y, s) = \begin{bmatrix} u_{01} - y\,\chi_3 \\ u_{02} + x\,\chi_3 \\ u_{03} + y\,\chi_1 \; - x\,\chi_2 \end{bmatrix} + \begin{bmatrix} xu_{1x} \\ yu_{2y} \\ 0 \end{bmatrix} = \bar{\mathbf{h}}^{(1)0} + \bar{\mathbf{h}}^{(1)1} =$$

$$= \mathbf{U}_{(1),0}(x, y)\mathbf{h}^{(1)0}(s) + \mathbf{U}_{(1),1}(x, y)\mathbf{h}^{(1)1}(s) = \mathbf{U}_{(1)}(x, y)\mathbf{h}^{(1)}(s)\,, \tag{5a}$$

$$\bar{\mathbf{h}}^{(2)}(x, y, s) = \begin{bmatrix} (x^2\, u_{1x^2} + xy\, u_{1xy} + y^2 u_{1y^2}) \\ (x^2\, u_{2x^2} + xy\, u_{2xy} + y^2\, u_{2y^2}) \\ (x^2\, u_{3x^2} + xy\, u_{3xy} + y^2\, u_{3y^2}) \end{bmatrix} = \mathbf{U}_{(2)}(x, y)\mathbf{h}^{(2)}(s)\,, \tag{5b}$$

$$\bar{\mathbf{h}}^{(3)}(x, y, s) = \begin{bmatrix} (u_{1x^3}x^3 + u_{1x^2y}x^2y + u_{1xy^2}xy^2 + u_{1y^3}y^3) \\ (u_{2x^3}x^3 + u_{2x^2y}x^2y + u_{2xy^2}xy^2 + u_{2y^3}y^3) \\ (u_{3x^3}x^3 + u_{3x^2y}x^2y + u_{3xy^2}xy^2 + u_{3y^3}y^3) \end{bmatrix} = \mathbf{U}_{(3)}(x, y)\mathbf{h}^{(3)}(s)\,. \tag{5c}$$

Furthermore

$$\mathbf{U}_{(1),0} = \begin{bmatrix} 1 & 0 & 0 & 0 & 0 & -y \\ 0 & 1 & 0 & 0 & 0 & x \\ 0 & 0 & 1 & y & -x & 0 \end{bmatrix}, \quad \mathbf{U}_{(1),1} = \begin{bmatrix} x & 0 \\ 0 & y \\ 0 & 0 \end{bmatrix},$$

$$\mathbf{U}_{(1)} = \begin{bmatrix} 1 & 0 & 0 & 0 & 0 & -y & x & 0 \\ 0 & 1 & 0 & 0 & 0 & x & 0 & y \\ 0 & 0 & 1 & y & -x & 0 & 0 & 0 \end{bmatrix}, \tag{6a}$$

$$\mathbf{U}_{(2)} = \begin{bmatrix} x^2 & xy & y^2 & 0 & 0 & 0 & 0 & 0 & 0 \\ 0 & 0 & 0 & x^2 & xy & y^2 & 0 & 0 & 0 \\ 0 & 0 & 0 & 0 & 0 & 0 & x^2 & xy & y^2 \end{bmatrix}, \tag{6b}$$

$$\mathbf{U}_{(3)} = \begin{bmatrix} x^3 & x^2y & xy^2 & y^3 & 0 & 0 & 0 & 0 & 0 & 0 & 0 & 0 \\ 0 & 0 & 0 & 0 & x^3 & x^2y & xy^2 & y^3 & 0 & 0 & 0 & 0 \\ 0 & 0 & 0 & 0 & 0 & 0 & 0 & 0 & x^3 & x^2y & xy^2 & y^3 \end{bmatrix}, \tag{6c}$$

where $u_{1x}, u_{2y};\; u_{0i},\; \chi_i;\; u_{ix^2}\,,\; u_{ixy},\; u_{iy^2};\; u_{ix^3}, u_{ix^2y}, u_{ixy^2}, u_{iy^3}\;\; i = 1, 2, 3$ are the one-dimensional field functions of s, the monomials $1,\; x,\; y;\; x^2,\; xy,\; y^2\,; x^3, x^2y, xy^2, y^3$ are the director functions. In the classical theory of beams only the linear terms

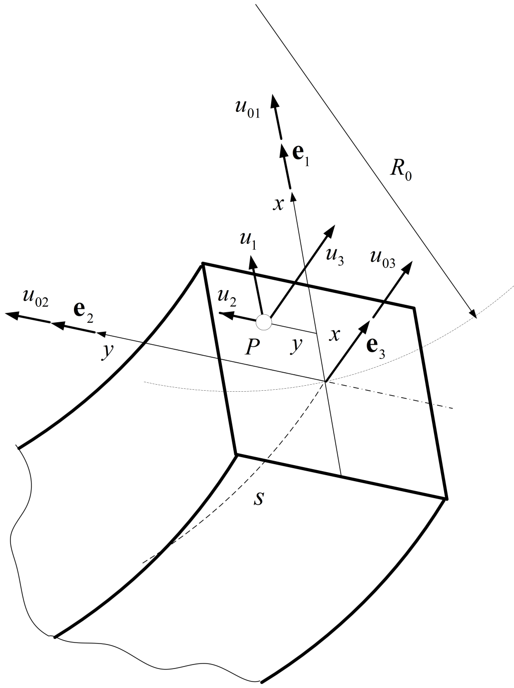

Figure 2. Notation: x, y, s – local coordinate system, $\mathbf{e}_1, \mathbf{e}_2, \mathbf{e}_3$ are the unit vectors, u_{01}, u_{02}, u_{03} are displacements of the center line, u_1, u_2, u_3 are displacements at an arbitrary point P, R_0 is the radius of cylinder

are retained. This is justified when the diameter of the cross section approaches zero. However, in practical problems one has to consider bars that have cross sections of finite diameters, in which case the higher-order terms may play an important role, depending on the goals of computation. As M increases, the solution of the fully three-dimensional problems is approximated progressively better in the norm of the formulation, in our case the energy norm, and the types of boundary conditions that can be applied increase. The director functions $\mathbf{U}_{(m)}(x, y)$ are polynomials constructed from the monomials of Pascal's triangle (see Appendix A).

2.3. **Deformations.** The deformation tensor at small deformation

$$\boldsymbol{\varepsilon} = \boldsymbol{\varepsilon}(x, y, s) = \frac{1}{2}(\mathbf{u} \otimes \nabla + \nabla \otimes \mathbf{u}) \tag{7}$$

can be calculated through a geometric equation. Here $\otimes$ denotes dyadic multiplication. The nabla operator is:

$$\nabla = \frac{\partial}{\partial x}\mathbf{e}_1 + \frac{\partial}{\partial y}\mathbf{e}_2 + \frac{R_1}{R_1 - x}\frac{\partial}{\partial s}\mathbf{e}_3 \equiv \frac{\partial}{\partial x}\mathbf{n} + \frac{\partial}{\partial y}\mathbf{b} + \frac{R_1}{R_1 - x}\frac{\partial}{\partial s}\mathbf{t} \tag{8}$$

, where $R_1 = 1/\kappa$ is the radius of curvature.

The axial and shear strains can be calculated as follows in the adopted curvilinear coordinate system:

$$\begin{gathered}
\varepsilon_1 = \frac{\partial u_1}{\partial x}, \quad \varepsilon_2 = \frac{\partial u_2}{\partial y}, \quad \varepsilon_3 = \frac{R_1}{R_1 - x}\left(\frac{\partial u_3}{\partial s} - \frac{u_1}{R_1}\right), \\
\gamma_{12} = \frac{\partial u_1}{\partial y} + \frac{\partial u_2}{\partial x}, \quad \gamma_{13} = \frac{R_1}{R_1 - x}\left(\frac{\partial u_1}{\partial s} - \tau\, u_2 + \kappa u_3\right) + \frac{\partial u_3}{\partial x}, \\
\gamma_{23} = \frac{R_1}{R_1 - x}\left(\frac{\partial u_2}{\partial s} + \tau u_1\right) + \frac{\partial u_3}{\partial y}.
\end{gathered} \tag{9}$$

It is seen from these relationships that some of the deformations depend only on the function itself and its x, y derivative, while others depend on the derivative with respect to s. We will introduce the following vectors using notation $(...)' = \partial(...)/\partial s$:

For Model 0:

$$\begin{gathered}
\mathbf{h}^{(1)0T} = [u_{01}\; u_{02}\; u_{03}\; \chi_1\; \chi_2\; \chi_3], \quad \mathbf{h}^{(1)0\,'T} = [u'_{01}\; u'_{02}\; u'_{03}\; \chi'_1\; \chi'_2\; \chi'_3] \\
\tilde{\boldsymbol{\psi}}_0^T = \tilde{\boldsymbol{\psi}}_0^T(s) = \left[\mathbf{h}^{(1)0T}\; \mathbf{h}^{(1)0\,'T}\right] = \\
= [u_{01}\; u_{02}\; u_{03}\;\; \chi_1\; \chi_2\; \chi_3\;\; u'_{01}\; u'_{02}\; u'_{03}\;\; \chi'_1\; \chi'_2\;\; \chi'_3].
\end{gathered} \tag{10}$$

For Model 1:

$$\begin{gathered}
\mathbf{h}^{(1)T} = \left[\mathbf{h}^{(1)0T}\; \mathbf{h}^{(1)1T}\right], \quad \mathbf{h}^{(1)1T} = [u_{1x},\; u_{2y}], \quad \mathbf{h}^{(1)1\,'T} = \left[u'_{1x},\; u'_{2y}\right], \\
\tilde{\boldsymbol{\psi}}_1^T = \tilde{\boldsymbol{\psi}}_1^T(s) = \left[\tilde{\boldsymbol{\psi}}_0^T\; \tilde{\boldsymbol{\psi}}^{h^{(1)1}T}\right], \\
\tilde{\boldsymbol{\psi}}^{h^{(1)1}T} = \tilde{\boldsymbol{\psi}}^{\,h^{(1)1}T}(s) = \left[\mathbf{h}^{(1)1T}\; \mathbf{h}^{(1)1'T}\right] = \left[u_{1x},\; u_{2y},\; u'_{1x},\; u'_{2y}\right].
\end{gathered} \tag{11}$$

For Model 2:

$$\begin{gathered}
\tilde{\boldsymbol{\psi}}_2^T = \tilde{\boldsymbol{\psi}}_2^T(s) = \left[\tilde{\boldsymbol{\psi}}_1^T\; \tilde{\boldsymbol{\psi}}^{h^{(2)}T}\right], \quad \tilde{\boldsymbol{\psi}}^{h^{(2)}T} = \left[\mathbf{h}^{(2)T}\; \mathbf{h}^{(2)'T}\right], \\
\mathbf{h}^{(2)T} = \left[u_{1x^2}\;\; u_{1xy}\; u_{1y^2}\; u_{2x^2}\;\; u_{2xy}\; u_{2y^2}\; u_{3x^2}\;\; u_{3xy}\; u_{3y^2}\right], \\
\mathbf{h}^{(2)'T} = \left[\; u'_{1x^2}\;\; u'_{1xy}\; u'_{1y^2}\; u'_{2x^2}\;\; u'_{2xy}\; u'_{2y^2}\; u'_{3x^2}\;\; u'_{3xy}\; u'_{3y^2}\right].
\end{gathered} \tag{12}$$

For Model 3:

$$\begin{gathered}
\tilde{\boldsymbol{\psi}}_3^T = \tilde{\boldsymbol{\psi}}_3^T(s) = \left[\tilde{\boldsymbol{\psi}}_1^T\; \tilde{\boldsymbol{\psi}}^{h^{(2)}T}\;\; \tilde{\boldsymbol{\psi}}^{h^{(3)}T}\right], \\
\tilde{\boldsymbol{\psi}}_3^T = \left[\tilde{\boldsymbol{\psi}}_2^T\;\; \tilde{\boldsymbol{\psi}}^{h^{(3)}T}\right], \quad \tilde{\boldsymbol{\psi}}^{h^{(3)}T} = \tilde{\boldsymbol{\psi}}^{h^{(3)}T}(s) = \left[\mathbf{h}^{(3)T}\; \mathbf{h}^{(3)'T}\right], \\
\mathbf{h}^{(3)T} = \left[u_{1x^3}\;\; u_{1x^2y}\; u_{1xy^2}\; u_{1y^3}\;\; u_{2x^3}\;\; u_{2x^2y}\; u_{2xy^2}\; u_{2y^3}\;\; u_{3x^3}\;\; u_{3x^2y}\; u_{3xy^2}\; u_{3y^3}\;\right].
\end{gathered} \tag{13}$$

For higher approximations we write:

$$\tilde{\boldsymbol{\psi}}_m^T = \left[\tilde{\boldsymbol{\psi}}_{m-1}^T\;\; \tilde{\boldsymbol{\psi}}^{h^{(m)}T}\right], \qquad \tilde{\boldsymbol{\psi}}^{h^{(m)}T} = \tilde{\boldsymbol{\psi}}^{h^{(m)}T}(s) = \left[\mathbf{h}^{(m)T}\; \mathbf{h}^{(m)'T}\right]. \tag{14}$$

Additional director functions are listed in Appendix A.

Based on the above, the deformation vector can be concisely written in the following form for the m-th model

$$\boldsymbol{\varepsilon} = \begin{bmatrix} \varepsilon_1 \\ \varepsilon_2 \\ \varepsilon_3 \\ \gamma_{12} \\ \gamma_{13} \\ \gamma_{23} \end{bmatrix} = [\boldsymbol{\Gamma}_1 \ \ \boldsymbol{\Gamma}_{h^{(2)}} \ ... \ \boldsymbol{\Gamma}_{h^{(m-1)}} \ \boldsymbol{\Gamma}_{h^{(m)}} \ ] \begin{bmatrix} \tilde{\boldsymbol{\psi}}_1 \\ \tilde{\boldsymbol{\psi}}^{h^{(2)}} \\ ... \\ \tilde{\boldsymbol{\psi}}^{h^{(m-1)}} \\ \tilde{\boldsymbol{\psi}}^{h^{(m)}} \end{bmatrix} = \boldsymbol{\Gamma}_m \begin{bmatrix} \tilde{\boldsymbol{\psi}}_{m-1} \\ \tilde{\boldsymbol{\psi}}^{h^{(m)}} \end{bmatrix} = \boldsymbol{\Gamma}_m \tilde{\boldsymbol{\psi}}_m, \tag{15}$$

where $\boldsymbol{\Gamma}_m(x, y)$ is generated based on the derivation relations under (9) and the field functions in $\tilde{\boldsymbol{\psi}}_m(s)$. We will approximate based on the p-version finite element

$$\tilde{\boldsymbol{\psi}}_m(s) = \mathbf{G}_m^{total}(s)\mathbf{q}^m + \boldsymbol{\Phi}_{mp}^{total}(s)\mathbf{a}^{mp} \tag{16}$$

where $\mathbf{q}^m$ comprises the nodal values, $\mathbf{a}^{mp}$ is the vector of parameters related to the internal functions, $\mathbf{G}_m^{total}(s)$, $\boldsymbol{\Phi}_{mp}^{total}(s)$ are the approximation matrices. Figure 3 shows the approximation of an arbitrary function h.

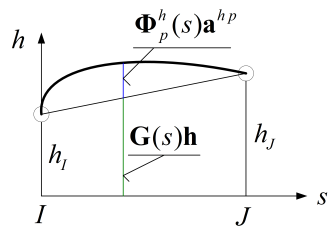

Figure 3. Approximation of field functions within a finite element

$\mathbf{G}(s)\mathbf{h}$ describes the linear change along the rod, while $\boldsymbol{\Phi}_p^h(s)$ $\mathbf{a}^{h\,p}$ provides the approximation with a higher degree (maximum p-th degree) polynomial, as indicated in Figure 3. The nodal values h_I, h_J and the additional constants in the vector $\mathbf{a}^{h\,p}$ are the unknowns. The derivation of matrices and vectors in (16) is included in Appendix B.

2.4. **Stresses.** The six independent elements of the stress tensor define the stress vector $\boldsymbol{\sigma}$ of size (6×1):

$$\boldsymbol{\sigma} = \mathbf{D}\,\boldsymbol{\varepsilon} \tag{17}$$

where $\mathbf{D}$ is the matrix of the material constants.

2.4.1. *In the case of Model-0 this is simplified.* It has the following form

$$\boldsymbol{\varepsilon}^T = [\varepsilon_3 \ \gamma_{13} \ \gamma_{23}], \quad \boldsymbol{\sigma}^T = [\sigma_3 \ \tau_{13} \ \tau_{23}], \quad \mathbf{D} = \langle E \ G \ G \rangle \ \text{ diagonal matrix} \tag{18}$$

where E is the Young's modulus, G is the shear modulus.

2.4.2. *Model-1,...,6d.* Then we have

$$\boldsymbol{\varepsilon}^T = [\varepsilon_1 \; \varepsilon_2 \; \varepsilon_3 \; \gamma_{12} \; \gamma_{13} \; \gamma_{23}] \,, \quad \boldsymbol{\sigma}^T = [\sigma_1 \; \sigma_2 \; \sigma_3 \; \tau_{12} \tau_{13} \; \tau_{23}] \,. \tag{19}$$

For these cases matrix $\mathbf{D}$ is a (6×6) material constant matrix corresponding to the 3D state of stress.

2.5. **Potential energy.** The total potential energy is [1] is given by

$$\Pi_p = \frac{1}{2} \int_V \boldsymbol{\varepsilon}^T \mathbf{D} \, \boldsymbol{\varepsilon} \, dV - W^{work} = \frac{1}{2} \int_L \tilde{\boldsymbol{\psi}}_m^T \Big(\int_S \boldsymbol{\Gamma}_m^T \mathbf{D} \, \Gamma_m \, dS \Big) \tilde{\boldsymbol{\psi}}_m ds - W^{work}, \tag{20}$$

where W^{work} is the work of the external load and the integral over the volume was written as the product of two integrals, one over the length coordinate s, the other over the the cross section S. The integral over the cross section is a function of s,

$$\tilde{\mathbf{D}}_m = \int_S \boldsymbol{\Gamma}_m^T \mathbf{D} \, \boldsymbol{\Gamma}_m \, dS. \qquad m = 1, \ldots, 6 \tag{21}$$

Thus the potential energy is

$$\Pi_p = \frac{1}{2} \int_L \tilde{\boldsymbol{\psi}}_m^T \, \tilde{\boldsymbol{D}}_m \, \tilde{\boldsymbol{\psi}}_m ds - W^{work}. \qquad m = 1, \ldots, 6 \tag{22}$$

The integration should be performed over the domain of s. Using the relations

$$\mathbf{q} = \mathbf{q}^m, \; \mathbf{a} = \mathbf{a}^{mp}, \quad \tilde{\mathbf{D}} = \tilde{\mathbf{D}}_m = \int_S \boldsymbol{\Gamma}_m^T \mathbf{D} \boldsymbol{\Gamma}_m \, dS, \quad \mathbf{G} = \mathbf{G}_m^{total} \; \text{ and } \; \boldsymbol{\Phi} = \boldsymbol{\Phi}_{mp}^{total}$$

the potential energy can be rewritten into the form

$$\Pi_p = \frac{1}{2} \int_L (\mathbf{q}^T \mathbf{G}^T + \mathbf{a}^T \boldsymbol{\Phi}^T) \, \tilde{\mathbf{D}} \, (\mathbf{G}\mathbf{q} + \boldsymbol{\Phi}\mathbf{a}) \, ds - W^{work} = U - W^{work} \tag{23}$$

from which the functional form of the stiffness matrix is yielded as

$$\mathbf{K} = \begin{bmatrix} \mathbf{K}_{qq} & \mathbf{K}_{qa} \\ \mathbf{K}_{aq} & \mathbf{K}_{aa} \end{bmatrix}, \quad \mathbf{K}_{qq} = \int_L \mathbf{G}^T \, \tilde{\mathbf{D}} \, \mathbf{G} \, ds, \tag{24a}$$

$$\mathbf{K}_{aa} = \int_L \boldsymbol{\Phi}^T \, \tilde{\mathbf{D}} \, \boldsymbol{\Phi} \, ds, \quad \mathbf{K}_{qa} = \int_L \mathbf{G}^T \, \tilde{\mathbf{D}} \, \boldsymbol{\Phi} \, ds = \mathbf{K}_{aq}^T. \tag{24b}$$

The reduced load vector is given by $\mathbf{f}^T = \left[\mathbf{f}_q^T \; \mathbf{f}_a^T \right]$.

Finally, eliminating the internal variables, the reduced stiffness matrix and load vector are obtained:

$$\mathbf{K}_{red} = \mathbf{K}_{qq} - \mathbf{K}_{qa} (\mathbf{K}_{aa})^{-1} \mathbf{K}_{aq}, \quad \mathbf{f}_{red} = \mathbf{f}_q - \mathbf{K}_{qa} (\mathbf{K}_{aa})^{-1} \mathbf{f}_a. \tag{25}$$

The internal variables are recovered in the post-solution process using the relationship

$$\mathbf{a} = (\mathbf{K}_{aa})^{-1} \mathbf{f}_a - (\mathbf{K}_{aa})^{-1} \mathbf{K}_{aq} \mathbf{q}. \tag{26}$$

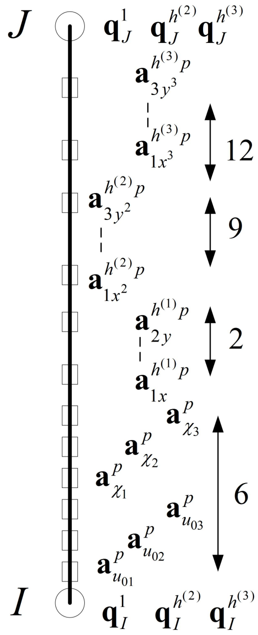

Figure 4. Unknowns associated with the external and internal nodes of the finite element belonging to the $h3$ model

2.6. **The load vectors.**

1. In the case of the $h0$ model the applied loads, as well as the stress resultants, are functions of the center line coordinate.
2. In the case of the $h1, h2, h3, \dots$ models, we calculate the work of the loads distributed on the surface. The process is illustrated for the $h3$ model in the following. The approximate displacement field for this model is calculated based on (4). Collecting the functions depending on s, we write:

$$\boldsymbol{\psi}_3^{displ} = \boldsymbol{\psi}_3^{displ}(s) = \begin{bmatrix} \mathbf{u}_0(s) \\ \boldsymbol{\chi}(s) \\ \mathbf{h}^{(1)1}(s) \\ \mathbf{h}^{(2)}(s) \\ \mathbf{h}^{(3)}(s) \end{bmatrix} = \begin{bmatrix} \mathbf{h}^{(1)}(s) \\ \mathbf{h}^{(2)}(s) \\ \mathbf{h}^{(3)}(s) \end{bmatrix} = \mathbf{R}^3_{red} \begin{bmatrix} \mathbf{h}^{(1)}(s) \\ \mathbf{h}^{(1)'}(s) \\ \mathbf{h}^{(2)}(s) \\ \mathbf{h}^{(2)'}(s) \\ \mathbf{h}^{(3)}(s) \\ \mathbf{h}^{(3)'}(s) \end{bmatrix} = \mathbf{R}^3_{red}\, \tilde{\boldsymbol{\psi}}_3(s), \quad (27)$$

where the operator $\mathbf{R}^3_{red(29,58)}$ produces the displacements $\boldsymbol{\psi}_3^{displ}$ from the $\boldsymbol{\psi}_3$ vector, including the derivatives. Therefore the displacement vector defined in (4), taking into account (27), is

$$\mathbf{u} = \mathbf{u}(x,y,s) = \left[\mathbf{U}_{(1)}\ \mathbf{U}_{(2)}\ \mathbf{U}_{(3)}\right] \boldsymbol{\psi}_3^{displ} = \\ = \mathbf{U}^3(x,y)\boldsymbol{\psi}_3^{displ}(s) = \mathbf{U}^3(x,y)\mathbf{R}^3_{red}\tilde{\boldsymbol{\psi}}_3(s). \quad (28)$$

Furthermore, in a view of (16) we have

$$\tilde{\boldsymbol{\psi}}_3(s) = \mathbf{G}^{total}(s)\ \mathbf{q}^{total} + \boldsymbol{\Phi}^{total}(s)\ \mathbf{a}^{total}. \tag{29}$$

Hence the work of the load acting on the surface S_{load} is

$$W^{work} = \int\limits_{S_{load}} \tilde{\boldsymbol{\psi}}_3^T(s) \mathbf{R}_{red}^{3,T}\ \mathbf{U}^{3,T}(x,y)\ \mathbf{p}_{load}(x,y,s)\ dS, \tag{30}$$

from which the reduced load vectors are calculated. When the load is a function of x, y (i.e. the load acts on the cross-section of the bar, marked I or J) and the cross section of the body is rectangular, with dimensions a, b in the x and y directions, then the distributed load can be written as

$$\mathbf{p}_{load} = \begin{bmatrix} \tau_{13}^0 \left(1 - \left(\frac{x}{a/2}\right)^2\right) \\ \tau_{23}^0 \left(1 - \left(\frac{y}{b/2}\right)^2\right) \\ \sigma^0 - \frac{\sigma^+}{b/2} y \end{bmatrix} \tag{31}$$

where $\tau_{13}^0,\ \ \tau_{23}^0,\ \ \sigma^0,\ \ \sigma^+$ are given quantities. Then the work of the load is

$$W^{work} = \tilde{\boldsymbol{\psi}}_3^T(s_{I(J)}) \mathbf{R}_{red}^{3,T} \int\limits_{S_{I(J)}} \mathbf{U}^{3,T}(x,y)\ \mathbf{p}_{load}(x,y)\, dS_{xy}\,. \tag{32}$$

With (32) the reduced load vectors are

$$\begin{aligned} \mathbf{f}_q &= \left(\mathbf{G}^{total,T}(s_{I(J)})\right) \mathbf{R}_{red}^{3,T} \int\limits_{S_{I(J)}} \mathbf{U}^{3,T}(x,y)\ \mathbf{p}_{load}(x,y)\ dS_{xy}\,, \\ \mathbf{f}_a &= \left(\boldsymbol{\Phi}^{total,T}(s_{I(J)})\right) \mathbf{R}_{red}^{3,T} \int\limits_{S_{I(J)}} \mathbf{U}^{3,T}(x,y)\ \mathbf{p}_{load}(x,y)\ dS_{xy}\,. \end{aligned} \tag{33}$$

If the load is exerted on a planar surface defined by $x = -a/2$ then

$$W^{work} = \int\limits_{S_{load}} \tilde{\boldsymbol{\psi}}_3^T(s) \mathbf{R}_{red}^{3,T}\ \mathbf{U}^{3,T}(x=-a/2,y)\ \mathbf{p}_{load}(y,s)\ dS_{ys}. \tag{34}$$

The procedure is analogous for the other hierarchic models.

2.7. **Treatment of elastic foundation.** Let us assume that on the surface $y = b/2$ a ring-shaped body is in contact with a Winkler-type foundation characterized by spring constant c. Then the strain energy is

$$U^{found} = \frac{1}{2} \int\limits_{S_{found}} u_y(x, y=b/2, s)\ c u_y(x, y=b/2, s)\ dS_{xs}\,. \tag{35}$$

Therefore, in view of the approximation of $\mathbf{u}(x, y, s)$ under (28) we get

$$u_y = \mathbf{u}(x,y,s)^T \mathbf{e}_2 = \left(\mathbf{u}(x,y,s)^T \mathbf{e}_2\right)^T = \mathbf{e}_2^T \mathbf{u}(x,y,s) = \mathbf{u}(x,y,s)^T \begin{bmatrix} 0 \\ 1 \\ 0 \end{bmatrix} =$$

$$[0\;1\;0]\,\mathbf{u}(x,y,s) = \tilde{\boldsymbol{\psi}}_3^T(s)\mathbf{R}_{red}^{3,T}\mathbf{U}^{3,T}(x,y) \begin{bmatrix} 0 \\ 1 \\ 0 \end{bmatrix} = [0\;1\;0]\,\mathbf{U}^3(x,y)\mathbf{R}_{red}^3\tilde{\boldsymbol{\psi}}_3(s), \quad (36)$$

that is

$$U^{found} = \frac{1}{2} \int\limits_{S_{found}} \tilde{\boldsymbol{\psi}}_3^T(s)\mathbf{R}_{red}^{3,T}\mathbf{U}^{3,T}(x,y=b/2) \begin{bmatrix} 0 & 0 & 0 \\ 0 & c & 0 \\ 0 & 0 & 0 \end{bmatrix} \mathbf{U}^3(x,y=b/2)\mathbf{R}_{red}^3\tilde{\boldsymbol{\psi}}_3(s)dS_{xs}\,. \quad (37)$$

Using (29), omitting the upper index and performing the integrations, the energy is written in the form

$$U^{found} = \frac{1}{2}\left[\mathbf{q}^T\;\mathbf{a}^T\right] \begin{bmatrix} \mathbf{C}_{qq} & \mathbf{C}_{qa} \\ \mathbf{C}_{aq} & \mathbf{C}_{aa} \end{bmatrix} \begin{bmatrix} \mathbf{q} \\ \mathbf{a} \end{bmatrix}, \quad (38)$$

where the stiffness matrix of the elastic support is

$$\mathbf{C} = \begin{bmatrix} \mathbf{C}_{qq} & \mathbf{C}_{qa} \\ \mathbf{C}_{aq} & \mathbf{C}_{aa} \end{bmatrix}$$

in which

$$\mathbf{C}_{qq} = \int\limits_{S_{xs}} \mathbf{G}^T\mathbf{W}\,\mathbf{G}\,dS_{xs}\,, \quad \mathbf{C}_{aa} = \int\limits_{S_{xs}} \boldsymbol{\Phi}^T\,\mathbf{W}\,\boldsymbol{\Phi}\,dS_{xs}\,, \quad \mathbf{C}_{qa} = \int\limits_{S_{xs}} \mathbf{G}^T\,\mathbf{W}\,\boldsymbol{\Phi} dS_{xs} = \mathbf{C}_{aq}^T$$

and

$$\mathbf{W} = \mathbf{W}\,(x,y=b/2) = \mathbf{R}_{red}^{3,T}\mathbf{U}^{3,T}(x,y=b/2) \begin{bmatrix} 0 & 0 & 0 \\ 0 & c & 0 \\ 0 & 0 & 0 \end{bmatrix} \mathbf{U}^3(x,y=b/2)\mathbf{R}_{red}^3.$$

3. Formulation of frictionless contact problem

3.1. **General equations.** The line of thought in this subsection is based on [38, 39, 50, 51]. Let the displacement of the bodies in the normal direction of contact $\mathbf{n}_c$ be $u^i = \mathbf{u}^i \cdot \mathbf{n}_c$, $i = 1, 2$, and g be the initial gap in the contact region S_c – see Figure 5.

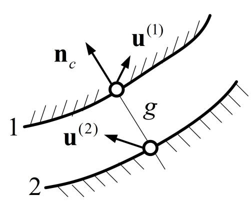

Figure 5. Bodies in contact. Notations

There is contact when $d = u_n^{(1)} - u_n^{(2)} + g = 0$ and $p_n \geqslant 0$, while a gap is present if $d = u_n^{(1)} - u_n^{(2)} + g > 0$ and $p_n = 0$, where d is the gap formed after deformation and p_n is the contact pressure.

The $p_n d = 0$ condition is fulfilled over the entire S_c domain. Solving the contact problem with the augmented Lagrange multiplier method [17, 28, 32, 42], it is necessary to incorporate the contact penalty energy:

$$U^{cont} = \frac{1}{2}\int\limits_{S_c} d^- \, c_n \, d^- \, dS_c = \frac{1}{2}\int\limits_{S_c} (u_n^{(1)} - u_n^{(2)} + g) c_n \, (u_n^{(1)} - u_n^{(2)} + g) \, dS_c \tag{39}$$

and the Lagrangian term:

$$W_{aug} = \int\limits_{S_c} p_n d \, dS = \int\limits_{S_c} p_n (u_n^{(1)} - u_n^{(2)} + g) dS, \tag{40}$$

where $d^- \leq 0$, $c_n >> 0$ is the penalty parameter. The displacement in the normal direction is given by

$$u_n^{(i)} = \mathbf{n}_c \cdot \mathbf{u}^{(i)} = \mathbf{n}^T \mathbf{u}^{(i)}, \qquad i = 1, 2.$$

The total energy, the minimum of which is sought subject to the stated inequalities, is:

$$L_{aug} = \Pi_p - W_{aug} + U^{cont}. \tag{41}$$

Considering the relation $u_n^{(i)} = \mathbf{n}_c \cdot \mathbf{u}^{(i)} = \mathbf{n}^T \mathbf{u}^{(i)}$ and using (28), (29) for the displacement of the i-th body in the normal direction on the surface $y_b^{(i)}$(the formulae are general, so we ignore the reference to the $h3$ model, the index 3), we get

$$\begin{aligned} u_n^{(i)} &= \mathbf{n}^T \mathbf{U}^{(i)}(x, y_b^{(i)}) \mathbf{R}_{red} \left(\mathbf{G}^{(i)}(s) \mathbf{q}^{(i)} + \mathbf{\Phi}^{(i)}(s) \mathbf{a}^{(i)} \right) = \\ &= \mathbf{n}^T \tilde{\mathbf{U}}^{(i)}(x, y_b^{(i)}) \left(\mathbf{G}^{(i)}(s) \mathbf{q}^{(i)} + \mathbf{\Phi}^{(i)}(s) \mathbf{a}^{(i)} \right) \end{aligned} \tag{42}$$

and, defining $\mathbf{C}_n = c_n \, \mathbf{n}^T \mathbf{n}$, the penalty energy given in (39), neglecting the constant term from the initial gap, is written in compact form:

$$U^{cont} = \frac{1}{2} \left[\mathbf{a}^T \mathbf{q}^T \right] \left(\begin{bmatrix} \mathbf{C}_{qq} & \mathbf{C}_{qa} \\ \mathbf{C}_{aq} & \mathbf{C}_{aa} \end{bmatrix} \begin{bmatrix} \mathbf{q} \\ \mathbf{a} \end{bmatrix} - 2 \begin{bmatrix} \mathbf{f}_{cq} \\ \mathbf{f}_{ca} \end{bmatrix} \right) = \frac{1}{2} \tilde{\mathbf{q}}^T \left(\tilde{\mathbf{C}} \, \tilde{\mathbf{q}} - 2\tilde{\mathbf{f}} \right), \tag{43}$$

where

$$\mathbf{q}^T = \left[\mathbf{q}^{(1)T} \; \mathbf{q}^{(2)T} \right], \qquad \mathbf{a}^T = \left[\mathbf{a}^{(1)T} \; \mathbf{a}^{(2)T} \right],$$

$$\mathbf{C}_{qq} = \int\limits_{S_c} \begin{bmatrix} \mathbf{G}^{(1)T} \tilde{\mathbf{U}}^{(1)T} \mathbf{C}_n \tilde{\mathbf{U}}^{(1)} \mathbf{G}^{(1)} & -\mathbf{G}^{(1)T} \tilde{\mathbf{U}}^{(1)T} \mathbf{C}_n \tilde{\mathbf{U}}^{(2)} \mathbf{G}^{(2)} \\ -\mathbf{G}^{(2)T} \tilde{\mathbf{U}}^{(2)T} \mathbf{C}_n \tilde{\mathbf{U}}^{(1)} \mathbf{G}^{(1)} & \mathbf{G}^{(2)T} \tilde{\mathbf{U}}^{(2)T} \mathbf{C}_n \tilde{\mathbf{U}}^{(2)} \mathbf{G}^{(2)} \end{bmatrix} dS_c \,,$$

$$\mathbf{f}_{cq} = -\int\limits_{S_c} c_n \begin{bmatrix} \mathbf{G}^{(1)T} \tilde{\mathbf{U}}^{(1)T} \mathbf{n} g \\ -\mathbf{G}^{(2)T} \tilde{\mathbf{U}}^{(2)T} \mathbf{n} g \end{bmatrix} dS_c \,,$$

$$\mathbf{C}_{aq} = \mathbf{C}_{qa}^T = \int\limits_{S_c} \begin{bmatrix} \mathbf{\Phi}^{(1)T} \tilde{\mathbf{U}}^{(1)T} \mathbf{C}_n \tilde{\mathbf{U}}^{(1)} \mathbf{G}^{(1)} & -\mathbf{\Phi}^{(1)T} \tilde{\mathbf{U}}^{(1)T} \mathbf{C}_n \tilde{\mathbf{U}}^{(2)} \mathbf{G}^{(2)} \\ -\mathbf{\Phi}^{(2)T} \tilde{\mathbf{U}}^{(2)T} \mathbf{C}_n \tilde{\mathbf{U}}^{(1)} \mathbf{G}^{(1)} & \mathbf{\Phi}^{(2)T} \tilde{\mathbf{U}}^{(2)T} \mathbf{C}_n \tilde{\mathbf{U}}^{(2)} \mathbf{G}^{(2)} \end{bmatrix} dS_c \,,$$

$$\mathbf{C}_{aa} = \int\limits_{S_c} \begin{bmatrix} \mathbf{\Phi}^{(1)T}\tilde{\mathbf{U}}^{(1)T}\mathbf{C}_n\tilde{\mathbf{U}}^{(1)}\mathbf{\Phi}^{(1)} & -\mathbf{\Phi}^{(1)T}\tilde{\mathbf{U}}^{(1)T}\mathbf{C}_n\tilde{\mathbf{U}}^{(2)}\mathbf{\Phi}^{(2)} \\ -\mathbf{\Phi}^{(2)T}\tilde{\mathbf{U}}^{(2)T}\mathbf{C}_n\tilde{\mathbf{U}}^{(1)}\mathbf{\Phi}^{(1)} & \mathbf{\Phi}^{(2)T}\tilde{\mathbf{U}}^{(2)T}\mathbf{C}_n\tilde{\mathbf{U}}^{(2)}\mathbf{\Phi}^{(2)} \end{bmatrix} dS_c\,,$$

$$\mathbf{f}_{ca} = -\int\limits_{S_c} c_n \begin{bmatrix} \mathbf{\Phi}^{(1)T}\tilde{\mathbf{U}}^{(1)T}\mathbf{n}g \\ -\mathbf{\Phi}^{(2)T}\tilde{\mathbf{U}}^{(2)T}\mathbf{n}g \end{bmatrix} dS_c\,,$$

and $\tilde{\mathbf{C}}$, $\tilde{\mathbf{f}}$ are the stiffness matrix and load vector of the contact element, respectively. When $u_n^{(1)} = 0$, then we get the stiffness matrix of the Winkler-type foundation for body 2.

The work term corresponding to augmentation is:

$$W_{aug} = \int\limits_{S_c} p_n d\, dS = \int\limits_{S_c} p_n(\mathbf{q}^{(1),T}\mathbf{G}^{(1)T}\tilde{\mathbf{U}}^{(1)T}\mathbf{n} - \mathbf{q}^{(2),T}\mathbf{G}^{(2)T}\tilde{\mathbf{U}}^{(2)T}\mathbf{n} + g)dS +$$
$$+ \int\limits_{S_c} p_n(\mathbf{a}^{(1),T}\mathbf{\Phi}^{(1)T}\tilde{\mathbf{U}}^{(1)T}\mathbf{n} - \mathbf{a}^{(2),T}\mathbf{\Phi}^{(2)T}\tilde{\mathbf{U}}^{(2)T}\mathbf{n})dS,$$

that is

$$W_{aug} = \mathbf{q}^T\mathbf{f}_{aug,q} + \mathbf{a}^T\mathbf{f}_{aug,a}\,, \tag{44a}$$

where

$$\mathbf{f}_{aug,q} = \begin{bmatrix} \int\limits_{S_c} p_n\mathbf{G}^{(1)T}\tilde{\mathbf{U}}^{(1)T}\mathbf{n}\, dS \\ -\int\limits_{S_c} p_n\mathbf{G}^{(2)T}\tilde{\mathbf{U}}^{(2)T}\mathbf{n}\, dS \end{bmatrix}, \quad \mathbf{f}_{aug,a} = \begin{bmatrix} \int\limits_{S_c} p_n\mathbf{\Phi}^{(1)T}\tilde{\mathbf{U}}^{(1)T}\mathbf{n}\, dS \\ -\int\limits_{S_c} p_n\mathbf{\Phi}^{(2)T}\tilde{\mathbf{U}}^{(2)T}\mathbf{n}\, dS \end{bmatrix}. \tag{44b}$$

In the iterative solution process the contact pressure is calculated from the following formula using Macaulay brackets

$$p_n^{(j+1)} = \left\langle p_n^{(j)} - c_n d^{(j)} \right\rangle, \qquad x^{(j+1)} = \left\langle \frac{x^{(j)} + \left|x^{(j)}\right|}{2} \right\rangle. \tag{45}$$

The iteration process is started by solving the problem using the penalty method and continued by incrementing the pressure where the term in parenthesis is positive, and setting the value of c_n to zero where it is negative. This gives us the modified contact stiffness and load vector. The iteration process is generally stable when the c_n value is sufficiently small.

3.2. **Model in the global coordinate system.**

3.2.1. *Hierarchical bar elements in cases when the displacement field is approximated by Taylor or Legendre polynomials.* The displacement vector in the XYZ global coordinate system is written as:

$$\mathbf{u} = u\,\mathbf{e}_X + v\,\mathbf{e}_Y + w\,\mathbf{e}_Z. \tag{46}$$

The displacement in the cross section of a rod is approximated by the function $\mathbf{U}_{(m)}(\xi,\eta)$, in the longitudinal direction it is approximated by the function $\mathbf{h}^{(m)}(\zeta)$. The displacement vector is the product of the two functions:

$$\mathbf{u} = \mathbf{u}(\xi,\eta,\zeta) = \sum_{m=1}^{M} \bar{\mathbf{h}}^{(m)}(\xi,\eta,\zeta) = \sum_{m=1}^{M} \mathbf{U}_{(m)}(\xi,\eta)\,\mathbf{h}^{(m)}(\zeta), \tag{47}$$

where $-1 \le \xi \le 1$, $-1 \le \eta \le 1$, $-1 \le \zeta \le 1$ are the coordinates of the standard hexahedral element.

Depending on the degree of the polynomial functions included in the series expansion, we arrive at a sequence of hierarchical rod models, characterized by polynomials of degree Tm or Lm. At a given level, the longitudinal distribution of the displacement field is determined by the highest power of the polynomial in the definition of $\mathbf{h}^{(m)}(\zeta)$. The maximum of the degree will be denoted by p.

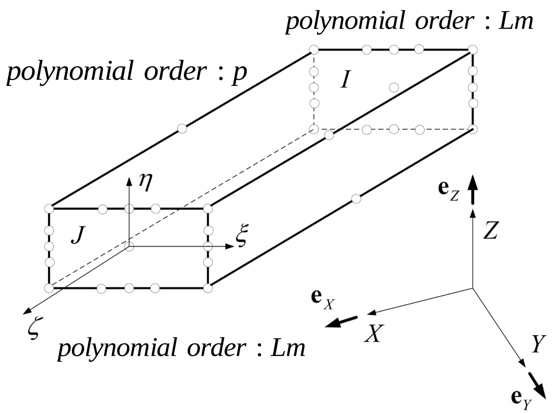

Figure 6. A prismatic rod with a rectangular cross section in the adopted local coordinate system (ξ,η,ζ). I and J are the initial and final cross section labels.

We denote the shape functions containing Lm-order Legendre polynomials [1, 37] describing the director functions by $N_i(\xi,\eta)$, and the longitudinal ones by $\psi^i(\zeta)$. We get

$$u_\tau = \sum_{i=1}^{nLm} N_i(\xi,\eta)\cdot\psi^i_\tau(\zeta), \quad \tau = 1,2,3 \tag{48}$$

which in matrix form is written as

$$u_\tau = \mathbf{N}^\tau(\xi,\eta)\boldsymbol{\psi}_\tau(\zeta), \quad \tau = 1,2,3 \tag{49}$$

where

$$\mathbf{N}^\tau(\xi,\eta) = [N_1(\xi,\eta)\ N_2(\xi,\eta), ..., N_i(\xi,\eta), ..., N_{nLm}(\xi,\eta)]_{(1,nLm)},$$

in which nLm is the number of Legendre polynomials. The $\boldsymbol{\psi}_\tau$ function is approximated as outlined in Figure 7. The displacement of the bodies will be approximated

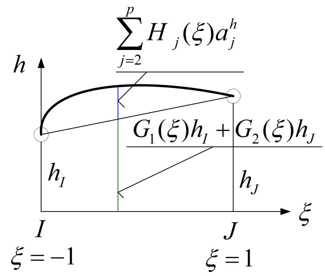

Figure 7. Approximation along the length of the rod for an arbitrary function h

by linear approximation and higher power Legendre functions through the values in the nodes I and J of the element. In concise form:

$$\psi_\tau^i = \psi_\tau^i(\zeta) = \frac{1}{2}(1-\zeta)u_\tau^{i,I} + \frac{1}{2}(1+\zeta)u_\tau^{i,J} + \sum_{j=2}^{p} H_j(\zeta)a_\tau^{i,j}, \quad i=1,...,nLm, \quad \tau=1,2,3 \tag{50a}$$

$$\psi_\tau^i = \psi_\tau^i(\zeta) = \left[\frac{1}{2}(1-\zeta) \ \ \frac{1}{2}(1+\zeta)\right]\left[\begin{array}{c} u_\tau^{i,I} \\ u_\tau^{i,J} \end{array}\right] + \sum_{j=2}^{p} H_j(\zeta)a_\tau^{i,j}, \quad i=1,...,nLm, \quad \tau=1,2,3 \tag{50b}$$

$$\psi_\tau^i = \psi_\tau^i(\zeta) = \tilde{\mathbf{g}}(\zeta)\mathbf{q}_\tau^i + \tilde{\mathbf{h}}(\zeta)\mathbf{a}_\tau^i, \quad i=1,...,nLm, \quad \tau=1,2,3 \tag{50c}$$

It can be seen from the approximation displayed in (50) that one component of the displacement is approximated through $nLm * (p+1)$ parameters. Note that $H_j(\zeta)$ can be obtained from Legendre polynomials $P_j(\zeta)$ using the formula

$$H_j(\zeta) = \frac{1}{\sqrt{2(2j-1)}}(P_j(\zeta) - P_{j-2}(\zeta)),$$

see, for example [1, 37]. In matrix form ($np = p-1$):

$$\begin{aligned}\boldsymbol{\psi}_{\tau(nLm,1)} &= \boldsymbol{\psi}_\tau(\zeta) = \\ &= \tilde{\mathbf{G}}(\zeta)_{(nLm,2\times nLm)}\mathbf{q}_{\tau(2\times nLm,1)} + \tilde{\mathbf{H}}(\zeta)_{(nLm,nLm\times np)}\mathbf{a}_{\tau(nLm\times np,1)}, \quad \tau = 1,2,3\end{aligned} \tag{51}$$

Introducing the following matrix:

$$\underset{(3,3\times nLm)}{\mathbf{N}(\xi,\eta)} = \begin{bmatrix} N_1(\xi,\eta) & 0 & 0 & \dots & N_i(\xi,\eta) & 0 & 0 & \dots \\ 0 & N_1(\xi,\eta) & 0 & \dots & 0 & N_i(\xi,\eta) & 0 & \dots \\ 0 & 0 & N_1(\xi,\eta) & \dots & 0 & 0 & N_i(\xi,\eta) & \dots \end{bmatrix} \quad (52)$$

the displacement vector $\mathbf{u}^T = [u_1\ u_2\ u_3]$ is written in the following form:

$$\mathbf{u} = \mathbf{N}(\xi,\eta)\psi(\zeta). \quad (53)$$

In addition the vector $\boldsymbol{\psi} = \boldsymbol{\psi}(\zeta)$ is:

$$\begin{aligned} &\boldsymbol{\psi}_{(3\times nLm,1)} = \boldsymbol{\psi}(\zeta) = \\ &\quad = \mathbf{G}(\zeta)_{(3\times nLm,6\times nLm)}\mathbf{q}_{(6\times nLm,1)} + \boldsymbol{\Phi}(\zeta)_{(3\times nLm,3\times nLm\times np)}\mathbf{a}_{(3\times nLm\times np,1)} \end{aligned} \quad (54)$$

$$\underset{(1,np)}{\tilde{\mathbf{h}}} = \left[\, H_2(\zeta)\ \ H_3(\zeta)\ \ \dots\ \ H_p(\zeta)\,\right], \qquad \underset{(nLm,nLm\times np)}{\tilde{\mathbf{H}}(\zeta)} = \begin{bmatrix} \tilde{\mathbf{h}}(\zeta) & & \dots & \\ & \tilde{\mathbf{h}}(\zeta) & \dots & \\ \dots & \dots & \dots & \dots \\ & & \dots & \tilde{\mathbf{h}}(\zeta) \end{bmatrix}, \quad (55a)$$

$$\underset{(2\times nLm,1)}{\mathbf{q}_\tau} = \begin{bmatrix} \mathbf{q}^1 \\ \mathbf{q}^2 \\ \dots \\ \mathbf{q}^{nLm} \end{bmatrix}, \qquad \underset{(nLm\times np,1)}{\mathbf{a}_\tau} = \begin{bmatrix} \mathbf{a}^1 \\ \mathbf{a}^2 \\ \dots \\ \mathbf{a}^{nLm} \end{bmatrix}, \quad (55b)$$

$$\underset{(nLm,2\times nLm)}{\tilde{\mathbf{G}}} = \begin{bmatrix} \tilde{G}_{11} & 0 & \cdots & 0 & \tilde{G}_{1,nLm+1} & 0 & \cdots & 0 \\ 0 & \tilde{G}_{22} & \cdots & 0 & 0 & \tilde{G}_{2,nLm+2} & \cdots & 0 \\ \dots & \dots & \dots & \dots & \dots & \dots & \dots & \dots \\ 0 & 0 & \cdots & \tilde{G}_{nLm,nLm} & 0 & 0 & \cdots & \tilde{G}_{nLm,2\times nLm} \end{bmatrix},$$

$$\tilde{G}_{11} = \tilde{G}_{22} = \cdots = \tilde{G}_{nLm,nLm} = \frac{1-\zeta}{2},$$

$$\tilde{G}_{1,nLm+1} = \tilde{G}_{2,nLm+2} = \cdots = \tilde{G}_{nLm,2\times nLm} = \frac{1+\zeta}{2}, \quad (55c)$$

$$\underset{(3\times nLm,6\times nLm)}{\mathbf{G}} =$$

$$\begin{bmatrix} G_{11} & 0 & \cdots & 0 & G_{1,3\times nLm+1} & 0 & \cdots & 0 \\ 0 & \tilde{G}_{22} & \cdots & 0 & 0 & \tilde{G}_{2,3\times nLm+2} & \cdots & 0 \\ \dots & \dots & \dots & \dots & \dots & \dots & \dots & \dots \\ 0 & 0 & \cdots & \tilde{G}_{3\times nLm,3\times nLm} & 0 & 0 & \cdots & \tilde{G}_{3\times nLm,6\times nLm} \end{bmatrix},$$

$$G_{11} = G_{22} = \cdots = G_{3\times nLm,3\times nLm} = \frac{1-\zeta}{2},$$

$$G_{1,3\times nLm+1} = G_{2,3\times nLm+2} = \cdots = G_{3\times nLm,6\times nLm} = \frac{1+\zeta}{2}. \quad (55d)$$

$$\underset{(3\times nLm, 3\times nLm\times np)}{\mathbf{\Phi}(\zeta)} = \begin{bmatrix} H_2 & H_3 & \cdots & H_p & 0 & 0 & \cdots & 0 & \cdots\cdots & 0 & 0 & \cdots & 0 \\ 0 & 0 & \cdots & 0 & H_2 & H_3 & \cdots & H_p & \cdots\cdots & 0 & 0 & \cdots & 0 \\ \cdots & \cdots & \cdots & \cdots & \cdots & \cdots & \cdots & \cdots & \cdots & \cdots & \cdots & \cdots & \cdots \\ 0 & 0 & \cdots & 0 & 0 & 0 & \cdots & 0 & \cdots\cdots & H_2 & H_3 & \cdots & H_p \end{bmatrix}. \tag{55e}$$

The internal coordinates displacement coordinates of the element are approximated via $ND_{hLm}{}^1 = 2\times nLm + nLm \times (p-1) = nLm(p+1)$ parameters. So, the vector $\mathbf{q}_{(6\times nLm,1)}$ contains the coefficients of hLm polynomials interpreted on the I and J planes, while the vector $\mathbf{a}_{(3\times nLm\times np,1)}$ contains the coefficients $a_\tau^{i,j}$ that multiply the polynomials $H_j(\zeta)$, i.e.

$$\underset{(1,6\times nLm)}{\mathbf{q}^T} = \Big[u_1^{1,I}\ u_2^{1,I}\ u_3^{1,I}\ u_1^{2,I}\ u_2^{2,I}\ u_3^{2,I}\ \ldots\ u_1^{nLm,I}\ u_2^{nLm,I}\ u_3^{nLm,I}$$
$$u_1^{1,J}\ u_2^{1,J}\ u_3^{1,J}\ u_1^{2,J}\ u_2^{2,J}\ u_3^{2,J}\ \ldots\ u_1^{nLm,J}\ u_2^{nLm,J}\ u_3^{nLm,J}\Big] \tag{56}$$

$$\underset{(1,3\times nLm\times np)}{\mathbf{a}^T} = \Big[a_1^{1,2}\ \ldots\ a_1^{1,p} a_2^{1,2}\ \ldots\ a_2^{1,p}\ a_3^{1,2} \ldots\ a_3^{1,p}\ \ldots$$
$$a_1^{nLm,2}\ \ldots\ a_1^{nLm,p}\ a_2^{nLm,2}\ \ldots\ a_2^{nLm,p}\ a_3^{nLm,2}\ \ldots\ a_3^{nLm,p}\Big] \tag{57}$$

Using the notation $u = u_1$, $v = u_2$ $w = u_3$ the components of the strain tensor are calculated as follows:

$$\begin{gathered} \varepsilon_X = \frac{\partial u}{\partial X}, \quad \varepsilon_Y = \frac{\partial v}{\partial Y}, \quad \varepsilon_Z = \frac{\partial w}{\partial Z}, \\ \gamma_{XY} = \frac{\partial u}{\partial Y} + \frac{\partial v}{\partial X}, \quad \gamma_{YZ} = \frac{\partial v}{\partial Z} + \frac{\partial W}{\partial Y}, \quad \gamma_{ZX} = \frac{\partial w}{\partial X} + \frac{\partial u}{\partial Z}. \end{gathered} \tag{58}$$

Since the displacement field is approximated in the local system ξ, η, ζ, it will be necessary to calculate the derivative of the displacement u in the global system:

$$\partial_G \mathbf{u} = \begin{bmatrix} \frac{\partial u}{\partial X} \\ \frac{\partial u}{\partial Y} \\ \frac{\partial u}{\partial Z} \end{bmatrix} = \mathbf{J}^{-1} \begin{bmatrix} \frac{\partial u}{\partial \xi} \\ \frac{\partial u}{\partial \eta} \\ \frac{\partial u}{\partial \zeta} \end{bmatrix} = \mathbf{J}^{-1}\partial_L \mathbf{u}\,,$$

where $\mathbf{J}^{-1}$ is the inverse of Jacobian matrix $\mathbf{J}$:

$$\mathbf{J} = \begin{bmatrix} \frac{\partial X}{\partial \xi} & \frac{\partial Y}{\partial \xi} & \frac{\partial Z}{\partial \xi} \\ \frac{\partial X}{\partial \eta} & \frac{\partial Y}{\partial \eta} & \frac{\partial Z}{\partial \eta} \\ \frac{\partial X}{\partial \zeta} & \frac{\partial Y}{\partial \zeta} & \frac{\partial Z}{\partial \zeta} \end{bmatrix}. \tag{59}$$

We remark that $\mathbf{J}$ is calculated from the mapping functions. For later consideration we shall introduce the following notations:

$$\partial_\xi N(\xi,\eta) = N_{,\xi}(\xi,\eta), \quad \partial_\eta N(\xi,\eta) = N_{,\eta}(\xi,\eta), \quad \partial_\zeta \tilde{G}(\zeta) = \tilde{G}_{,\zeta}(\zeta), \quad \partial_\zeta \tilde{H}(\zeta) = \tilde{H}_{,\zeta}(\zeta) \tag{60}$$

The derivatives of the displacement fields in the local system are:

$$\begin{aligned}
u_{,\xi} &= \frac{\partial u}{\partial \xi} = \mathbf{N}_{,\xi}(\xi,\eta)(\tilde{\mathbf{G}}(\zeta)\mathbf{q}^u + \tilde{\mathbf{H}}(\zeta)\mathbf{a}^u), \quad u = u_1 \leftrightarrow v = u_2 \leftrightarrow w = u_3 \\
u_{,\eta} &= \frac{\partial u}{\partial \eta} = \mathbf{N}_{,\eta}(\xi,\eta)(\tilde{\mathbf{G}}(\zeta)\mathbf{q}^u + \tilde{\mathbf{H}}(\zeta)\mathbf{a}^u), \quad u = u_1 \leftrightarrow v = u_2 \leftrightarrow w = u_3 \\
u_{,\zeta} &= \frac{\partial u}{\partial \zeta} = \mathbf{N}(\xi,\eta)(\tilde{\mathbf{G}}_{,\zeta}(\zeta)\mathbf{q}^u + \tilde{\mathbf{H}}_{,\zeta}(\zeta)\mathbf{a}^u), \quad u = u_1 \leftrightarrow v = u_2 \leftrightarrow w = u_3
\end{aligned} \tag{61}$$

Based on (58), the derivatives of the displacement components are computed in the global coordinate system from which the $3D$ strain tensor and, through application of Hooke's law, the stress tensor are computed.

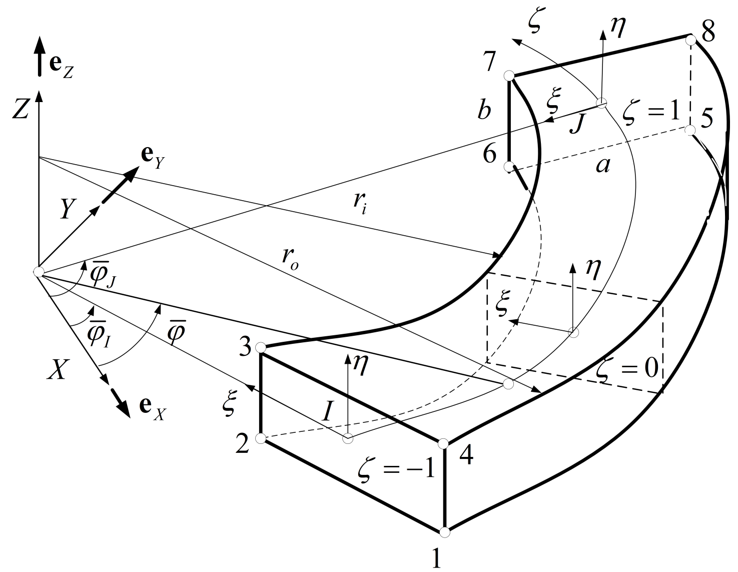

Figure 8. Relationship betweern the local coordinates ξ, η, ζ and the global ones

The mapping for a curved element is illustrated in Figure 8 where the blending technique was used to produce a smooth mapping function [1, 37].

Note that $\bar{\varphi}_m = (\bar{\varphi}_I + \bar{\varphi}_J)/2, \quad \bar{\varphi}_d = (\bar{\varphi}_J - \bar{\varphi}_I)/2, \quad \bar{\varphi} = \bar{\varphi}_m + \zeta\bar{\varphi}_d$.

It is worth comparing the number of unknowns associated with the $3D$ p-version with the hierarchical element: Using the trunk space described [1, 37], each field is approximated with $ND_{3D}{}^1$ unknowns whereas there are $ND_{hLm}{}^1$ unknowns in the hierarchic formulation.

The three displacement fields are approximated using $ND_{hLm} = 3 \times nLm \times 2 + 3 \times nLm \times (p-1) = 3 \times nLm \times (p+1)$ degrees of freedom per element. Of these, $3 \times nLm \times 2$ belong to the boundary points (nodes I and J), the rest are internal functions. For $3D$ elements (hexahedral element), the number of unknowns used to describe one or three fields is ${ND_{3D}}^1$ or ${ND_{3D}}^3$, i.e.,

	$p=2$	3	4	5	6
${ND_{3D}}^1$	20	35	54	79	111
${ND_{3D}}^3$	60	105	162	237	333

For the planar trunk space, the number of unknowns is:

	$p=2$	3	4	5	6	7	8
${ND_{2D}}^1$	8	12	17	23	30	38	47
${ND_{2D}}^2$	16	24	34	46	50	76	94

These relationships also hold when Tm polynomials rather than Lm polynomials are used.

The director functions for the hTm elements are the polynomials constructed by substituting $x \to \xi$, $y \to \eta$ for the monomials of the Pascal triangle (see Appendix A) for the hm element, where $-1 \leq \xi \leq 1$, $-1 \leq \eta \leq 1$, i.e. $hm \to hTm$.

Since three-dimensional displacements are approximated by both the hTm and hLm elements, the total number of unknowns is ${ND_{hTm}}^1$ and ND_{hTm}, respectively.

hTm beam element with Taylor expansion

	ht2	ht3	ht4	ht5	ht6	ht7	ht8
${ND_{hTm}}^1$	6(p+1)	10(p+1)	15(p+1)	21(p+1)	28(p+1)	36(p+1)	45(p+1)
ND_{hTm}	18(p+1)	30(p+1)	45(p+1)	63(p+1)	84(p+1)	108(p+1)	134(p+1)

hLm beam element with $2D$ Legendre function

	hL2	hL3	hL4	hL5	hL6	hL7	hL8
${ND_{hLm}}^1$	8(p+1)	12(p+1)	17(p+1)	23(p+1)	30(p+1)	38(p+1)	47(p+1)
ND_{hLm}	24(p+1)	36(p+1)	51(p+1)	69(p+1)	90(p+1)	114(p+1)	141(p+1)

For hTm elements, we use polynomials defined by

$$H_{j+1}(\zeta) = [0.5(1+\zeta)]^{j+1} - 0.5(1+\zeta),\ j = 1, 2, ...$$

It is seen that for the $3D$ approximation at $p = 6$, the degree of freedom of the element is 333, while for the hierarchical element hTm ($hT6$) it is 588, and for the hierarchical element hLm ($hL6$) it is 630. Here we assumed that the polynomial degree assigned to the longitudinal approximation is 6.

Note: Given that the displacement field of the i-th element is approximated in the form $\mathbf{u}^{(i)} = \mathbf{N}^{(i)}(\xi, \eta)\psi^{(i)}(\zeta)$, the $\mathbf{N}^{(i)}(\xi, \eta)$ and $\mathbf{N}^{(i)}(\xi, \eta = \pm 1)$ matrices must be used instead of the $\mathbf{U}^{(3)}(x, y)\mathbf{R}^{(3)}_{red}$ and $\tilde{\mathbf{U}}^{(i)}(x, y_b^{(i)})$ matrices when a Winkler-type foundation is used or the contact problem described previously has to be solved.

4. Numerical examples

4.1. **Prismatic beam.** Let the geometric dimensions of a prismatic beam be $a = 40$, $b = 20$, $L = 157.0796$ mm ($200\pi/4 = 50\pi$), and the material constants be: Elastic modulus $E = 2 \cdot 10^5$ MPa, Poisson's ratio $\nu = 0.3$. The beam is shown in Figure 9.

In the following we present results for two load cases. In the first load case, at the end of the rod, on the $Z = 0$ boundary, a parabolic distributed load acts in the direction y which has the resultant $F_Y = 200$ N. In the second load case a distributed load with an intensity of $p_y = -p_Y = 0.25\mathrm{N/mm}^2$ acts on the $y = -b/2$ surface in the direction y.

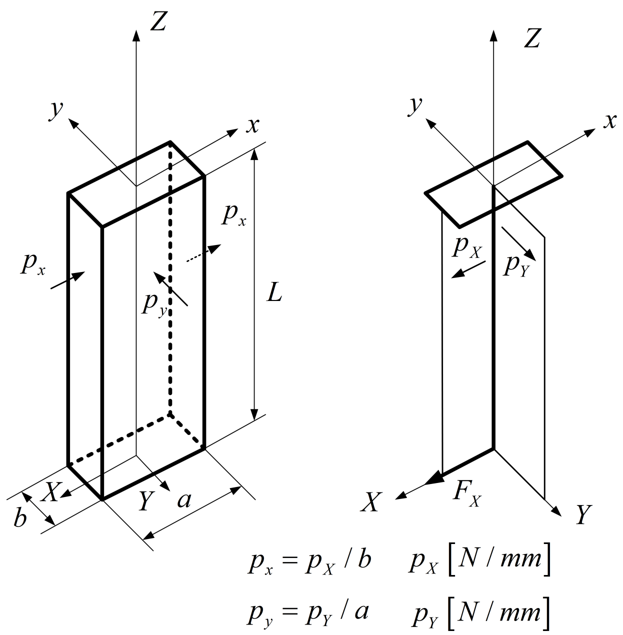

Figure 9. The geometry of a cantilever prismatic beam, the global XYZ and the local coordinate system xys ($s = Z$). The beam is fixed in the $Z = L$ plane

Solving a sequence hierarchical models, we get the results for degrees $p = 2, ..., 6$ in terms of the Y-component of the displacement of the centroid of the cross section $Z = 0$ shown in Figure 10. The results of the $3D$ finite element model (obtained by the StressCheck program) are also shown. It is clear that as the hierarchic level increases, displacement converges to the $3D$ result. The results for a sequence of hLm models are shown in Figure 11. The differences between the hierarchic models and the $3D$ finite element solution are model form errors within the family of models formulated under the assumptions of the linear theory of elasticity.

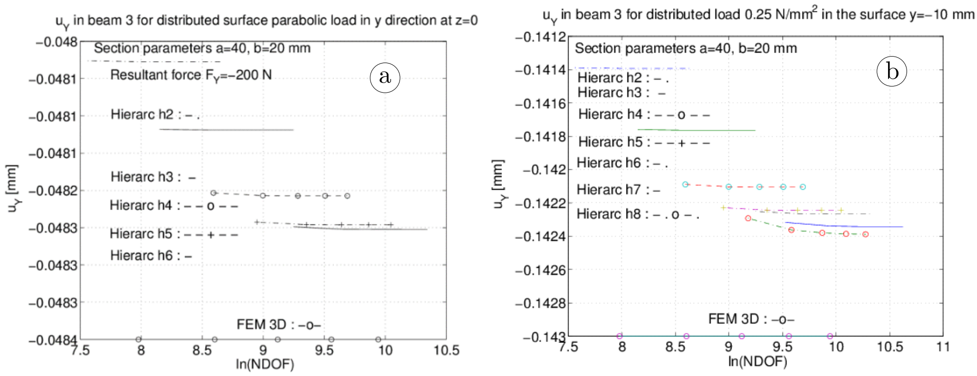

Figure 10. Convergence diagrams for hm models: a) the parabolic distributed load on the end plate acts (1st load), resulting in $F_Y = -200$ N, b) $p_y = -p_Y = 0.25\,\mathrm{N/mm}^2$ load is distributed on the $y = -b/2$ surface (2nd load)

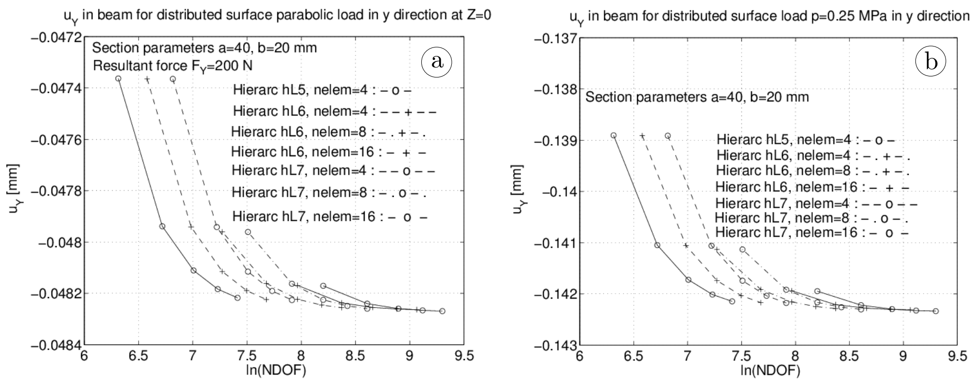

Figure 11. Convergence diagrams for hLm models, a) 1st load case, the displacement of the point $x = y = 0$ of the end plate in the Y direction in the case of different hierarchical models, b) 2nd load case

It is seen that in the case of load 2 the displacement values agree to 4 decimal digits when 16 elements and the $hL6$ and $hL7$ models are used. The numerical values are: $hL6$ - 0.482632D-01, $hL7$ - 0.482690D-01 mm for load case 1; $hL6$ - 0.142313D+00, $hL7$ - 0.142336D+00 mm for load case 2.

Solving the same problem using the Abaqus software, we get:

Mesh 1: $10 \times 10 \times 9.862$ hexahedral elements (C3D20R), 20 nodes, quadratic, reduced integration, the number of nodes is 869 (2496 degrees of freedom, lnNDOF=7.82) Mesh 2: $2 \times 2 \times 1.987$ hexahedral elements (C3D20R), 20 nodes, quadratic, reduced integration, thus the total node number: 71129 (212726 unknown, lnNDOF=12.27)

- Load case 1 for Mesh 1 -0.0541153 [mm]; for Mesh 2 -0.0485062 [mm]
- Load case 2 for Mesh 1 -0.1416740 [mm]; for Mesh 2 -0.142314 [mm].

On comparing the results with those obtained by StressCheck (load case 1 -0.0484 mm, load case 2 -0.143 mm), a much lower rate of convergence is observed.

Furthermore, we note that reduced integration introduces a type error that cannot be treated by mesh refinement. Reduced integration is one of the *variational crimes* [52].

The distributions of the stress σ_2 for the models $h3$ and $h6$ are shown for load case 2 in Figure 12. Here $p_y = 0.25$ MPa acts as a compressive stress on the surface $y = -b/2$.

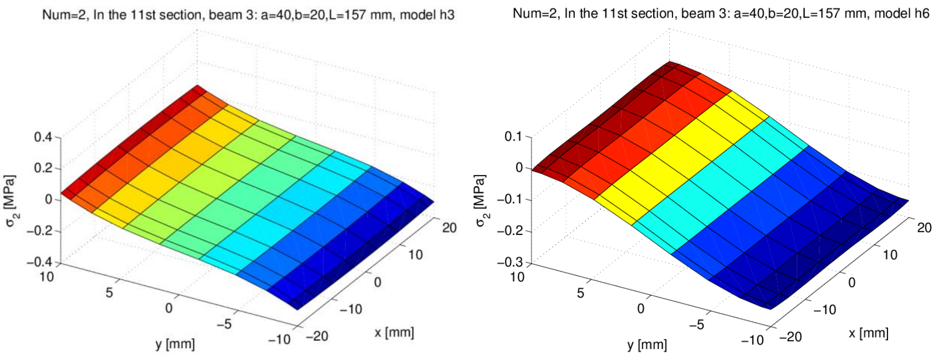

Figure 12. σ_2 stress distributions in load case 2 (models $h3$, $h6$)

We observe that the weak boundary conditions are well approximated by the $h6$ model: σ_2 is zero at the $y = 10$ mm boundary and it is $= -0.25$ MPa at the $y = -10$ mm boundary. This is not the case for lower order models such as model $h3$.

4.2. **Curved beam.** Next we consider the curved beam shown in Figure 13. The geometric parameters are: $R_0 = 100$ mm, $a = 40$ mm, $b = 20$ mm. The material is assumed to be linearly elastic, homogeneous and isotropic, the modulus of elasticity is $E = 2.0 \cdot 10^5$ MPa, Poisson's ratio is 0.3.

We examine the behavior of the structure under two load cases: In load case 1, parabolic distributed traction is applied on the cross section $\bar{\varphi} = \pi$ in the Z direction, the resultant of which is $F_z = 200$ N. In load case 2 distributed normal traction is exerted on the surface $y = -b/2$ in the Z direction, the magnitude of which is $p_y = 0.25$ MPa.

*Application of hm type elements.*The convergence diagrams obtained for two load cases are shown in Figures 14-15. The results of the $3D$ solution obtained with the StressCheck finite element program [35] are also shown. The diagrams clearly show the rapid convergence of the quantities of interest computed from the numerical solutions. The relative errors defined by

$$error = \frac{|\mathbf{u}_{FEM}| - |\mathbf{u}_{hierarc}|}{|\mathbf{u}_{FEM}|} 100\% \tag{62}$$

are below 4% for both load cases in the $h6$, $h7$ models, whereas the relative error is over 17% at the initial low hierarchical level.

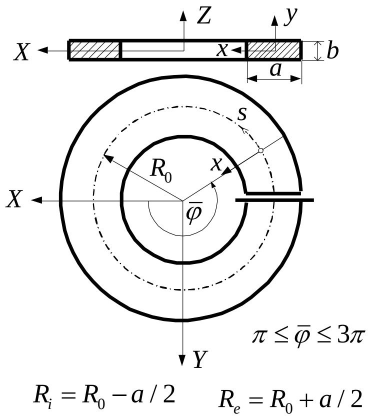

Figure 13. Geometry of the curved rod, the global XYZ coordinate system and the local xys coordinate system. The beam is fixed in the plane $\bar{\varphi} = 3\pi$

Load case 1

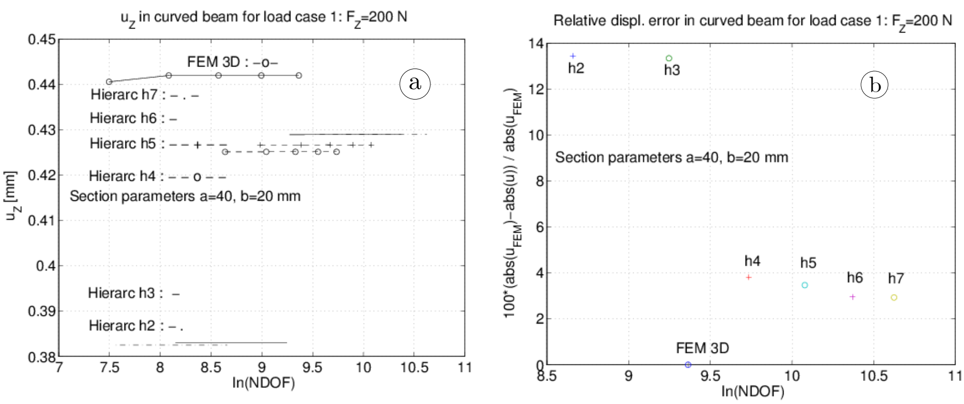

Figure 14. Convergence diagrams for hm elements for load case 1 ($F_z = 200$ N), a) displacement values, b) relative errors in displacements

Load case 2

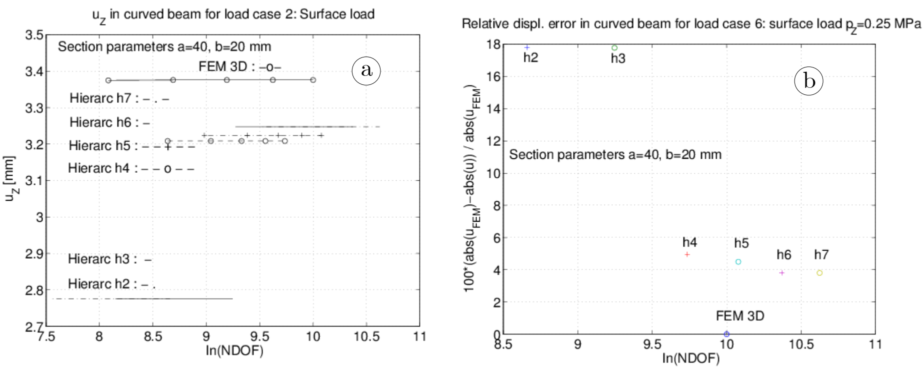

Figure 15. Convergence diagrams for hm elements in load case 2: a) displacements, b) relative errors in displacements

Application of hLm type elements. In this section we demonstrate that much faster convergence can be obtained with hLm type elements. Polynomial approximations $p = 3, 4, 5, 6$ were used in the longitudinal direction.

Load case 1:

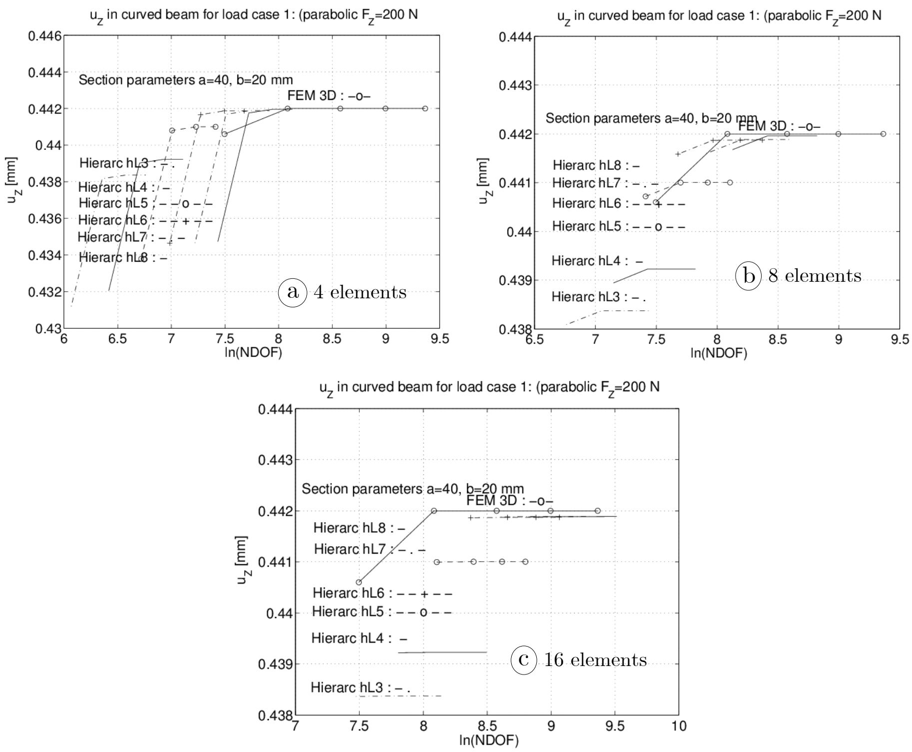

Figure 16. Convergence diagrams for hLm elements: at $F_z = 200$ N

Load case 2:

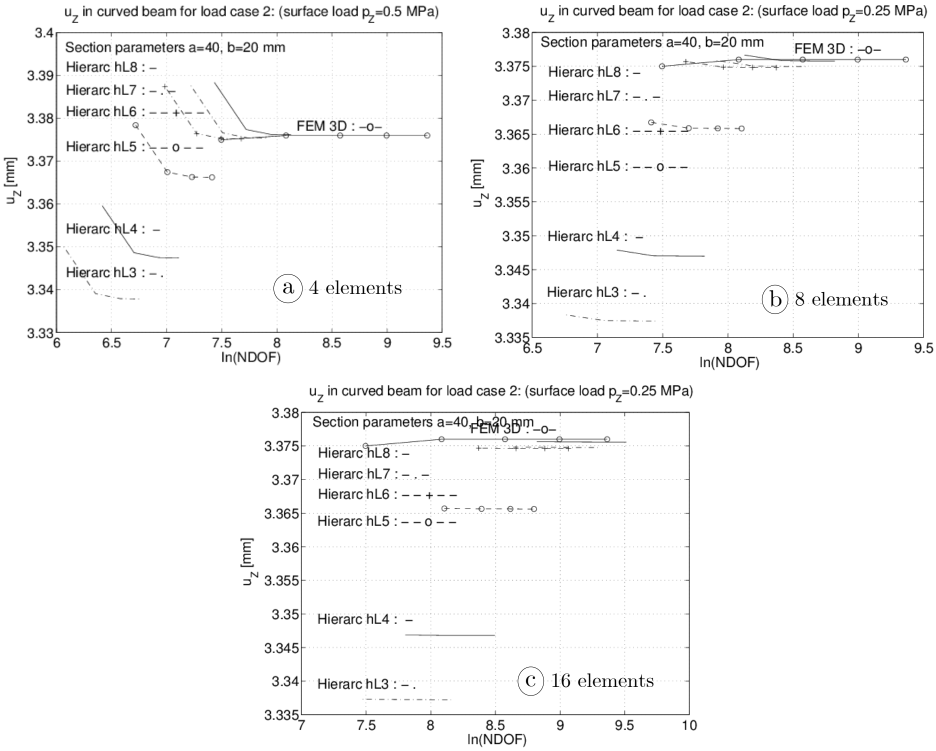

Figure 17. Convergence diagrams for load case 2

The relative errors do not exceed 1.2% when 8 elements and $p = 6 - 8$ are used.

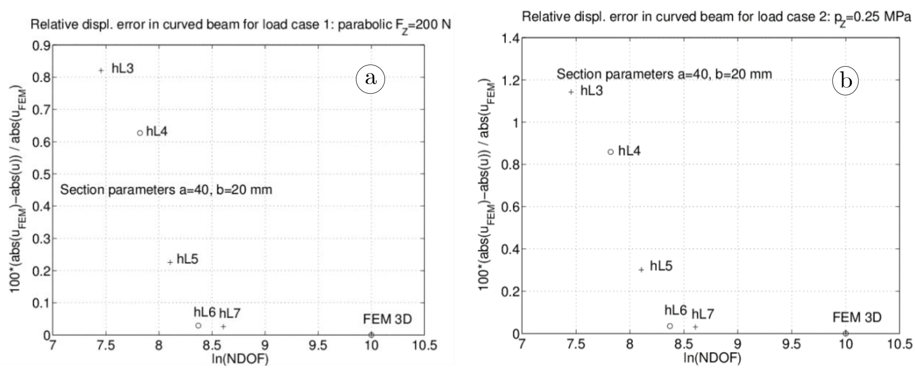

Figure 18. Relative errors for 8 elements, $p = 8$, a) in load case 1, b) in load case 2

Application of hTm elements. The relative errors in terms of the maximum displacement are shown for load cases 1 and 2 in Figure 19. Four hTm elements were used.

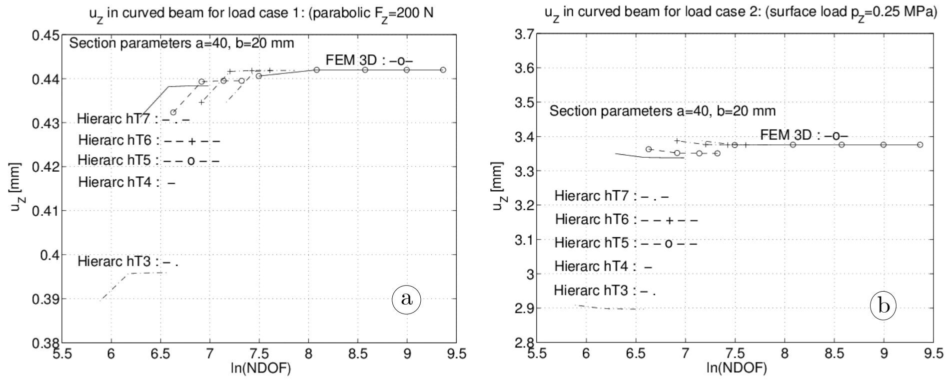

Figure 19. Convergence diagrams for load cases 1 and 2 using four htm elements

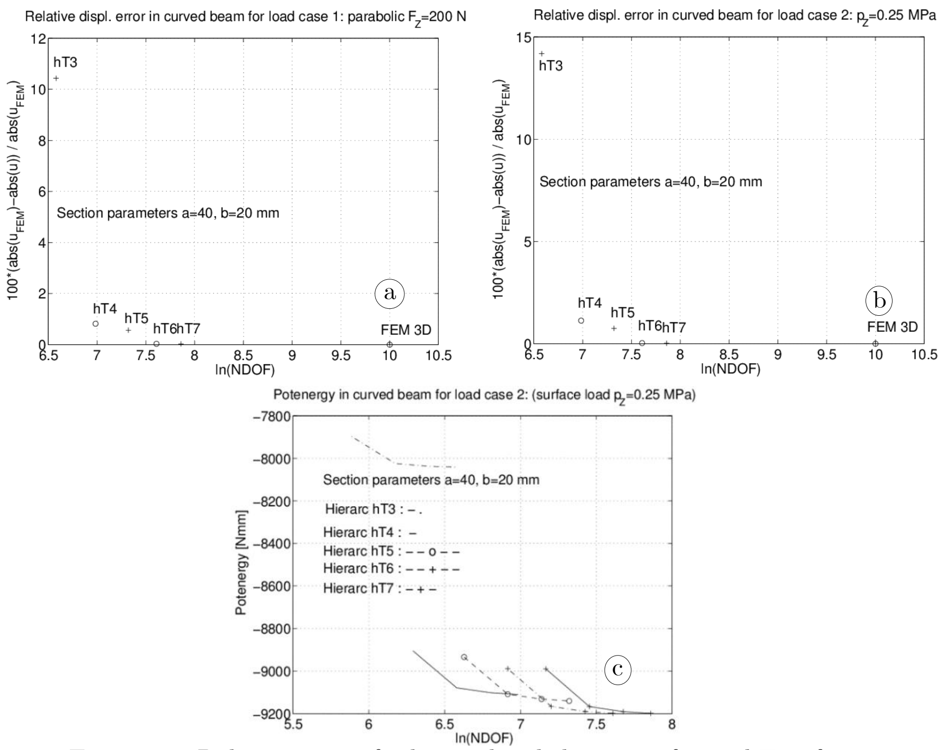

Figure 20. Relative errors for hierarchical elements of type hTm, four elements, a) load case 1, b) load case 2, c) potential energy for load case 2

Figure 20 shows the relative errors. Figure 20c shows the convergence of in potential energy. It is clearly visible that the potential energy decreases as p increases, and the smallest value was obtained by the $hT7$ model.

The hTm solution is more accurate than our original hm model. Comparing the results obtained with the hTm and hLm approximations, we can see that the hLm hierarchical approximation gives the more accurate result. This is because if the maximum degree in Taylor expansion is q, then the trunk space will have two more terms. The sum of the powers of the polynomial product terms is $q + 1$. It can be seen that the results for the excessively low $hT3$, $hL3$ hierarchical level are far from the exact solution.

4.3. **Numerical example for the contact problem of prismatic beams.** Let us consider two flexible, prismatic cantilever beams as shown in Figure 21. The geometric dimensions are: $a = b = 15$ mm. $l = 66.66$ mm. The possible contact domain is: $X \in (200, 300)$. The elastic constants are: $E^1 = 200$ GPa, $E^2 = 50$ GPa, or 20 GPa, Poisson's ratio $\nu = 0.3$. The applied load is $F_0 = 1$ kN.

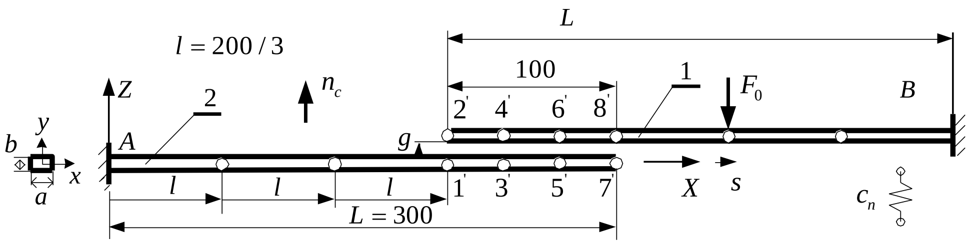

Figure 21. Contact problem of two prismatic beams. There are 12 elements. The points indicated by the open circles represent nodal points

The calculations are performed with the $h5$ hierarchical rod model.

The contact conditions are checked in the Lobatto points, see, for example, [1, 37]. The penalty parameter was set to $c_n = 1000E^1$. Moving along the X axis from right to left, we reach the point where we first find a negative d value.

At this value of X, we assume contact along the x axis in the transverse direction. We will then select this point as the penultimate integration point of the element, which we can use to determine the right-hand side, e.g. the position of the 6th node. With repeated calculations, we move the edge of the element until we reach the position in Figure 22.

Thus, there is contact on the entire surface of this element, and the one to the right already has a gap [38, 39]. Figures 22-26 show some results for this. In the case of $E^2 = 50$ GPa, nodes $3'-4'$ were moved, while in the case of $E^2 = 20$ GPa , nodes $3'-4'$ and $5'-6'$ were moved. With the 12 element mesh, $p = 6$, the number of unknowns is $NDOF = 4464$. The contact element boundaries were established in 10–20 iterations.

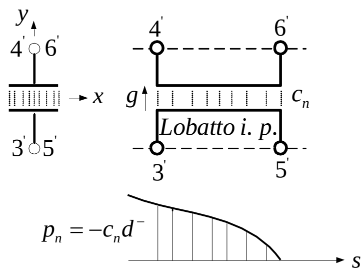

Figure 22. Contact element

Comparing the results with those calculated by the Abaqus [36] and StressCheck [35] 3D finite element programs, looking at the deflection diagrams (Figures 23, 24 and 25), we obtained very close approximations. The deformed configuration obtained with StressCheck can be seen in Figure 23b. We note that the 3D solution with $p = 6$, product space [1, 37], the number of unknowns exceeded the number of unknowns in our $h5$ hierarchical beam model by the factor of nearly 7.

The edge of the contact range and the maximum bending stress in beam 1 are as follows:

$$g = 0, \qquad X_c = 221.71 \text{ mm}, \quad \sigma^{(1)}_{\max} = 117.15 \text{ MPa},$$
$$g = 0.5, \quad X_c = 207.47 \text{ mm}, \quad \sigma^{(1)}_{\max} = 124.40 \text{ MPa}.$$

The distribution of the contact pressure as a function of s is shown in Figure 26. It is clearly visible that the solution satisfies the constraint condition $p_n d = 0$.

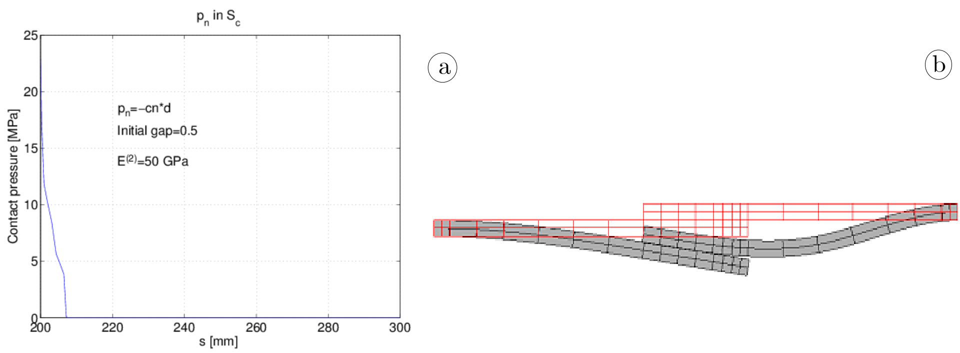

Figure 23. The modulus of elasticity of beam 2 is $E^2 = 50$ GPa, a) Contact pressure with initial gap of 0.5 mm, b) deflection obtained with the StressCheck program with zero initial gap. The number of unknowns (NDOF) is 31,104

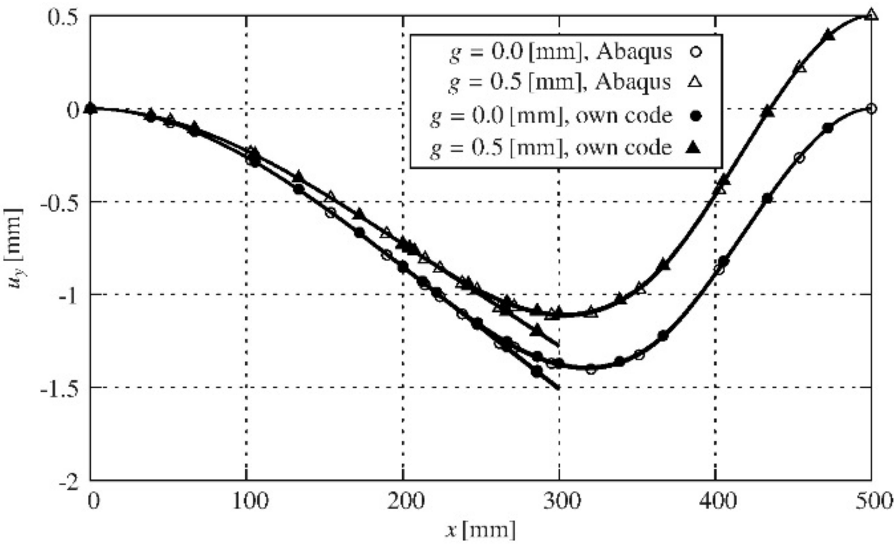

Figure 24. Deflection of the beams

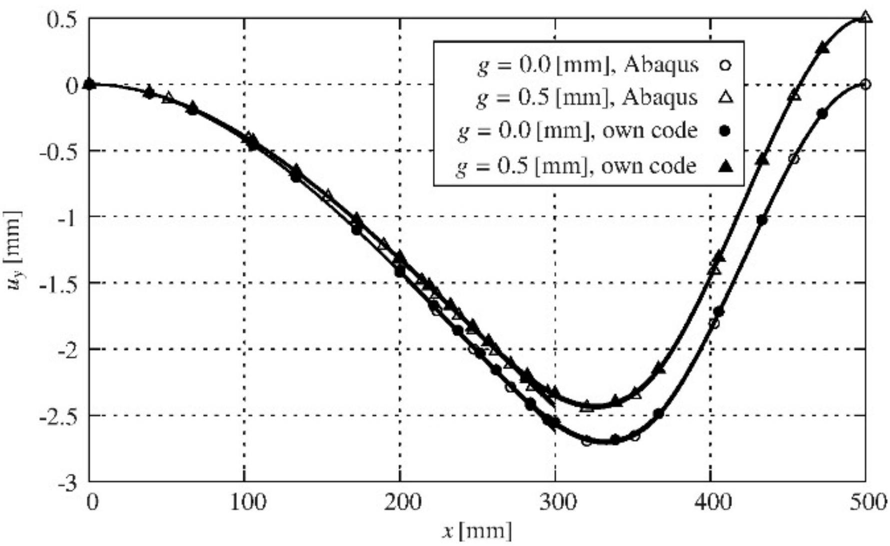

Figure 25. Deflection of the beams for beam 2 with a lower elasticity modulus ($E^2 = 20$ GPa)

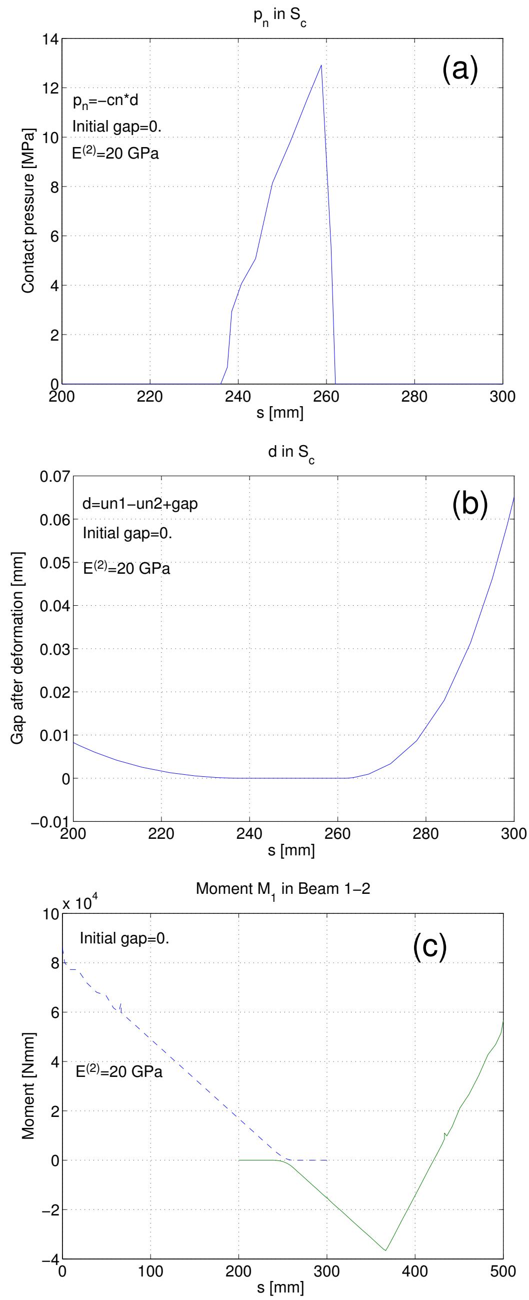

Figure 26. Modulus of elasticity of beam 2: 20.0 GPa, no initial gap: a) the contact pressure, b) the gap d after deformation, c) the resulting bending moment

The edges of the contact range and the maximum bending stress in beam 1:

$$g = 0,\ X_c = 237.52 - 262.05 \text{ mm},\ \sigma^{(1)}_{\max} = 100.71 \text{ MPa},$$
$$g = 0.5,\ \ X_c = 232.69 - 257.29 \text{ mm } \sigma^{(1)}_{\max} = 104.85 \text{ MPa}.$$

4.4. **Numerical example: Curved beam contact problem.** We examine the curved beam shown in Figure 13. The beam is resting on a Winkler-type elastic foundation on the surface $y = b/2$. A parabolic distributed force $F_z = 800$ N is acting on the face $\bar{\varphi} = \pi$. The geometric parameters are $R_0 = 100$ mm, $a = 40$ mm, $b = 20$ mm. The material constants are $E = 200$ GPa, $\nu = 0.3$. The Winkler constant is $c_n = 50\,\mathrm{N/mm}^2$. The beam is fixed at $\bar{\varphi} = 3\pi$. The calculations are performed using the hierarchic model $h6$, that is, the polynomial degree of the field functions is 6.

The displacement component in the Z direction on the circular curve $x = 0$, $y = -b/2$, i.e., the curve on the surface on which the Winkler boundary condition is prescribed, is shown in Figure 27. The displacement curve obtained for the Winkler support is displayed in Figure 27a. Observe that tensile stresses occur. The maximum vertical displacement estimated by our method was 0.0154 mm whereas Abaqus estimated it at 0.01616 mm, while the StressCheck estimation is 0.0164 mm. The error in our approximation, compared with StressCheck, is approximately 6%.

Assuming one-sided frictionless contact between the elastic body and the foundation, i.e. permitting compressive stresses only, the solution is shown in Figure 27b. The first element is in contact, then a gap occurs and at the end there are four elements on which contact occurs again.

The vertical displacement of the $y = b/2$ surface, corresponding to the the $h6$ model with 6 elements (NDOF=7996), is shown in Figure 28. The convergence of the displacement of the point $x = 0$, $y = b/2$, $s = 0$ on the loaded surface and the convergence curve including the maximum occurring at $x = -a/2$, $y = b/2$, $s = 0$ of the loaded surface is shown in Table 1.

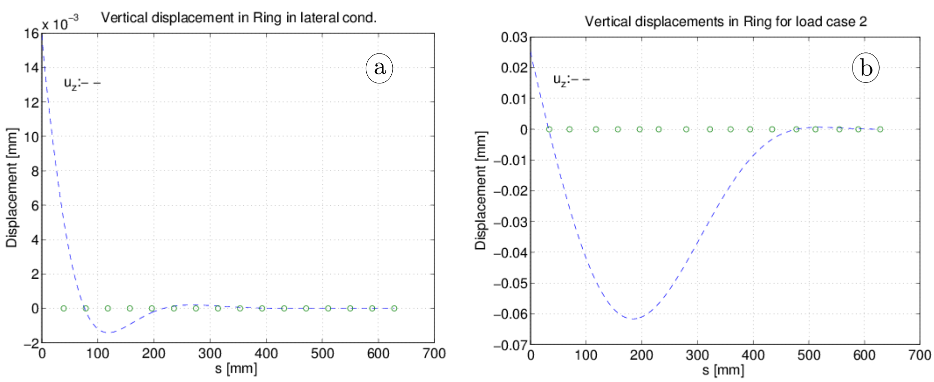

Figure 27. Displacement of the center line $x = 0$, $y = b/2$: a) Winkler support, b) contact condition

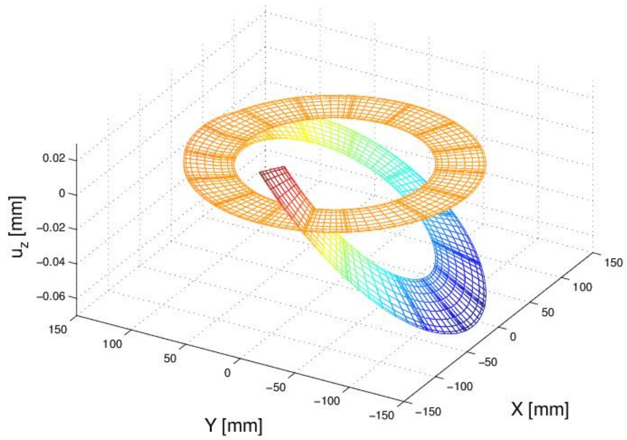

Figure 28. Vertical displacement of the surface $y = b/2$. The displacement of the point $x = 0$, $y = b/2$, $s = 0$ is equal to $\max u_z = 25.76$ μmm

Strong convergence is evident. Figure 29 shows the change in the value of the angle $\bar{\varphi}$, which marks the boundary of the first element. It can be seen that after 10 iterations we have already obtained the solution of the contact problem with negligibly small error.

Solving the problem with 3D finite element programs (Abaqus, StressCheck), we find that, considering Figures 30 and 31, the $\max u_z$ is in the point ($x = -a/2$, $y = b/2$, $s = 0$), that is $\max u_z = 29.88$ μmm obtained with Abaqus and the $\max u_z = 27.9$ μmm ($\max \sigma_z = 1.396$ MPa, $c_n = 50$ n/mm^3) obtained with StressCheck with $\max u_z = 29.61$ μmm; we used the $h6$. The calculated error is Error$= 100(29.61 - 27.9)/27.9 = 6.1\%$, which is a reasonable value considering the significantly smaller number of unknowns in model $h6$. It should be mentioned that the Abaqus program is based on the h-version whereas StressCheck program is based on the p-version. The latter provides faster convergence and a sequence of solutions from which the limit value of the quantities of interest can be estimated. This is an essential requirement of solution verification.

Table 1. Demonstration of the convergence of the p-version method

p	NDF	u_z [mm] ($x = 0$, $y = b/2$, $s = 0$)	$\max u_z$ [mm] ($x = -a/2$, $y = b/2$, $s = 0$)
2	2863	0.0256558	0.02955
3	4012	0.0257587	0.02964
4	5339	0.0257623	0.02963
5	6668	0.0257666	0.02962
6	7996	0.0257685	0.02961

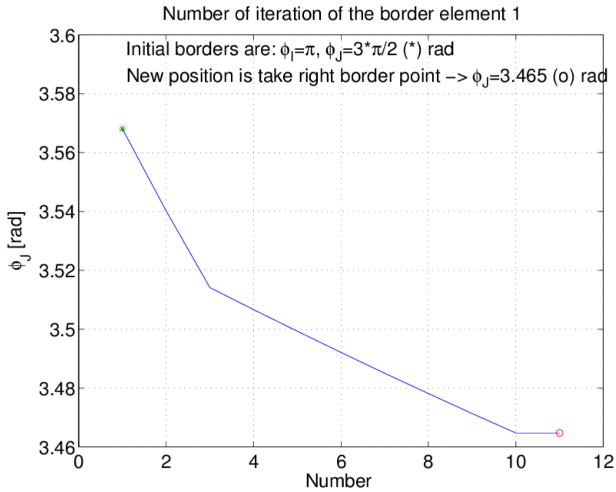

Figure 29. Location of the boundary of the first element as a function of the iteration number when the positioning technique is used

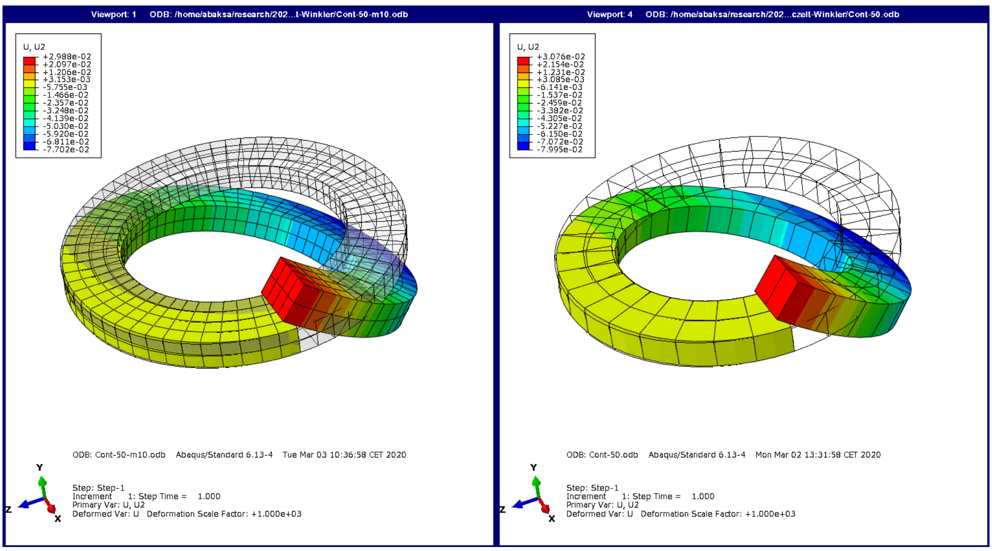

Figure 30. Solutions obtained by the Abaqus program for different numbers of elements using quadratic finite elements C3D20R (NDOF= 20343, NDOF= 6174)

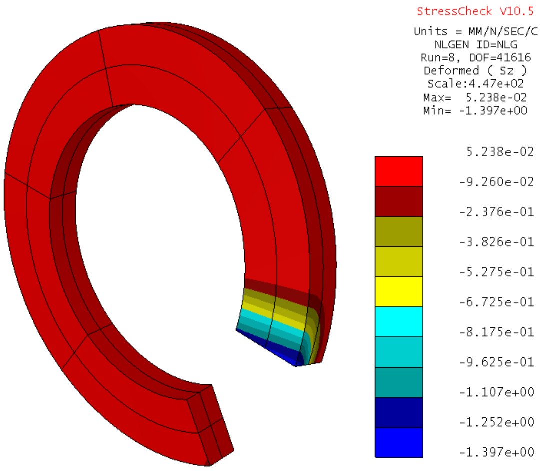

Figure 31. The distribution of σ_z obtained by the StressCheck p-version finite element program, (NDOF=41616)

4.5. **The second numerical example for the contact problem of prismatic beams.** We examine the intersecting prismatic beams shown in Figure 32. Curved surfaces, characterized by a parabolic function, is formed on the $y = \pm b/2$ surfaces of the beams. The extent of this is characterized by the c_z amplitude value.

The elastic material parameters are Young modulus: $E = 200$ GPa, and Poisson's ratio $\nu = 0.3$. The dimensions and location coordinates of the beams result in symmetrical contact when the loads have the appropriate symmetry.

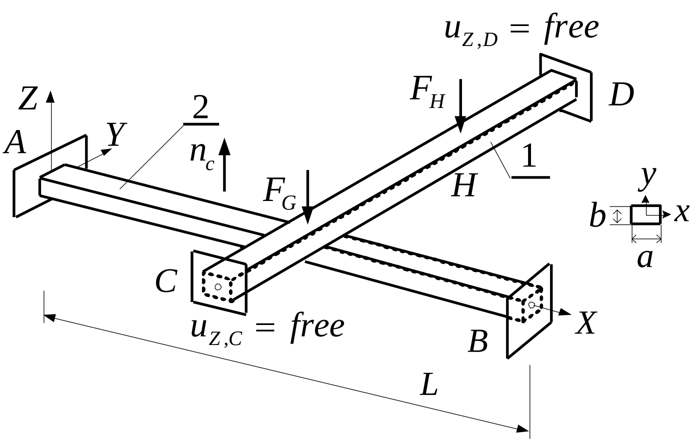

Figure 32. Configuration 2

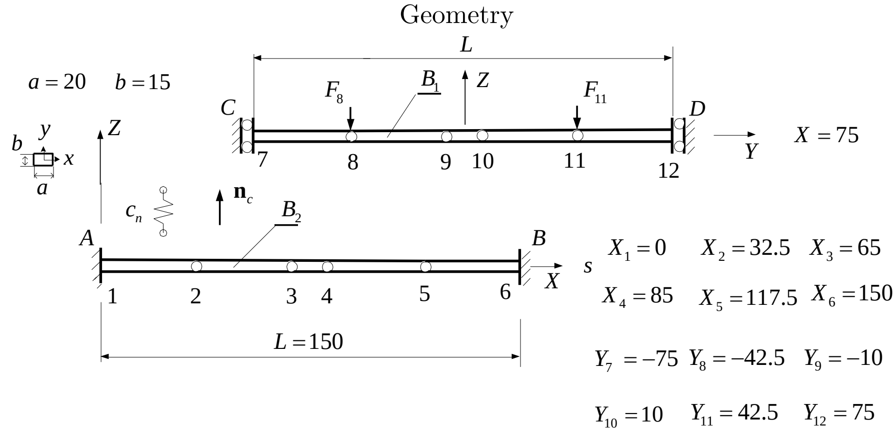

Figure 33. The dimensions of Configuration 2

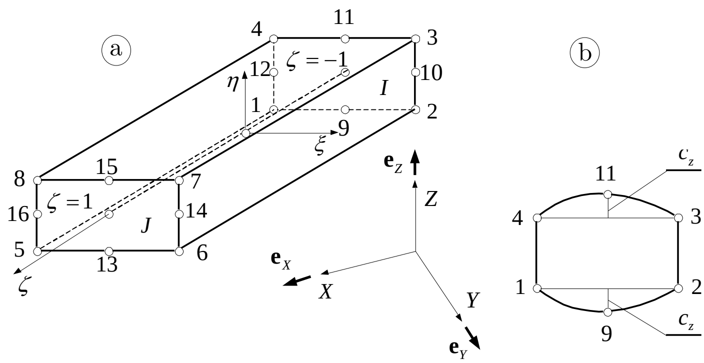

Figure 34. Finite element for mapping a) local system $-1 \leq \xi,\ \eta, \zeta \leq 1$, b) second order's boundary is characterized by parameter c_z

Load case 1:
We assign the values $F_8 = F_{11} = -F_0 = -10$ kN (in the $-Z$ direction) and fix the boundary A and B.

The $hT6$ hierarchical model and 16-node elements, shown in Figure 34, were used, however the locations of the mid-side nodes 9, 11, 13, 15 were assigned values to obtain curved surfaces. The assignment of nodes 9 and 11 is indicated in Figure 34. The assignment of nodes 13 and 15 was analogous. The penalty parameter was assigned the value $c_n = 100000$.

Using 5 elements per bar, taking into account the boundary conditions, the total number of unknowns was 4874. The forces F_8 F_{11} act as concentrated forces, since the first term of the director function in the $hT6$ model is 1. This means that the force acts in the centroid of the cross section. The initial gap is provided by the difference between the Z coordinates of the contact surfaces of bodies B_1 and B_2: $g = Z(B_1, y = -b/2) - Z(B_2, y = b/2)$. We calculate this from the finite element solution. The function obtained at $c_z = 0.1$ is a quadratic function. (See e.g. Figure 36a.)

The estimated contact pressure is shown in Figure 35. The initial gap, the displacement of the beams, the shear force and bending moment are shown in Figure 36. The contact pressure was calculated in 19×19 Gauss integration points. The contact conditions were enforced on the same 361 points. It is seen that contact occurs on a relatively small surface area which was determined by augmentation. There was no change in the final iterations, the gap between the bodies formed during the shape change: d is of the order of 10^{-3}. As expected, due to the vertical equilibrium, the resulting contact force is 10.0 kN, its line of action passes through the point $X_c = 75.0$, $Y_c = 0.0$.

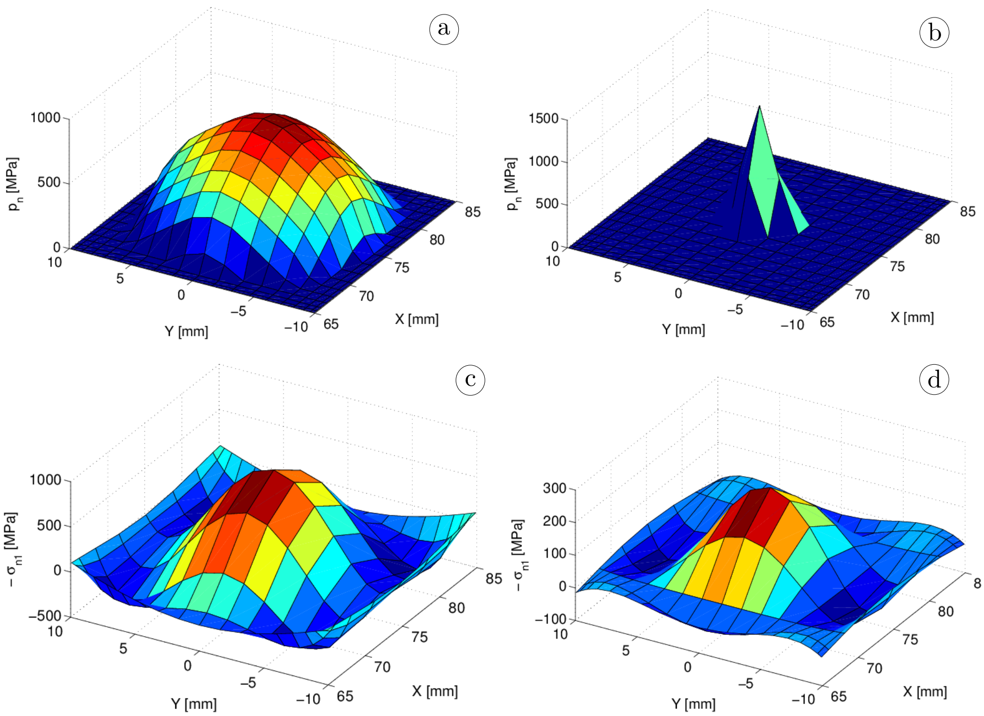

Figure 35. The distribution of the contact pressure in the configuration is shown in this figure for load case 1, a) without augmentation step=1, b) with augmentation, step=13, c), d) normal contact stresses calculated from Hooke's law: c) augmentation step=0, d) augmentation step=13

The symmetry of the displacements is clearly visible in Figure 36b. The normal stress calculated from the derivatives of the displacement field in the contact region via Hooke's law is shown in Figures 35c,d. Owing to the continuity of the approximation fields in the assumed contact region, approximated by one element, we cannot recover the negative of the contact pressure. The pressure is high in the middle of the contact domain, and small at the edges; however, the $hT6$ model cannot accurately represent the pressure distribution with the number of elements used in this example. On the other hand, the contact pressure can be reliably estimated with the augmented Lagrangian technique as indicated below.

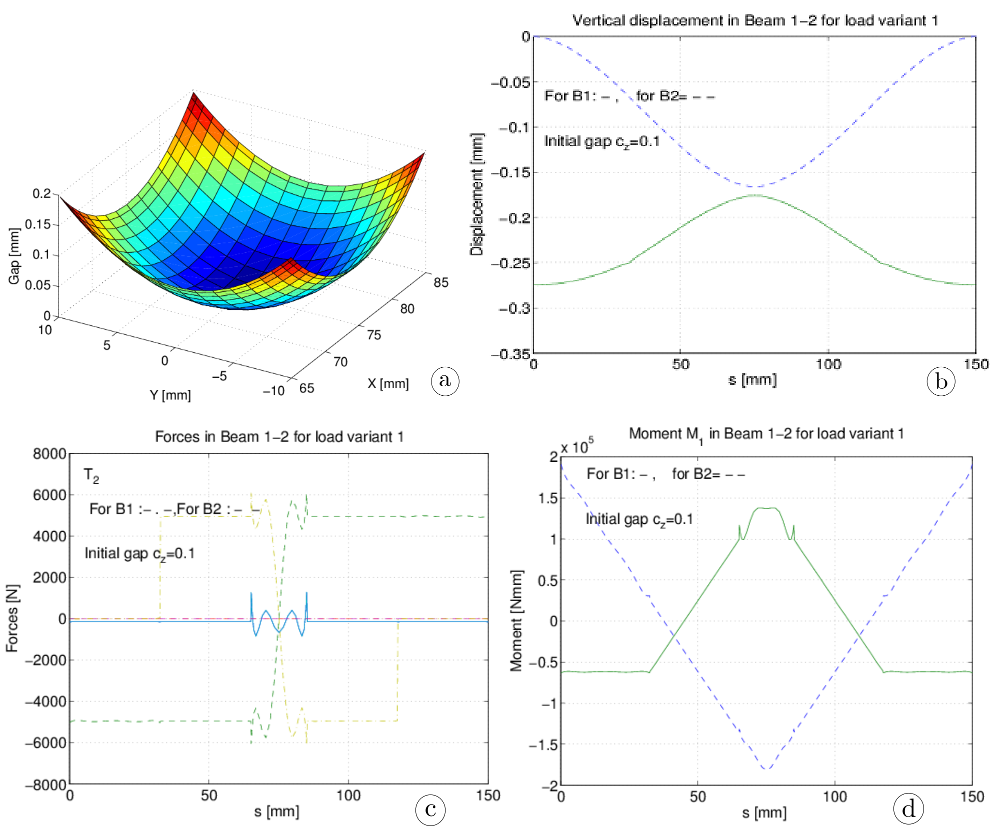

Figure 36. Results for configuration 2 at load case 1, a) initial gap function, b) vertical displacement on middle line of beam, c) distribution of the shear force T, d) bending moment M_1

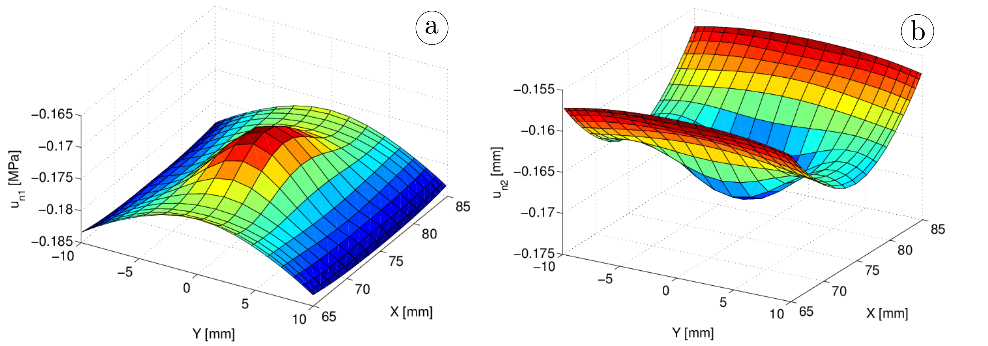

Figure 37. Vertical displacement in the contact zone, a) for body B_1, b) for body B_2 at initial gap $c_z = 0.1$, load case 1

At $c_z = 0$ the initial gap between the supports is zero. The normal stress in the corner points of the contact region is not analytic. The numerical results obtained on a grid of 19×19 Gauss points are shown in Figure 38. The resulting solution is symmetric, resulting from the contact force of $F_{cont} = 10.0$ kN.

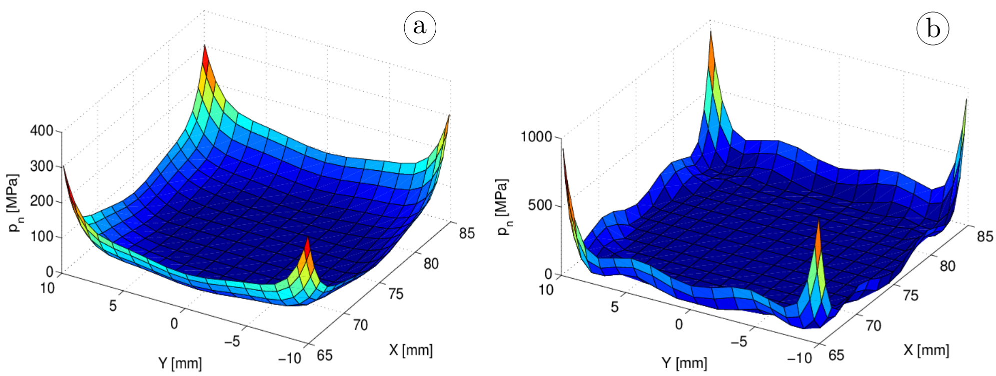

Figure 38. Contact pressure distribution interpolated on a grid of 19×19 Gauss points, a) without augmentation step=1, b) with augmentation, step=13. The initial gap was zero

Load case 2:
The l load is $F_c = -5$ kN (in the $-Z$ direction). Referring to Figure 32, the B and C boundaries are free, A and D are fixed.

We define second-order surfaces by letting $c_z = 0,\ 0.04,\ 0.08,\ 0.12,\ 0.4,\ 0.6,\ 0.8$. The resulting contact pressures and position of contact resulting force are shown in Table 2. Note that as the curvature decreases, the contact area shifts inward of the supposed contact area ($65 \le X \le 85$, $-10 \le Y \le 10$) and extends to a very small surface area.

At $c_z = 0$, the contact is in the left corner of the relevant domain. Then, depending on the curved surfaces of the beams, the contact shifts towards the middle of the assumed contact area.

Table 2. Resulting contact forces and their positions at different parameters c_z

c_z	X_s mm	Y_s mm	F_z kN
0.00	66.41	-9.647	6.740
0.04	67.52	-9.560	6.665
0.08	69.10	-8.596	6.474
0.12	70.68	-6.842	6.297
0.40	72.99	-2.012	6.247
0.60	74.26	-2.100	6.110
0.80	75.00	-1.500	6.049

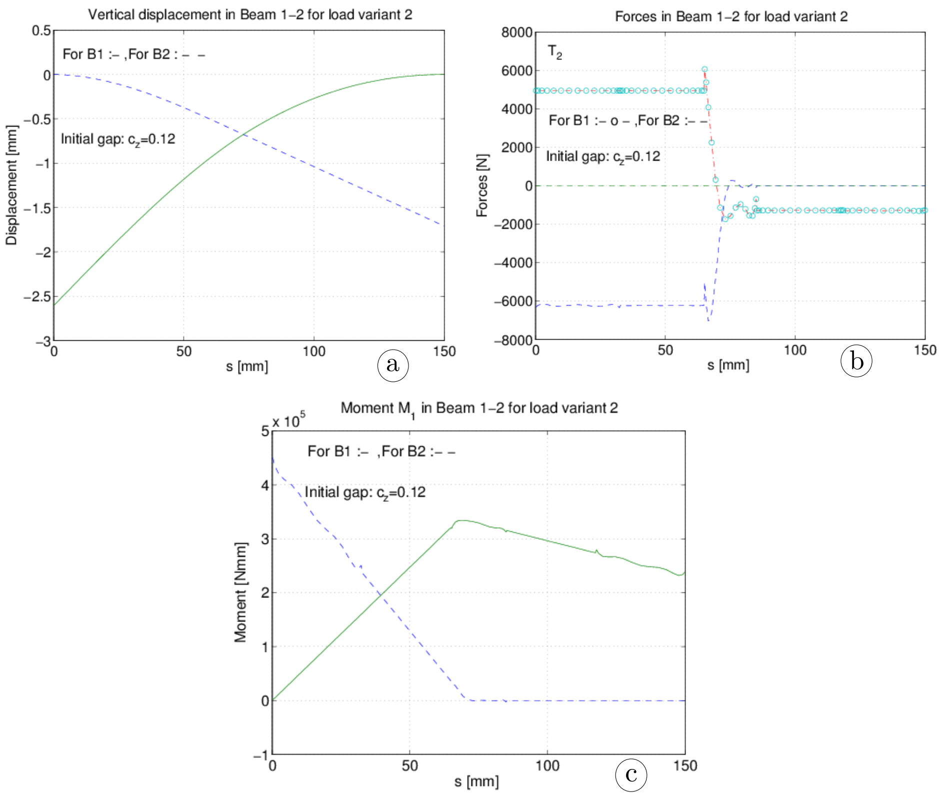

Figure 39. Results for case $c_z = 0.12$ a) vertical displacement on the center line of the beam, b) vertical displacement on middle line of beam, c) distribution of the shear force T_2, d) bending moment M_1

It is also obvious that, as the resultant of the contact pressure moves towards the larger Y by increasing $c_z = 0$, the resulting contact force decreases. The resulting distributions of bending moments and shear forces are essentially the same for different variants. Therefore only one is presented here; Figure 39 represents the case $c_z = 0.12$.

5. Summary and conclusions

We have investigated the algorithmic aspects hierarchic models for elastic rods using sequences of polynomial approximations. The models are semi-discretizations, in which the displacement components that lie in the cross-sectional plane are represented by polynomials of a fixed degree when the rod is homogeneous, or piecewise polynomials when the rod is made of composite materials. These are the director functions. The coefficients of the director functions are functions of the lengthwise coordinate and are discretized by the finite element method. In this way, the three-dimensional problem of elasticity is transformed into sets of one-dimensional problems that can be solved very efficiently. An important practical advantage is that the model form errors as well as the discretization errors can be controlled.

Classical models of rods are extensively used in conventional engineering handbooks and design manuals, see for example [53].

Through application of the algorithmic procedures outlined in this paper, is possible to extend the number and type of entries to a much broader class of problems while removing the limitations inherent in the classical formulations. In other words, numerical techniques, examples of which were discussed in this paper, allow substantial extension of the breadth and depth of the scope of classical engineering handbooks and design manuals.

Smart applications, also called 'simulation apps', are expert-designed in such a way that those applications can be used by engineers whose expertise is not in numerical simulation. The preservation and maintenance of institutional knowledge are among the important objectives of standardization. Economic benefits are realized through improved productivity and improved reliability. The challenging aspects of standardization are that (a) the input parameters have to be suitably restricted so that the assumptions incorporated in the models are not violated and (b) the model form and the discretization errors have to be controlled such that the users' expectation of accuracy, stated in terms of the quantities of interest, is satisfied. The hierarchic formulation outlined in this paper provides the algorithmic foundation for smart applications.

The hierarchical beam models can be advantageously used to solve strength problems through a model containing far fewer unknowns than fully 3D models. The complexities in implementation are compensated for by substantially shortened execution times and increased reliability.

References

1. Szabó, B. and Babuška, I. *Finite Element Analysis.* John Wiley & Sons, 1991.
2. Actis, R. L. "Hierarchic Models for Laminated Plates." PhD. Washington University in St. Louis, USA, 1991.
3. Alesadi, A., Ghazanfari, S., and Shojaee, S. "B-spline finite element approach for the analysis of thin-walled beam structures based on 1D refined theories using Carrera unified formulation." *Thin-Walled Structures,* **130**, (2018), pp. 313–320. doi: 110.1016/j.tws.2018.05.016.
4. Yan, Y., Carrera, E., Pagani, A., Kaleel, I., and de Miguel, A. G. "Isogeometric analysis of 3D straight beam-type structures by Carrera Unified Formulation." *Applied Mathematical Modelling,* **79**, (2020), pp. 768–792. doi: 10.1016/j.apm.2019.11.003.
5. Antmann, S. S. "Theory of Rods." *Handbuch der Physik.* Vol. 6/2. Springer, 1962, pp. 641–703.
6. Carrera, E. and Giunta, G. "Refined beam theories based on an unified formulation." *International Journal of Applied Mechanics,* **2**, (2010), 117–143. doi: 10.1142/S1758825110000500.
7. Carrera, E., Giunta, G., Nali, P., and Petrolo, M. "Refined beam elements with arbitrary cross-section geometries." *Computers and Structures,* **88**, (2010), 283–293. doi: 10.1016/j.compstruc.2009.11.002.
8. Carrera, E. and Petrolo, M. "On the Effectiveness of Higher-Order Terms in Refined Beam Theories." *Journal of Applied Mechanics,* **78**(2), (2010), 021013 (17 pages). doi: 10.1115/1.4002207.
9. Carrera, E., Giunta, G., and Petrolo, M. *Beam Structures: Classical and Advanced Theories.* Wiley-Blackwell, New York, 2011.
10. Carrera, E. and Petrolo, M. "Refined beam elements with only displacement variables and plate/shell capabilities." *Meccanica,* **47**, (2012), 537–556. doi: 10.1007/s11012-011-9466-5.
11. Carrera, E., Pagani, A., and Petrolo, M. "Use of Lagrange multipliers to combine 1D variable kinematic finite elements." *Computers and Structures,* **129**, (2013), 194–206. doi: 10.1016/j.compstruc.2013.07.005.
12. Carrera, E., Cinefra, M., Petrolo, M., and Zappino, E. *Finite Element Analysis of Structures through Unified Formulation.* John Wiley & Sons, London, 2014.
13. Carrera, E., Cinefra, M., Petrolo, M., and Zappino, E. "Comparisons between 1D (Beam) and 2D (Plate/Shell) Finite Elements to Analyze Thin Walled Structures." *Aerotecnica Missili & Spazio, The Journal of Aerospace Science, Technology and Systems,* **93**(3/16), (2014), 1–14. doi: 10.1007/BF03404671.
14. Carrera, E., de Miguel, A. G., and Pagani, A. "Hierarchical theories of structures based on Legendre polynomial expansions with finite element applications." *International Journal of Mechanical Sciences,* **120**, (2017), pp. 286–300. doi: 10.1016/j.ijmecsci.2016.10.009.

15. De Pietro, G., de Miguel, A. G., Carrera, E., Giunta, G., Belouettar, S., and Pagani, A. "Strong and weak form solutions of curved beams via Carrera's unified formulation." *Journal Mechanics of Advanced Materials and Structures* **27**(15) (2018), pp. 1342–1353. doi: 110.1080/15376494.2018.1510066.
16. Li, G. and Carrera, E. "On the mitigation of shear locking in laminated plates through p-version refinement." *Computers and Structures* **225**:106121 (2019). doi: 10.1016/j.compstruc.2019.106121.
17. Moleiro, F., Carrera, E., Zappino, E., Li, G., and Cinefra, M. "Layerwise mixed elements with node-dependent kinematics for global–local stress analysis of multilayered plates using high-order Legendre expansions." *Computer Methods in Applied Mechanics and Engineering,* **359**:112764, (2020). doi: 10.1016/j.cma.2019.112764.
18. Szabó, B. and Sahrmann, G. J. "Hierarchic plate and shell modells based on p-extension." *International Journal for Numerical Methods in Engineering,* **27**, (1988), pp. 1855–1881. doi: 10.1002/nme.1620260812.
19. Carrera, E., Fiordilino, G. A., Nagaraj, M., Pagani, A., and Montemurro, M. "A global/local approach based on CUF for the accurate and efficient analysis of metallic and composite structures." *Engineering Structures,* **188**, (2020), pp. 188–201. doi: 10.1016/j.engstruct.2019.03.016.
20. Li, G., Cinefra, M., and Carrera, E. "Coupled thermo-mechanical finite element models with node-dependent kinematics for multi-layered shell structures." *Journal of Mechanical Sciences,* **171**:105379 (2020). doi: 10.1016/j.ijmecsci.2019.105379.
21. Li, G., Carrera, E., Cinefra, M., de Miguel, A., Pagani, A., and Zappino, E. "An adaptable refinement approach for shell finite element models based on node-dependent kinematics." *Computers and Structures,* **210**, (2019), pp. 1–19. doi: 10.1016/j.compstruct.2018.10.111.
22. Hanten, L., Giunta, G., Belouttar, S., and Salnikov, V. "Free vibration analysis of fibre-metal laminated beams via hierarchical one-dimensional models." *Hindawi Mathematical Problems in Engineering,* Article ID 2724781, 12 pages, (2018). doi: 10.1155/2018/2724781.
23. Nguyen, D. K. and Bui, V. T. "Dynamic analysis of functionally graded timoshenko beams in thermal environment using a higher-order hierarchical beam element." *Hindawi Mathematical Problems in Engineering,* Article ID 7025750, 12 pages, (2017). doi: 10.1155/2017/7025750.
24. Pagani, A., Carrera, E., and Ferreria A. J. M. "Higher-order theories and radial basis functions applied to free vibration analysis of thin-walled beams." *Mechanics of Advanced Materials and Structures,* **23**, (2017), 1080–1091. doi: 10.1080/15376494.2015.1121555.
25. Giunta, G., Belouettar, S., and Carrera, E. "Analysis of FGM beams by means of classical and advanced theories." *Mechanics of Advanced Materials and Structures,* **17**, (2017), 622–635. doi: 10.1080/15376494.2010.518930.

26. Giunta, G., Belouttar, S., and Frreira, A. J. M. "A static analysis of three-dimensional functionally graded beams by hierarchical modelling and collocation meshless solution method." *Acta Mechanica,* **227**, (2016), pp. 969–991. doi: 10.1007/s00707-015-1503-3.
27. Kountsawa, Y., Giunta, G., Nasser, H., and Belouttar, S. "Static analysis of shear actuated piezo-electricbeams via hierarchical one-dimensional FEM theories." *Mechanics of Advanced Materials and Structures,* **22**, (2015), pp. 3–18. doi: 10.1080/15376494.2014.907946.
28. Giunta, G., de Pietro, G., Nasser, H., Beluttar, S., Carrera, E., and Petrolo, M. "A thermal stress finite element analysis of beam structures by hierarchical modelling." *Composites B: Part B, Engineering,* **95**, (2016), pp. 179–195. doi: 10.1016/j.compositesb.2016.03.075.
29. Hui, Y., de Pietro, G., Giunta G., Belouttar, S., Hu, H., Carrera, E., and Pagani, A. "Geometrically nonlinear analysis of beam structures via hierarchical one-dimensional finite elements." *Hindawi Mathematical Problems in Engineering,* Article ID 4821385 (2018). doi: 10.1155/2018/4821385.
30. Petrolo, M., Nagaraj, M. H., Kaleel, I., and Carrera, E. "A global-local approach for the elastoplastic analysis of compact and thin-walled structures via refined models." *Computers and Structures,* **206**, (2018), pp. 54–65. doi: 10.1016/j.compstruc.2018.06.004.
31. Wu, B., Pagani, A., Filippi, M., Chen, W. Q., and Carrera, E. "Large-deflection and post-buckling analyses of isotropic rectangular plates by Carrera Unified Formulation." *International Journal of Non-Linear Mechanics,* **116**, (2019), pp. 18–31. doi: 10.1016/j.ijnonlinmec.2019.05.004.
32. Nagaraj, M. H., Kaleel, I., Carrera, E., and Petrolo, M. "Contact analysis of laminated structures including transverse shear and stretching." *European Journal of Mechanics / A Solids,* **80**,10389, (2020). doi: 10.1016/j.euromechsol.2019.103899.
33. Nagaraj, M. H., Kaleel, I., Carrera, E., and Petrolo, M. "Nonlinear analysis of compact and thin-walled metallic structures including localized plasticity under contact conditions." *Engineering Structure,* **203**, (2020). doi: 10.1016/j.engstruct.2019.109819.
34. Dauge, G. M., Faun, E., and Yosibash, Z. "Plates and Schells: Asymptotic Expansions and Hierarchic models." *Encyclopedia of Computational Mechanics,* ed. by E. Stein, R. de Borst, and T. J. R. Hughes. Vol. 1. 2004, pp. 199–236.
35. Engineering Software Research and Inc. (ESRD) Development. *StressCheck, Version 11.1.* 2023. url: https://esrd.com.
36. SIMULIA software. *ABAQUS, Version 2023.* url: https://www.3ds.com/products-services/simulia/products/abaqus/.
37. Szabó, B. and Babuška, I. *Introduction to Finite Element Analysis: Formulation, Verification and Validation.* John Wiley & Sons, 2011. doi: 10.1002/9781119993834.
38. Páczelt, I., Szabó, B., and Szabó, T. "Solution of contact problem using the *hp* version of the finite element method." *Computers & Mathematics with Applications,* **38**, (2000), pp. 49–69. doi: 10.1016/S0898-1221(99)00261-8.

39. Páczelt, I., Baksa, A., and Szabó, T. "Formulation of the p-extension finite lements for the solution of normal contact probems." *Journal of Computational and Applied Mechanics,* **15**, (2020), pp. 135–172. doi: 10.32973/jcam.2020.009.
40. Franke, D., Düster, A., Nübel, V., and Rank, E. "A comparison of the *h*-, *p*-, *hp*-, and *rp*-version of the FEM for the solution of the 2D Hertzian contact problem." *Computational Mechanics,* **45**, (2010), 513–522. doi: 10.1007/s00466-009-0464-6.
41. Konyukhov, A. and Schweizerhof, K. "Incorporation of contact for high-order finite elements in covariant form." *Computer Methods in Applied Mechanics and Engineering,* **198**, (2009), 1213–1223. doi: 10.1016/j.cma.2008.04.023.
42. Páczelt, I. and Szabó, T. "Solution of contact optimization problems of cylindrical bodies using the hp-FEM." *International Journal for Numerical Methods in Engineering,* **53**, (2002), pp. 123–146. doi: 10.1002/nme.395.
43. Baksa, A., Páczelt, I., and Szabó, T. "Solution of 3D contact problems using spline interpolation." *Journal of Computational and Applied Mechanics,* **9**, (2014), pp. 125–147. doi: 10.32973/jcam.2014.007.
44. Páczelt, I., Mróz, Z., and Baksa, A. "Analysis of steady wear processes for periodic sliding." *Journal of Computational and Applied Mechanics,* **10**, (2015), 231–268. doi: 10.32973/jcam.2015.014.
45. Litewka, P. and Wriggers, P. "Frictional contact between 3D-beams with rectangular cross section." *Computational Mechanics,* **28**, (2002), pp. 26–39. doi: 10.1007/s004660100266.
46. Litewka, P. *Finite Element Analysis of Beam to Beam Contact.* Springer Berlin Heidelberg, 2010. doi: 10.1007/978-3-642-12940-7.
47. Kawa, O. and Litewka, P. "Contact with friction between 3d beams with deformable circular cross sections." *Engineering Transactions,* **63**, (2015), 439–462.
48. O. Kawa, P. Litewka, and R. Studzinski. "Beams with deformable circular cross sections - numerical verification." *Engineering Transactions,* 66, (2018), pp. 281–299.
49. Bucalem, M. L. and Bathe K. J. *The mechanics of solids and structures - hierarchical modeling and the finite element solution.* Springer Heidelberg New York., 2011. doi: 10.1007/978-3-540-26400-2.
50. Konyukhov, A. and Schweizerhof, K. *Computational Contact Mechanics: Geometrically Exact Theory for Arbitrary Shaped Bodies.* Springer Verlag Heidelberg, 2013. doi: 10.1007/978-3-642-31531-2.
51. Wriggers, P. *Computational Contact Mechanics.* Springer Verlag Heidelberg, 2006. doi: 10.1007/978-3-540-32609-0.
52. Strang, G. and Fix, G. J. *An Analysis of the Finite Element Method.* Prentice-Hall, Inc. Englewood Cliffs, N. J., 1973.
53. Budynas, R. G. and Sadegh, A. M. *Roark's Formulas for Stress and Strain.* McGraw-Hill Education, 2020.

54. Páczelt, I. and Beleznai, R. "Nonlinear contact-theory for analysis of wire rope strand using high-order approximation in the FEM." *Computers and Structures,* **8**, (2011), pp. 1004–1025. DOI: 10.1016/j.compstruc.2011.01.011.

Appendix A. The Pascal Triangle

The Pascal triangle is the set of monomial functions shown below:

$$\begin{array}{cr}
1 & \\
x \;\; y & h1\\
x^2 \;\; xy \;\; y^2 & h2\\
x^3 \;\; x^2y \;\; xy^2 \;\; y^3 & h3\\
x^4 \;\; x^3y \;\; x^2y^2 \;\; xy^3 \;\; y^4 & h4\\
x^5 \;\; x^4y \;\; x^3y^2 \;\; x^2y^3 \;\; xy^4 \;\; y^5 & h5\\
x^6 \;\; x^5y \;\; x^4y^2 \;\; x^3y^3 \;\; x^2y^4 \;\; xy^5 \;\; y^6 & h6\\
x^7 \;\; x^6y \;\; x^5y^2 \;\; x^4y^3 \;\; x^3y^4 \;\; x^2y^5 \;\; xy^6 \;\; y^7 & h7\\
x^8 \;\; x^7y \;\; x^6y^2 \;\; x^5y^3 \;\; x^4y^4 \;\; x^3y^5 \;\; x^2y^6 \;\; xy^7 \;\; y^8 & h8
\end{array}$$

Appendix B. Mathematical transformations

In the present Appendix we detail the calculations for the terms in equation (16).

$$\mathbf{q}_I^{G,T} = \left[\begin{array}{cccccc} u_{0X} & u_{0Y} & u_{0Z} & \chi_X & \chi_Y & \chi_Z \end{array}\right], \quad I \to J, \quad \mathbf{q}^T = \left[\mathbf{q}_I^G \quad \mathbf{q}_J^G\right]^T \tag{B.1}$$

interpreted in the local system:

$$\mathbf{u_0}^{L,T} = \left[\begin{array}{ccc} u_{01} & u_{02} & u_{03} \end{array}\right], \qquad \chi^{L,T} = \left[\begin{array}{ccc} \chi_1 & \chi_2 & \chi_3 \end{array}\right] \tag{B.2}$$

formally, the center line displacement, angular rotation and their derivatives with respect to s are approximated in the form:

$$\left[\begin{array}{c} \mathbf{u}_0 \\ \chi \end{array}\right]^L = \mathbf{G}_{u\chi}\,\mathbf{q} + \mathbf{\Phi}_{u\chi,p}\,\mathbf{a}^{u\chi,p}, \qquad \left[\begin{array}{c} \mathbf{u}_0' \\ \chi' \end{array}\right]^L = \mathbf{G}_{u\chi}'\,\mathbf{q} + \mathbf{\Phi}_{u\chi,p}'\,\mathbf{a}^{u\chi,p} \tag{B.3}$$

where $\mathbf{G}_{u\chi}$ is the matrix [54] linearly approximating rigid-body and elastic displacements, $\mathbf{\Phi}_{u\chi,p}$ is the matrix containing polynomials depending on the degree p, and is the vector of additional constants. The vector in equation (10), taking into account equation (B.3), can be written as

$$\tilde{\psi}_0 = \mathbf{G}^0\,\mathbf{q} + \mathbf{\Phi}_p^0\,\mathbf{a}^{0p}, \quad \mathbf{G}^0 = \left[\begin{array}{c} \mathbf{G}_{u\chi} \\ \mathbf{G'}_{u\chi} \end{array}\right], \quad \mathbf{\Phi}_p^0 = \left[\begin{array}{c} \mathbf{\Phi}_{u\chi,p} \\ \mathbf{\Phi'}_{u\chi,p} \end{array}\right]. \tag{B.4}$$

By substituting equation (B.4) into equation (24), the stiffness matrix of the finite element formulation is produced [1, 37].

In some detail

$$\mathbf{\Phi}_{u\chi,p} = \left[\begin{array}{cc} \mathbf{\Phi}_{0p} & \mathbf{0} \\ \mathbf{0} & \mathbf{\Phi}_{0p} \end{array}\right] = \left[\begin{array}{c} \mathbf{\Phi}_{up} \\ \mathbf{\Phi}_{\chi p} \end{array}\right], \quad \mathbf{\Phi'}_{u\chi,p} = \left[\begin{array}{cc} \mathbf{\Phi}_{0p}' & \mathbf{0} \\ \mathbf{0} & \mathbf{\Phi}_{0p}' \end{array}\right] = \left[\begin{array}{c} \mathbf{\Phi}_{up}' \\ \mathbf{\Phi}_{\chi p}' \end{array}\right] \tag{B.5}$$

Letting $\bar{s} = s/L$, where L is the length of the center line of the element, the derivative with respect to s can be calculated based on

$$(.)' = \frac{d(.)}{ds} = \frac{1}{L}\frac{d(.)}{d\bar{s}}.$$

We have

$$\underset{(3,3\times np)}{\mathbf{\Phi}_{0p}} = \begin{bmatrix} \bar{s}^2-\bar{s} & \bar{s}^3-\bar{s} & \cdots & \bar{s}^p-\bar{s} & 0 & 0 & \cdots & 0 & 0 & 0 & \cdots & 0 \\ 0 & 0 & \cdots & 0 & \bar{s}^2-\bar{s} & \bar{s}^3-\bar{s} & \cdots & \bar{s}^p-\bar{s} & 0 & 0 & \cdots & 0 \\ 0 & 0 & \cdots & 0 & 0 & 0 & \cdots & 0 & \bar{s}^2-\bar{s} & \bar{s}^3-\bar{s} & \cdots & \bar{s}^p-\bar{s} \end{bmatrix}, \tag{B.6a}$$

$$\underset{(3,3\times np)}{\mathbf{\Phi}'_{0p}} = \frac{1}{L}\begin{bmatrix} 2\bar{s}-1 & \cdots & p\bar{s}^{p-1}-1 & 0 & \cdots & 0 & 0 & \cdots & 0 \\ 0 & \cdots & 0 & 2\bar{s}-1 & \cdots & p\bar{s}^{p-1}-1 & 0 & \cdots & 0 \\ 0 & \cdots & 0 & 0 & \cdots & 0 & 2\bar{s}-1 & \cdots & p\bar{s}^{p-1}-1 \end{bmatrix} \tag{B.6b}$$

and

$$\underset{(1,6np)}{\mathbf{a}^{0p,T}} = \left[\mathbf{a}_u^{p,T}\ \mathbf{a}_\chi^{p,T}\right] \tag{B.7}$$

in which

$$\underset{(1,3\times np)}{\mathbf{a}_u^{p,T}} = \left[a_{u1}^{p=2}\ a_{u1}^{p=3}\ ,...,a_{u1}^{p}\ a_{u2}^{p=2}\ a_{u2}^{p=3},...,a_{u2}^{p}\ a_{u3}^{p=2}\ a_{u3}^{p=3},...,a_{u3}^{p}\right],$$

$$\underset{(1,3\times np)}{\mathbf{a}_\chi^{p,T}} = \left[a_{\chi1}^{p=2}\ a_{\chi1}^{p=3}\ ,...,a_{\chi1}^{p}\ a_{\chi2}^{p=2}\ a_{\chi2}^{p=3},...,a_{\chi2}^{p}\ a_{\chi3}^{p=2}\ a_{\chi3}^{p=3},...,a_{\chi3}^{p}\right].$$

In Model-1 the matrix of strains is:

$$\boldsymbol{\varepsilon} = \begin{bmatrix} \varepsilon_1 \\ \varepsilon_2 \\ \varepsilon_3 \\ \gamma_{12} \\ \gamma_{13} \\ \gamma_{23} \end{bmatrix} = \left[\mathbf{\Gamma}_{1(0)}\ \mathbf{\Gamma}_{1(1)}\right]\begin{bmatrix} \tilde{\boldsymbol{\psi}}_0 \\ \tilde{\boldsymbol{\psi}}^{h^{(1)}} \end{bmatrix} = \mathbf{\Gamma}_1\tilde{\boldsymbol{\psi}}_1 \tag{B.8}$$

Using equations (10) and (11), the 16 functions are approximated as

$$\tilde{\boldsymbol{\psi}}_1 = \begin{bmatrix} \tilde{\boldsymbol{\psi}}_0 \\ \tilde{\boldsymbol{\psi}}^{h^{(1)1}} \end{bmatrix} = \begin{bmatrix} \tilde{\boldsymbol{\psi}}_0 \\ \mathbf{h}^{h^{(1)1}} \\ \mathbf{h}^{h^{(1)1}\prime} \end{bmatrix} = \begin{bmatrix} \mathbf{G}^0 & \mathbf{0} \\ \mathbf{0} & \mathbf{G}^{h^{(1)1}} \\ \mathbf{0} & \mathbf{G}^{h^{(1)1}\prime} \end{bmatrix}\begin{bmatrix} \mathbf{q} \\ \mathbf{q}^{h^{(1)1}} \end{bmatrix} +$$

$$+\begin{bmatrix} \mathbf{\Phi}_p^0 & \mathbf{0} \\ \mathbf{0} & \mathbf{\Phi}_p^{h^{(1)1}} \\ \mathbf{0} & \mathbf{\Phi}_p^{h^{(1)1}\prime} \end{bmatrix}\begin{bmatrix} \mathbf{a}^{0p} \\ \mathbf{a}^{h^{(1)1}p} \end{bmatrix} = \mathbf{G}_1^{total}\mathbf{q}^1 + \mathbf{\Phi}_{1p}^{total}\mathbf{a}^{1p} \tag{B.9}$$

where

$$\mathbf{G}^{h^{(1)1}} = \begin{bmatrix} 1-\bar{s} & 0 & \bar{s} & 0 \\ 0 & 1-\bar{s} & 0 & \bar{s} \end{bmatrix}, \quad \mathbf{G}^{h^{(1)1}\prime} = \frac{1}{L}\begin{bmatrix} -1 & 0 & 1 & 0 \\ 0 & -1 & 0 & 1 \end{bmatrix}, \tag{B.10}$$

$$\underset{(2,2\times np)}{\mathbf{\Phi}_p^{h^{(1)1}}} = \begin{bmatrix} \bar{s}^2-\bar{s} & \bar{s}^3-\bar{s} & \cdots & \bar{s}^p-\bar{s} & 0 & 0 & \cdots & 0 \\ 0 & 0 & \cdots & 0 & \bar{s}^2-\bar{s} & \bar{s}^3-\bar{s} & \cdots & \bar{s}^p-\bar{s} \end{bmatrix}, \tag{B.11a}$$

$$\underset{(2,2\times np)}{\mathbf{\Phi}_p^{h^{(1)1}\prime}} = \begin{bmatrix} 2\bar{s}-1 & 3\bar{s}^2-1 & \cdots & p\bar{s}^{p-1}-1 & 0 & 0 & \cdots & 0 \\ 0 & 0 & \cdots & 0 & 2\bar{s}-1 & 3\bar{s}^2-1 & \cdots & p\bar{s}^{p-1}-1 \end{bmatrix}, \tag{B.11b}$$

$$\mathbf{q}^{1T} = \left[\mathbf{q}_I^T, \mathbf{q}_J^T,\ \mathbf{q}_I^{h^{(1)1}T}, \mathbf{q}_J^{h^{(1)1}T}\right], \qquad \mathbf{q}_I^{h^{(1)1}T} = \left[u_{1x}\ u_{2y}\right]_I$$
$$I \to J \tag{B.12}$$
$$\mathbf{a}^{h^{(1)1}pT} = \left[a_{1x}^{p=2}, a_{1x}^{p=3}, ...,\ a_{1x}^{p}; a_{2y}^{p=2}, a_{2y}^{p=3}, ...,\ a_{2y}^{p}\right].$$

Based on the previous equations, it is seen that the strain vector for the *hm*-th model is:

$$\boldsymbol{\varepsilon}=\begin{bmatrix}\varepsilon_1\\ \varepsilon_2\\ \varepsilon_3\\ \gamma_{12}\\ \gamma_{13}\\ \gamma_{23}\end{bmatrix}=[\boldsymbol{\Gamma}_1\ \ \boldsymbol{\Gamma}_{h^{(2)}}\ldots\boldsymbol{\Gamma}_{h^{(m-1)}}\ \boldsymbol{\Gamma}_{h^{(m)}}\ ]\begin{bmatrix}\tilde{\boldsymbol{\psi}}_1\\ \tilde{\boldsymbol{\psi}}^{h^{(2)}}\\ \cdots\\ \tilde{\boldsymbol{\psi}}^{h^{(m-1)}}\\ \tilde{\boldsymbol{\psi}}^{h^{(m)}}\end{bmatrix}=$$

$$=\boldsymbol{\Gamma}_m\begin{bmatrix}\tilde{\boldsymbol{\psi}}_{m-1}\\ \tilde{\boldsymbol{\psi}}^{h^{(m)}}\end{bmatrix}=\boldsymbol{\Gamma}_m\tilde{\psi}_m=\mathbf{G}_m^{total}\mathbf{q}^m+\boldsymbol{\Phi}_{mp}^{total}\mathbf{a}^{mp},\quad \text{(B.13)}$$

where

$$\tilde{\boldsymbol{\psi}}^{h^{(m)}}=\begin{bmatrix}\mathbf{h}^{(m)}\\ \mathbf{h}^{(m)\prime}\end{bmatrix}=\begin{bmatrix}\mathbf{G}^{h^{(m)}}\\ \mathbf{G}^{h^{(m)\prime}}\end{bmatrix}\mathbf{q}^{h^{(m)}}+\begin{bmatrix}\boldsymbol{\Phi}p^{h^{(m)}}\\ \boldsymbol{\Phi}p^{h^{(m)}\prime}\end{bmatrix}\mathbf{a}^{h^{(m)}p},\quad \text{(B.14)}$$

$$\tilde{\boldsymbol{\psi}}_m=\begin{bmatrix}\tilde{\boldsymbol{\psi}}_{m-1}\\ \tilde{\boldsymbol{\psi}}^{h^{(m)}}\end{bmatrix}=\begin{bmatrix}\mathbf{G}_{m-1}^{total} & \mathbf{0}\\ \mathbf{0} & \mathbf{G}^{h^{(m)}}\\ \mathbf{0} & \mathbf{G}^{h^{(m)}\prime}\end{bmatrix}\begin{bmatrix}\mathbf{q}^{m-1}\\ \mathbf{q}^{h^{(m)}}\end{bmatrix}+$$

$$+\begin{bmatrix}\boldsymbol{\Phi}_{mp}^{total} & \mathbf{0}\\ \mathbf{0} & \boldsymbol{\Phi}_p^{h^{(m)}}\\ \mathbf{0} & \boldsymbol{\Phi}_p^{h^{(m)\prime}}\end{bmatrix}\begin{bmatrix}\mathbf{a}^{m-1,p}\\ \mathbf{a}^{h^{(m)},p}\end{bmatrix}=\mathbf{G}_m^{total}\mathbf{q}^m+\boldsymbol{\Phi}_{mp}^{total}\mathbf{a}^{mp},\quad \text{(B.15)}$$

$$\begin{aligned}\mathbf{G}^{h^{(m)}}&=\begin{bmatrix}\mathbf{G}_{h^{(m)}1} & \mathbf{0} & \mathbf{0} & \mathbf{G}_{h^{(m)}2} & \mathbf{0} & \mathbf{0}\\ \mathbf{0} & \mathbf{G}_{h^{(m)}1} & \mathbf{0} & \mathbf{0} & \mathbf{G}_{h^{(m)}2} & \mathbf{0}\\ \mathbf{0} & \mathbf{0} & \mathbf{G}_{h^{(m)}1} & \mathbf{0} & \mathbf{0} & \mathbf{G}_{h^{(m)}2}\end{bmatrix},\\ \mathbf{G}^{h^{(m)\prime}}&=\begin{bmatrix}\mathbf{G}'_{h^{(m)}1} & \mathbf{0} & \mathbf{0} & \mathbf{G}'_{h^{(m)}2} & \mathbf{0} & \mathbf{0}\\ \mathbf{0} & \mathbf{G}'_{h^{(m)}1} & \mathbf{0} & \mathbf{0} & \mathbf{G}'_{h^{(m)}2} & \mathbf{0}\\ \mathbf{0} & \mathbf{0} & \mathbf{G}'_{h^{(m)}1} & \mathbf{0} & \mathbf{0} & \mathbf{G}'_{h^{(m)}2}\end{bmatrix},\end{aligned}\quad \text{(B.16)}$$

$$\begin{aligned}\mathbf{G}_{h^{(m)}1}&=(1-\bar{s})\mathbf{E}_{(m+1,m+1)},\quad \mathbf{G}_{h^{(m)}2}=\bar{s}\mathbf{E}_{(m+1,m+1)},\\ \mathbf{G}'_{h^{(m)}1}&=-\frac{1}{L}\mathbf{E}_{(m+1,m+1)},\quad \mathbf{G}'_{h^{(m)}2}=\frac{1}{L}\mathbf{E}_{(m+1,m+1)},\end{aligned}\quad \text{(B.17)}$$

in which $\mathbf{E}_{(m+1,m+1)}$ is the unit matrix of size $(m+1,m+1)$, $\bar{s}=s/L$, $0\le\bar{s}\le 1$. Furthermore

$$\underset{(3\times(m+1),np\times(m+1))}{\boldsymbol{\Phi}_p^{h^{(m)}}}=\begin{bmatrix}\boldsymbol{\Phi}_{h^{(m)}p} & & \\ \mathbf{0} & \boldsymbol{\Phi}_{h^{(m)}p} & \\ \mathbf{0} & \mathbf{0} & \boldsymbol{\Phi}_{h^{(m)}p}\end{bmatrix},\quad m=2,3,4,5,6\quad \text{(B.18)}$$

$$\underset{(3\times(m+1),np\times(m+1))}{\boldsymbol{\Phi}_p^{h^{(m)}\prime}}=\begin{bmatrix}\boldsymbol{\Phi}'_{h^{(m)}p} & & \\ \mathbf{0} & \boldsymbol{\Phi}'_{h^{(m)}p} & \\ \mathbf{0} & \mathbf{0} & \boldsymbol{\Phi}'_{h^{(m)}p}\end{bmatrix},\quad m=2,3,4,5,6\quad \text{(B.19)}$$

$$\underset{(m+1,np\times(m+1))}{\boldsymbol{\Phi}_{h^{(m)}p}}=$$

$$= \begin{bmatrix} \bar{s}^2-\bar{s} & \bar{s}^3-\bar{s} & \cdots & \bar{s}^p-\bar{s} & 0 & 0 & \cdots & 0 & 0 & 0 & \cdots & 0 \\ \cdots & & & & & & & & & & & \cdots \\ \cdots & & & & & & & & & & & \cdots \\ 0 & 0 & \cdots & 0 & \bar{s}^2-\bar{s} & \bar{s}^3-\bar{s} & \cdots & \bar{s}^p-\bar{s} & 0 & 0 & \cdots & 0 \\ \cdots & & & & & & & & & & & \cdots \\ \cdots & & & & & & & & & & & \cdots \\ 0 & 0 & \cdots & 0 & 0 & 0 & \cdots & 0 & \bar{s}^2-\bar{s} & \bar{s}^3-\bar{s} & \cdots & \bar{s}^p-\bar{s} \end{bmatrix} \begin{bmatrix} 1 \\ \cdots \\ \cdots \\ i \\ \cdots \\ \cdots \\ m+1 \end{bmatrix}$$

For the sake of brevity, we provide the additional unknowns of the finite element for the $h2$ model only:

$$\mathbf{q}^{2T} = \left[\mathbf{q}_I^{1T}, \mathbf{q}_J^{1T},\ \mathbf{q}_I^{h^{(2)}T},\ \mathbf{q}_J^{h^{(2)}T}\right] \tag{B.20}$$

$$\begin{gathered} \mathbf{q}_I^{h^{(2)}T} = \left[\left[u_{1x^2}\ \ u_{2xy}\ u_{3y^2}\right]_I\ \left[u_{2x^2}\ \ u_{2xy}\ u_{2y^2}\right]_I\ \left[u_{3x^2}\ \ u_{3xy}\ u_{3y^2}\right]_I\right], \quad I \to J \\ \mathbf{a}^{h^{(2)}pT} = \left[\mathbf{a}_1^{h^{(2)}pT}, \mathbf{a}_2^{h^{(2)}pT}, \mathbf{a}_3^{h^{(2)}pT}\right], \\ \mathbf{a}_i^{h^{(2)}pT} = \left[a_{ix^2}^{p=2}, a_{ix^2}^{p=3}, ...,\ a_{ix^2}^{p}; a_{ixy}^{p=2}, a_{ixy}^{p=3}, ...,\ a_{ixy}^{p}; a_{iy^2}^{p=2}, a_{iy^2}^{p=3}, ...,\ a_{iy^2}^{p}\right],\ \ i=1,2,3 \end{gathered} \tag{B.21}$$

Continuing the construction of the models based on (B.15), for the $h6$ model we get:

$$\boldsymbol{\varepsilon} = \begin{bmatrix} \varepsilon_1 \\ \varepsilon_2 \\ \varepsilon_3 \\ \gamma_{12} \\ \gamma_{13} \\ \gamma_{23} \end{bmatrix} = \left[\boldsymbol{\Gamma}_1\ \ \boldsymbol{\Gamma}_{h^{(2)}}\ \boldsymbol{\Gamma}_{h^{(3)}}\ \boldsymbol{\Gamma}_{h^{(4)}}\ \boldsymbol{\Gamma}_{h^{(5)}}\ \boldsymbol{\Gamma}_{h^{(6)}}\ \right] \begin{bmatrix} \tilde{\boldsymbol{\psi}}_1 \\ \tilde{\boldsymbol{\psi}}^{h^{(2)}} \\ \tilde{\boldsymbol{\psi}}^{h^{(3)}} \\ \tilde{\boldsymbol{\psi}}^{h^{(4)}} \\ \tilde{\boldsymbol{\psi}}^{h^{(5)}} \\ \tilde{\boldsymbol{\psi}}^{h^{(6)}} \end{bmatrix} = \boldsymbol{\Gamma}_6 \tilde{\boldsymbol{\psi}}_6 \tag{B.22}$$

Furthermore

$$\mathbf{G}_6^{total} = \begin{bmatrix} \mathbf{G}^1 & 0 & 0 & 0 & 0 & 0 \\ 0 & \mathbf{G}^{h^{(2)}} & 0 & 0 & 0 & 0 \\ 0 & \mathbf{G}^{h^{(2)\prime}} & 0 & 0 & 0 & 0 \\ 0 & 0 & \mathbf{G}^{h^{(3)}} & 0 & 0 & 0 \\ 0 & 0 & \mathbf{G}^{h^{(3)\prime}} & 0 & 0 & 0 \\ 0 & 0 & 0 & \mathbf{G}^{h^{(4)}} & 0 & 0 \\ 0 & 0 & 0 & \mathbf{G}^{h^{(4)\prime}} & 0 & 0 \\ 0 & 0 & 0 & 0 & \mathbf{G}^{h^{(5)}} & 0 \\ 0 & 0 & 0 & 0 & \mathbf{G}^{h^{(5)\prime}} & 0 \\ 0 & 0 & 0 & 0 & 0 & \mathbf{G}^{h^{(6)}} \\ 0 & 0 & 0 & 0 & 0 & \mathbf{G}^{h^{(6)\prime}} \end{bmatrix} \tag{B.23a}$$

and

$$\mathbf{\Phi}_6^{total} = \begin{bmatrix} \mathbf{\Phi}^1 & 0 & 0 & 0 & 0 & 0 \\ 0 & \mathbf{\Phi}^{h^{(2)}} & 0 & 0 & 0 & 0 \\ 0 & \mathbf{\Phi}^{h^{(2)\prime}} & 0 & 0 & 0 & 0 \\ 0 & 0 & \mathbf{\Phi}^{h^{(3)}} & 0 & 0 & 0 \\ 0 & 0 & \mathbf{\Phi}^{h^{(3)\prime}} & 0 & 0 & 0 \\ 0 & 0 & 0 & \mathbf{\Phi}^{h^{(4)}} & 0 & 0 \\ 0 & 0 & 0 & \mathbf{\Phi}^{h^{(4)\prime}} & 0 & 0 \\ 0 & 0 & 0 & 0 & \mathbf{\Phi}^{h^{(5)}} & 0 \\ 0 & 0 & 0 & 0 & \mathbf{\Phi}^{h^{(5)\prime}} & 0 \\ 0 & 0 & 0 & 0 & 0 & \mathbf{\Phi}^{h^{(6)}} \\ 0 & 0 & 0 & 0 & 0 & \mathbf{\Phi}^{h^{(6)\prime}} \end{bmatrix} \tag{B.23b}$$

Table 3. Main characteristics of hm models

Hierarch. model	NDOF in one nodal point	Number of inner nodal points	Number of nodes for one element	AD=Additional (inner) deegre	NDOF for one element
$h1$	6	6	8	$6(p-1)$	$12+AD$
$h2$	15	15	17	$15(p-1)$	$30+AD$
$h3$	27	27	29	$27(p-1)$	$54+AD$
$h4$	42	42	44	$42(p-1)$	$84+AD$
$h5$	60	60	62	$60(p-1)$	$120+AD$
$h6$	81	81	83	$81(p-1)$	$162+AD$

Journal of Computational and Applied Mechanics, Vol. 18, No. 1, (2023), pp. 85–95
DOI: 10.32973/jcam.2023.003

POST-EXTRAPOLATION FOR SPECIFIED TIME-STEP RESULTS WITHOUT INTERPOLATION, IN MOC-BASED 1D HYDRAULIC TRANSIENTS AND GAS RELEASE COMPUTATIONS

Abdallah A. Estuti
Department of Maintenance and Projects
National Oil Company – Tripoli Libya
P.O. Box 13665
aestuti@noc.ly
abdalla.estuti@gmail.com

E. Litvai†
Department of Fluid Mechanics
Budapest University of Technology and Economics,
H-1111 Budapest, Bertalan Lajos u. 4-6., Hungary

[Received: March 7, 2023; Accepted: May 18, 2023]

Abstract. The goal of the paper is to present a supplementary step called post-extrapolation. When applied to the well-known method of characteristics (MOC), this assures the continuous use of the specified time steps or regular numerical grid without interpolations during computations of transients in 1D 2-phase flow in straight elastic pipes. The new method consists of two steps, the first being a typical MOC step, where the C^- and C^+ characteristics start from regular nodal points, allowing for the point of intersection to differ from a regular one. After defining the variables there the method transforms it corresponding to the near regular grid point, using the first derivatives contained in the original, nonlinear, governing equations, as evaluated numerically from the variables got earlier in the neighboring nodes. The procedure needs no interpolations; it deals with grid-point values only. Instead of the Courant-type stability conditions, shock-wave catching and smoothing techniques help to assure numerical stability between broad limits of parameters like the closing time of a valve and the initial gas content of the fluid. Comparison by runs with traditional codes under itemized boundary conditions and measurements on a simple TPV (tank-pipe-valve) setup show acceptable scatter.

Keywords: MOC, gas release, post-extrapolation, shock catching, transients

1. Introduction

In this paper we would like to introduce a new method, or rather a supplementary step called post-extrapolation. It is applied to the well-known method of characteristic (MOC), which assures the continuous use of a regular grid $(\Delta x, \Delta t)$ defined by

$$\Delta x = a_0 \Delta t \tag{1}$$

where a_0 = constant, Δt = constant being a specific time step. Since grid point-values of the variables are used, no interpolations are necessary. This is in contrast to the traditional case, where the Courant-type numerical stability criteria need interpolation, especially in two-phase fluid where the changes in gas content cause steep variations in the pressure wave celerity a. These problems will be treated in the next sections. First the basic equations are introduced.

For 1D two-phase pipe-flow the momentum equation used reads:

$$\frac{\partial u}{\partial t} + u\frac{\partial u}{\partial x} = -\frac{1}{\rho}\frac{\partial p}{\partial x} - \frac{\lambda}{2D}u\,|u| - g\sin\alpha\,. \tag{2}$$

The density of the fluid ρ can be expressed by the void fraction V; by the density of the liquid ρ_w and by the density of the gas or air contained in the fluid ρ_g as

$$\rho = (1-V)\,\rho_w + V\rho_g\,. \tag{3}$$

This helps to introduce the dimensionless density ratio

$$R_o = \frac{\rho_w}{\rho} = \frac{1}{1-\left(1-\frac{\rho_g}{\rho_w}\right)V}\,. \tag{4}$$

With the pressure head defined by

$$P = \rho_w g H$$

and with volume flow rate $Q = uA$ the momentum equation can be transformed

$$\frac{\partial Q}{\partial t} + \frac{Q}{A}\frac{\partial Q}{\partial x} + R_o A g\frac{\partial H}{\partial x} + \frac{\lambda}{2DA}Q\,|Q| + gA\sin\alpha = 0. \tag{5}$$

The continuity equation

$$\frac{\partial \rho}{\partial t} + \frac{\partial}{\partial x}(\rho u) = 0 \tag{6}$$

can be transformed by introducing the celerity a of the pressure waves:

$$\frac{1}{a^2} = \frac{\partial \rho}{\partial p} \tag{7}$$

to

$$\frac{\partial p}{\partial t} + u\frac{\partial p}{\partial x} + a^2\rho\frac{\partial u}{\partial x} = 0\,, \tag{8}$$

$$R_o\frac{\partial H}{\partial t} + \frac{Q}{A}R_o\frac{\partial H}{\partial x} + \frac{a^2}{Ag}\frac{\partial Q}{\partial x} = 0\,. \tag{9}$$

2. Equations of characteristics

Since the first part of the new method requires the method of characteristics, the usual procedure (see e.g. Wylie & Streeter [1]) with governing equations (5) and (9) leads to the following equations for the characteristics $C^{\mp}$:

$$\frac{dQ}{dt} \mp Ro\frac{ga}{A}\frac{dH}{dt} + gA\sin\alpha + \frac{\lambda}{2DA}Q\,|Q| = 0\,, \tag{10}$$

$$\frac{dx}{dt} = \frac{Q}{A} \mp a, \tag{11}$$

where the negative sign refers to the C^- characteristic.

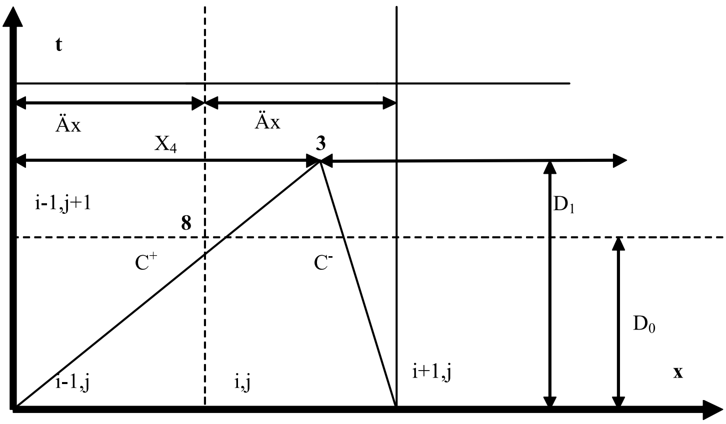

Figure 1. Notations of key nodal points in post-extrapolation

Figure 1 shows the point of intersection 3, the characteristic started in point $(i-1, j)$ and $(i+1, j)$, respectively. Its coordinates (x_4, D_1) can be taken from the equations for C^+

$$\left(\frac{dx}{dt}\right) = \frac{Q(i+1)}{A} + a(i) = \frac{x_4}{D_1}, \tag{12}$$

for C^-

$$\left(\frac{dx}{dt}\right) = \frac{U\,(i+1)}{A} - a(i) = \frac{x_4 - 2\Delta x}{D_1} \tag{13}$$

by introducing the following quantities

$$N_3 = \frac{Q\,(i-1) - U\,(i+1)}{A} + 2a(i)\,, \tag{14}$$

$$D_1 = 2\frac{\Delta x}{N_3}\,, \tag{15}$$

$$x_4 = D_1\frac{Q\,(i-1)}{A} + a(i)\,, \tag{16}$$

where $U\,(i+1) = Q\,(i+1)$ if $H\,(i+1) > H_v$, else see equations later. The values of the variables Q and H at point 3 in Figure 1, or U and H can be computed as usual by integrating equation (10) from t to $t + D_1$. From the integral along C^+ after transformations we obtain

$$H_3 = C_1 - B_1 Q_3 \tag{17}$$

with

$$C_1 = H\,(i+1) - BQ\,(i-1) - a\,(i)\,\frac{D_1}{R_o}\sin\alpha\,, \tag{18}$$

$$B_1 = B + R\,|Q(i-1)|\,\frac{a(i)}{\Delta x}D_1\,, \tag{19}$$

where

$$B = \frac{a(i)}{R_o g A}, \qquad R = \frac{\lambda \Delta x}{2gR_o DA^2}\,. \tag{20}$$

Similarly, integrating along C^- results in

$$H_3 = C_2 + B_2 Q_3 \,, \tag{21}$$

$$C_2 = H(i+1) - BQ(I+1) + a(i)\frac{D_1}{R_o}\sin\alpha \,, \tag{22}$$

$$B_2 = B + R\,|Q(i+1)|\,\frac{a(i)}{\Delta x}D_1 \,. \tag{23}$$

The difference of equations (17) and (21) yields

$$Q_3 = \frac{C_1 - C_2}{B_1 + B_2} \,. \tag{24}$$

It also holds that

$$H_3 = \frac{C_1 B_2 + C_2 B_1}{B_1 + B_2} \,. \tag{25}$$

Hence $U_3 = Q_3$.
If, however, $H_3 \le H_v$ then $H_3 = H_v$, i.e, cavity should be be prescribed. Then

$$U_3 = \frac{C_1 - H_v}{B_1} \qquad \text{instead of} \quad Q_3 \quad \text{and}$$

$$Q_3 = \frac{C_1 - H_v}{B_1} \,. \tag{26}$$

Their difference furnishes the rate of change of void fraction. Consequently,

$$V = \frac{(Q_3 - U_3)}{a_0 A} \,. \tag{27}$$

3. Post-extrapolation

The new element follows with the goal to transform the values of H_3, Q_3 or U_3 obtained in point 3 into values $H_8 = H(i, j+1)$, $Q_8 = Q(i, j+1)$ and $U_8 = U(i, j+1)$ in Figure 1. The transformation is based on the original nonlinear system of equations (5) and (9), defined by

$$K_h = H_8 - H_3 = (D_0 - D_1)\left[\frac{\partial H}{\partial t}\right]_3 + (\Delta x - x_4)\left[\frac{\partial H}{\partial x}\right]_3 , \tag{28}$$

$$K_q = Q_8 - Q_3 = (D_0 - D_1)\left[\frac{\partial Q}{\partial t}\right]_3 + (\Delta x - x_4)\left[\frac{\partial Q}{\partial x}\right]_3 . \tag{29}$$

The derivatives in brackets are expressed from the original equations (5) and (9) by the other partial derivatives, which in turn are computed as ratios of finite differences taken from the variables computed in the former steps in grid points $(i-1, j+1)$, $(i-1, j)$, (i, j) and $(i+1, j)$ in Figure 1. Consequently, equation (9) yields

$$\left[\frac{\partial H}{\partial t}\right]_3 = -\frac{a^2}{R_o g A}\frac{\Delta Q}{\Delta x} - \frac{Q}{A}\frac{\Delta H}{\Delta x} \,, \tag{30}$$

$$\left[\frac{\partial Q}{\partial t}\right]_3 = \frac{R_o g a}{a^2}\left(-\frac{\Delta H}{\Delta t} - \frac{Q}{A}\frac{\Delta H}{\Delta x}\right) \,. \tag{31}$$

In a similar manner equation (5) leads to the result

$$\left(\frac{\partial H}{\partial x}\right)_3 = \frac{1}{R_o g A}\left(-\frac{\Delta Q}{\Delta t} - \frac{\lambda}{2DA}Q\left|Q\right| - \frac{Q}{A}\frac{\Delta Q}{\Delta x} - gA\sin\alpha\right), \tag{32}$$

$$\left(\frac{\partial Q}{\partial t}\right)_3 = -R_o g A\frac{\Delta H}{\Delta x} - \frac{\lambda}{2DA}Q\left|Q\right| - \frac{Q}{A}\frac{\Delta Q}{\Delta x} - gA\sin\alpha\,. \tag{33}$$

The numerical derivatives are given by

$$\frac{\Delta H}{\Delta x} = \frac{\left(H\left(i+1,j\right) - H\left(i-1,j\right)\right)}{2\Delta x}, \tag{34}$$

$$\frac{\Delta Q}{\Delta t} = \frac{\left(Q(i-1,j+1) - Q(i-1,j)\right)}{D_0}\,. \tag{35}$$

After the derivatives in brackets have been defined K_h and K_q can be computed and the resulting variables

$$H_8 = H(i,j+1) = H_3 + K_h\,, \tag{36}$$

$$Q_8 = Q(i,j+1) = Q_3 + K_q \tag{37}$$

can be registered in the regular grid point $(i, j+1)$. As a last revision, only the condition $H_8 \leq H_v$ remains. If true, then the restriction (even if approximated by) $H(i,j+1) = H_v$ must be made, since otherwise negative absolute pressure could appear.

The treatment of boundary conditions in the first (MOC) step is identical with the usual one. Since at the boundaries only one of the characteristics can be applied, point 3 lies on the boundary higher or lower than the grid point (or coincides with it). The derivatives in brackets with respect to x are thus equal to zero. The numerical derivatives are somewhat different.

4. Numerical stability

Because of the nonlinearity of the governing equations and of the after-extrapolation method, numerical instability and oscillation can appear during the computation, especially in the presence of cavities at vapor pressure or column separation caused by gas or air release. Experience during the programming stage of simulation of the TPV system showed that to attain numerical stability the application of a somewhat simplified version of Kranenburg's "shock wave, nullifying cavitating flow region" model [2] and Vliegenthart's smoothing procedure [3] were necessary; they are compiled here. The jump through shock waves causes a decrease in the void fraction taken by the momentum equations in the form published by Kranenburg [2].

$$\frac{Q(i-1)}{A} + \frac{P(i-1) - P_v}{\rho_w a(i-1)} = B_1\,, \tag{38}$$

$$\frac{Q(i+1)}{A} + \frac{P(i-1) - P_v}{\rho_w a(i+1)} = B_2\,. \tag{39}$$

From the continuity

$$\Delta V = \frac{Q\left(i-1\right) - Q\left(i+1\right)}{A a_0}\,. \tag{40}$$

The pressure drop in the cavities caused by the gas released,

$$(P\,(i-1) - P_v)\,VA\,\Delta x = R_v T \Delta m \tag{41}$$

using the ideal gas law. The difference of momentum equations (38) and (39) yields the continuity in the form

$$a_0 \Delta V = B_1 - B_2 - \frac{P(i+1) - P_v}{\rho_w}\left(\frac{1}{a\,(i+1)} + \frac{1}{a\,(i-1)}\right). \tag{42}$$

The expressions B_1 and B_2 can be taken as

$$B_1 = \frac{Q\,(i-1)}{A} + g\frac{H(i-1) - H_v}{a(i)}\,, \tag{43}$$

$$B_2 = \frac{Q\,(i+1)}{A} + g\frac{H(i+1) - H_v}{a(i)} \tag{44}$$

according to the steps in MOC. Finally, mean values of H and a

$$\Delta V = \frac{Q(i-1) - Q(i+1)}{Aa_0} - 2g\frac{H(i) - H_v}{a_0 a\,(i)} \tag{45}$$

are used as correction to the void fraction at the end of every time step if the condition $V > 0$ has been met. The corrected $V(i+1) = V(i) + \Delta V$ value is restricted to $V(i+1) \geq 0$.

The smoothing trick consisted of evaluating

$$L\,(i) = \frac{H(i+1) + H(i-1)}{2} - H(i)\,. \tag{46}$$

If $L(i) > 0$ then

$$H(i) = H(i) + \frac{L(i)}{2}, \qquad \text{else} \qquad L(i) = 0\,. \tag{47}$$

5. Accuracy

The accuracy of the new method has been judged by comparison in two steps. First it has been compared numerically with a traditional, “pre-interpolating” method, programmed and run under itemized boundary conditions and an identical numerical grid [4]. The arrangement computed is shown in Figure 2. It is prepared to measure and record the pressure history during and after closing the exit valve in three points of the TPV system. The asymptotic behavior of the system after closing the exit valve is followed numerically by computing the time history of:

1. the temporary maxima and minima of the fluctuating pressure at the exit valve, and
2. the time mean value of the fluctuating volume flow rate entering or leaving the pipe at the tank ($x = 0$), using both pre-interpolating and post-extrapolating methods.

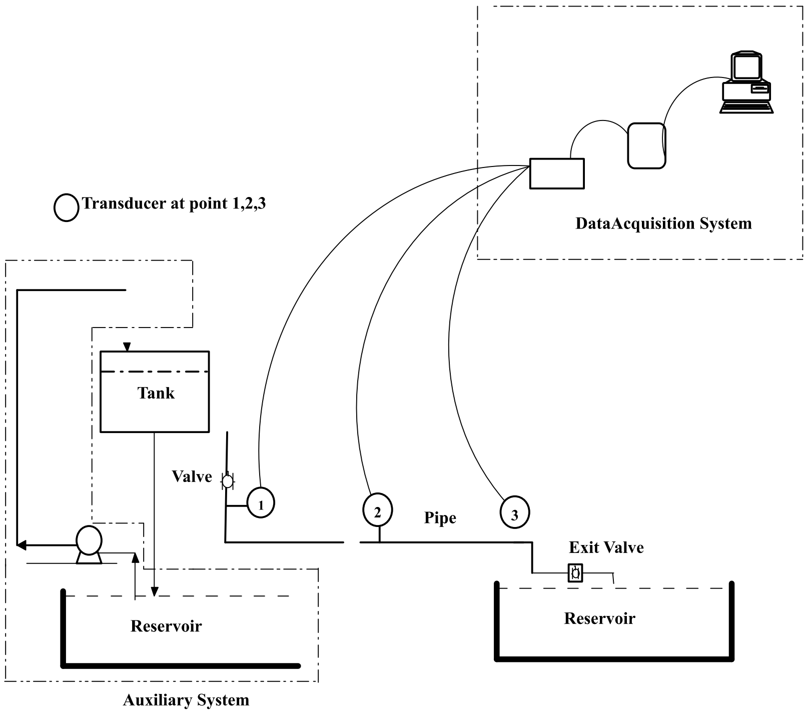

Figure 2. Experiment setup

The attenuation caused partly by the friction in the MOC method and partly by the additional artificial viscosity-like procedures in our method (which we call the New M method) appear in the asymptotic approximation of the limiting – static – value of the pressure as determined by the system data and by the zero flow rate. Some numerical runs with variable initial condition showed typical results after 104 time steps (nearly 30 times the duration of the closing time) of 0+3% or less of the limiting value as pressure fluctuation, and -10-5 as the ratio of the time mean flow rate to the initial flow rate; both values have been assumed as acceptable. Then as the second step the computed results have been compared with measured ones. Some results are shown in Figures 3 and 4 representing the middle and the endpoint, respectively. The agreement between the pre-interpolation (Simulation MOC) and post-extrapolation (Simulation New M) is remarkable. There are long time periods when the difference is less than 2% of the maximal pressure head measured. The deviations are greater near the second and third peak. They may be explained by the effect of the smoothing procedure, which should be improved, and possibly by the shock-wave capturing program, which could be refined: these two items are contained in the New M method and not in MOC. The measured pressure heads show somewhat greater deviation from both of the simulations above [5]. This can be explained partly by the usual errors in measuring

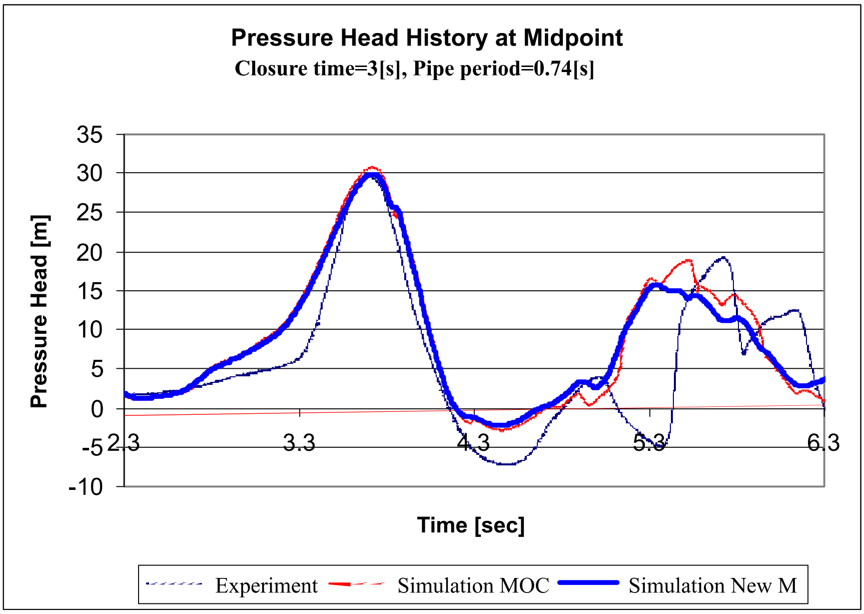

Figure 3. Pressure head history at midpoint of TPV system

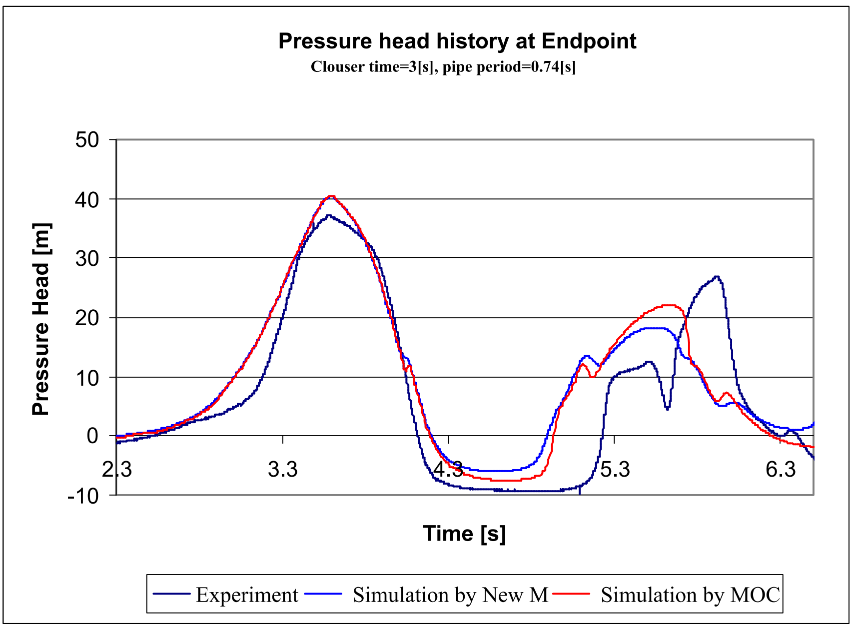

Figure 4. Pressure head history at endpoint of TPV system

equipment and methods (detailed in a special report [6]) and partly by the models of wave celerity and of gas release. It is very difficult to separate these factors without systematic modeling and measurements. Although a full description of the wave celerity and gas release models is beyond the scope of the present paper, we outline them below.

6. Celerity of pressure waves

The wave celerity a model used was based on results published by Wylie and Streeter [1] – see pp. 140–142 – after transformations in the form

$$\frac{a}{a_0} = \frac{H}{\sqrt{H^2 + mC_2}}\,, \tag{48}$$

where a_0 is the wave celerity in the fluid in the pipe without free gas or vapor,

$$C_2 = \frac{R_g T a_0^2}{\rho_w g^2}\,, \tag{49}$$

where m is the mass of free gas or vapor divided by the volume of the fluid.
The computed version is

$$m = m_1 = V\rho_v + m_3\,, \tag{50}$$

where m_3 $[kg/m^3]$ is the mass of the gas and/or air released and diffused in the cavities or contained in the incoming fluid in the unit of volume of fluid.

7. Cavity and gas release model

The incoming fluid is assumed to carry N_b homogeneously distributed cavitation nuclei in the unit of volume. Around the nuclei, there may be bubbles filled with gas (air) [7] and vapor, depending on the ambient pressure and temperature. The void fraction of the vapor is defined by equation (27) to be used in equation (50), on the condition that the pressure head is equal to the vapor pressure head H_v.

The mass of gas in unit volume of the fluid $m = m_3$ can be defined by

$$m = N_b \frac{D^3\pi}{6} \frac{\rho_w g H}{R_g T}\,, \tag{51}$$

or

$$\frac{m}{D^3 H} = N_b \frac{\pi}{6} \frac{\rho_w g}{R_g T} = S_n\,, \tag{52}$$

where D is the mean diameter of the bubbles and S_n is a known or guessed constant. The rate of the mass of gas released from the liquid and diffused into the bubbles has been calculated, following Kranenburg [2] by

$$\frac{\partial m}{\partial t} = N_b D^2 \pi \beta \frac{\partial c}{\partial r}\,, \tag{53}$$

where

$$\frac{\partial c}{\partial r} \cong \varepsilon \frac{c_0}{D\sqrt{\frac{\beta}{UD}}}\,. \tag{54}$$

With the initial concentration C_0 of the gas in liquid, according to Henry's law

$$C_0 = S_n \frac{\rho_w g H_{at}}{R_{air} T} . \tag{55}$$

Finally with $\varepsilon \approx 1$

$$\frac{\partial m}{\partial t} = F_c D^{\frac{3}{2}} , \tag{56}$$

$$F_c = N_b c_0 \pi \sqrt{\beta U} , \tag{57}$$

$$\frac{\partial m}{\partial t} \cong \frac{\Delta m_3}{D_0} , \tag{58}$$

$$\frac{D^3}{6} = V + \frac{m_3}{\rho_g} . \tag{59}$$

After each time step the diameter has been defined by equation (59), then Δm_3 from (58) and (56) then m_1 from equation (50) to continue with the new time step.

8. Conclusions

The introduction of the post-extrapolation, i.e. the use of the first partial derivatives of the governing equations, to define the variables after a MOC-type step at the regular grid points without pre-interpolation, proved to be successful in two-phase fluid flow with gas release and variable wave celerity in 1D elastic pipe transient flow computations. Instead of the Courant-type stability condition, simple shock-wave capturing and oscillation-smoothing techniques help to assure the numerical stability of the computations. The accuracy seems to correspond to traditional methods, although it can be influenced by the requirements of numerical stability [6, 7]. Measurements indicate the need for broader studies with respect to the appropriateness of the models of wave celerity and gas release used.

References

1. Wyle, E. B. and Streeter, V. L. *Fluid Transients in Systems.* McGraw-Hill, 1993.
2. Kranenburg, C. "Gas release during transient cavitation in pipes." *Journal of the Hydraulics Division,* **100**(10), (1974), pp. 1383–1398. doi: 10.1061/JYCEAJ.0004077.
3. Vliegenthart, A. C. "The Schumann filtering operator and numerical computation of shock waves." *Journal of Engineering Mathematics,* **4**(4), (1970), pp. 341–348. doi: 10.1007/BF01534981.
4. B. Stewardson, B. Brunone, and M. Ferrante. "Using Experiment design to determine transient pressure behaviour." *Proceeding of 8th International Conference Pressure Surges Safe Desigen.* BHRG Group, 2000, p. 611.
5. Kranenburg, C. "effect of Free Gas on Cavitation in Pipelines." *Proceeding of 1st International Conference Pressure Surges Safe Desigen.* BHRG Group, 1972, pp. 41–52.
6. Estuti, A. A. *Technical Experiment Report on the Investigation of Effect of Changing Valve Setting on Pressure Head Time History of TPV.* 2004.
7. Wyle, E. B. and Streeter, V. L. *Fluid Transients.* McGraw-Hill, 1978.

Nomenclature

a	pressure wave celerity	[m/s]
a_0	pressure wave celerity of one-phase flow	[m/s]
A	pipe cross section area	[m^2]
C	gas concentration in liquid	[kg/m^3]
C_0	initial concentration	[kg/m^3]
C_2	pressure wave celerity parameter	
D	diameter	[m]
D_0	time step	[s]
D_1	time ordinate in (3)	[s]
F_c	constant defined by equation (57)	
g	acceleration due to gravity	[m/s^2]
H	absolute pressure head	[m]
m	gas or vapor mass/volume	[kg/m^3]
N_b	number of nuclei in m^3	[1/m^3]
P	absolute pressure	[N/m^2]
Q	volume flow rate	[m^3/s]
R_o	density ratio	
R_g	gas law constant	[J/(kgK)]
R_v	gas law constant	[J/(kgK)]
S	Henry's constant	[m^3/m^3]
S_n	constant in equation (52)	
t	time	[s]
T	temperature	[K]
Δt	time step	[s]
u	velocity of fluid	[m/s]
U	volume flow rate (if cavity)	[m^3/s]
V	void fraction	[m^3/m^3]
x	length	[m]
Δx	reach length	[m]
x_4	abscissa of point 3	see Fig. 1
α	inclination angle of pipe	
β	diffusivity of gas	[m^2/s]
ρ	density	[kg/m^3]
λ	fraction factor	
ε	empirical constant	
Subscripts		
at	atmospheric	
w	liquid	
v	vapor	
g	gas	
3	at point 3	
8	at point 8	

Notes for Contributors
to the Journal of Computational and Applied Mechanics

Aims and scope. The aim of the journal is to publish research papers on theoretical and applied mechanics. Special emphasis is given to articles on computational mechanics, continuum mechanics (mechanics of solid bodies, fluid mechanics, heat and mass transfer) and dynamics. Review papers on a research field and materials effective for teaching can also be accepted and are published as review papers or classroom notes. Papers devoted to mathematical problems relevant to mechanics will also be considered.

Frequency of the journal. Two issues a year (approximately 80 pages per issue).

Submission of Manuscripts. Submission of a manuscript implies that the paper has not been published, nor is being considered for publication elsewhere. Papers should be written in standard grammatical English. The manuscript is to be submitted in electronic, preferably in pdf, format. The text is to be 130 mm wide and 190 mm long and the main text should be typeset in 10pt CMR fonts. Though the length of a paper is not prescribed, authors are encouraged to write concisely. However, short communications or discussions on papers published in the journal must not be longer than 2 pages. Each manuscript should be provided with an English Abstract of about 50–70 words, reporting concisely on the objective and results of the paper. The Abstract is followed by the Mathematical Subject Classification – in case the author (or authors) give the classification codes – then the keywords (no more than five). References should be grouped at the end of the paper in numerical order of appearance. Author's name(s) and initials, paper titles, journal name, volume, issue, year and page numbers should be given for all journals referenced.

The journal prefers the submission of manuscripts in LaTeX. Authors should select the $\mathcal{AMS}$-LaTeX article class and are not recommended to define their own LaTeX commands. Visit our home page for further details concerning how to edit your paper.

Manuscripts should be sent to either to the Editorial Office of JCAM:

jcam@uni-miskolc.hu

or directly to an editor: László Baranyi

laszlo.baranyi@uni-miskolc.hu (fluid mechanics and heat transfer)

or BalázsTóth

balazs.toth@uni-miskolc.hu (solid mechanics).

The eventual supply of an accepted for publication paper in its final camera-ready form will ensure more rapid publication. Format requirements are provided by the home page of the journal from which sample LaTeX files can be downloaded:

`http://www.mech.uni-miskolc.hu/jcam/`

These sample files can also be obtained directly (via e-mail) from Balázs Tóth.

One issue of the journal will be provided free of charge and mailed to the correspondent author. Since JCAM is an open access journal each paper can be downloaded freely from the homepage of the journal.

The Journal of Computational and Applied Mechanics is abstracted in Zentralblatt für Mathematik and in the Russian Referativnij Zhurnal.

Secretariat of the Vice-Rector for Research and International Relations, University of Miskolc
Responsible for publication: Prof. Dr. Zita Horváth, rector
Published by the Miskolc University Press under the leadership of Attila Szendi
Responsible for duplication: Works manager Erzsébet Pásztor
Number of copies printed: 75
Put to the Press on August 24, 2023
Number of permission: MERT.2023-199.ME.

ISSN 2732–0189 (Online)
ISSN 1586–2070 (Print)

A Short History of the Publications of the University of Miskolc

The University of Miskolc (Hungary) is an important center of research in Central Europe. Its parent university was founded by the Empress Maria Teresia in Selmecbánya (today Banska Štiavnica, Slovakia) in 1735. After the first World War the legal predecessor of the University of Miskolc moved to Sopron (Hungary) where, in 1929, it started the series of university publications with the title *Publications of the Mining and Metallurgical Division of the Hungarian Academy of Mining and Forestry Engineering* (Volumes I.-VI.). From 1934 to 1947 the Institution had the name Faculty of Mining, Metallurgical and Forestry Engineering of the József Nádor University of Technology and Economic Sciences at Sopron. Accordingly, the publications were given the title *Publications of the Mining and Metallurgical Engineering Division* (Volumes VII.-XVI.). For the last volume before 1950 – due to a further change in the name of the Institution – *Technical University, Faculties of Mining, Metallurgical and Forestry Engineering, Publications of the Mining and Metallurgical Divisions* was the title.

For some years after 1950 the Publications were temporarily suspended.

After the foundation of the Mechanical Engineering Faculty in Miskolc in 1949 and the movement of the Sopron Mining and Metallurgical Faculties to Miskolc, the Publications restarted with the general title *Publications of the Technical University of Heavy Industry* in 1955. Four new series - Series A (Mining), Series B (Metallurgy), Series C (Machinery) and Series D (Natural Sciences) - were founded in 1976. These came out both in foreign languages (English, German and Russian) and in Hungarian. In 1990, right after the foundation of some new faculties, the university was renamed to University of Miskolc. At the same time the structure of the Publications was reorganized so that it could follow the faculty structure. Accordingly three new series were established: Series E (Legal Sciences), Series F (Economic Sciences) and Series G (Humanities and Social Sciences). The latest series, i.e., the series H (European Integration Studies) was founded in 2001. The eight series are formed by some periodicals and such publications which come out with various frequencies.

Papers on computational and applied mechanics were published in the

Publications of the University of Miskolc, Series D, Natural Sciences.

This series was given the name Natural Sciences, Mathematics in 1995. The name change reflects the fact that most of the papers published in the journal are of mathematical nature though papers on mechanics also come out.

The series

Publications of the University of Miskolc, Series C, Fundamental Engineering Sciences

founded in 1995 also published papers on mechanical issues. The present journal, which is published with the support of the Faculty of Mechanical Engineering and Informatics as a member of the Series C (Machinery), is the legal successor of the above journal.

Journal of Computational and Applied Mechanics

Volume 18, Number 1 (2023)

Contents

Contributed Papers